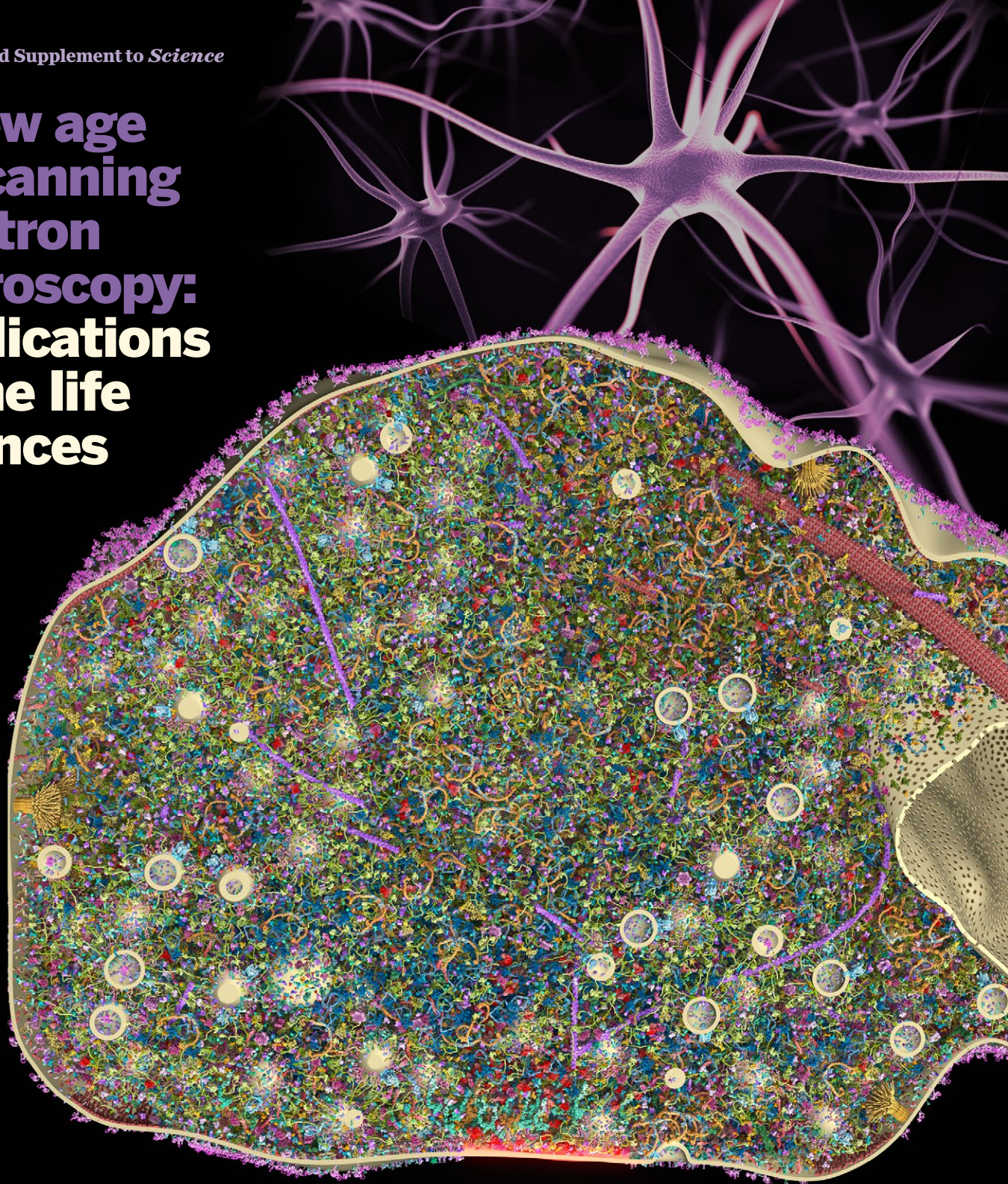


A Sponsored Supplement to *Science*

# A new age in scanning electron microscopy: Applications in the life sciences



Sponsored by



Produced by the  
Science/AAAS Custom  
Publishing Office

Science  
AAAS



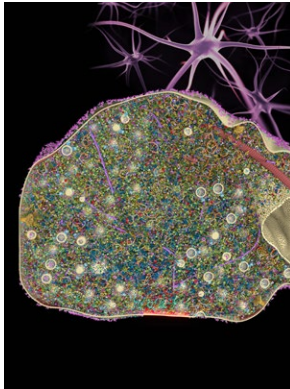
## AAAS MEMBERSHIP. MAKE THE CONNECTION.

**Join AAAS Sections.** They are the foundation of your AAAS membership

- **Be a subject-matter expert.**
- **Represent your discipline.**
- **Network with leaders in your field.**

[aaas.org/sections](https://www.aaas.org/sections)

AMERICAN ASSOCIATION FOR THE ADVANCEMENT OF SCIENCE



# A new age in scanning electron microscopy: Applications in the life sciences

About the cover: A realistic, molecular-scale view of a synapse, showing a few hundred thousand proteins. The synapse organization was measured by a combination of electron microscopy, quantitative biochemistry, and superresolution microscopy. From the cover of the May 30, 2014 issue of *Science*. Image: Burkhard Rammner/Rizzoli Laboratory, University of Göttingen Medical Center.

Original content (pages 29–42) has not been peer-reviewed or assessed by *Science*. These articles can be cited using the following format: [AUTHOR NAME(S)] in A new age in scanning electron microscopy: Applications in the life sciences (*Science/AAAS*, Washington, DC, 2017), p. [xx-xx].

This booklet was produced by the *Science/AAAS* Custom Publishing Office and sponsored by Carl Zeiss Microscopy GmbH, Germany

Editor: Sean Sanders, Ph.D.  
Proofreader/Copyeditor: Bob French  
Designer: Amy Hardcastle

ROGER GONCALVES, ASSOCIATE SALES DIRECTOR  
Custom Publishing  
Europe, Middle East, and India  
rgoncalves@science-int.co.uk  
+41-43-243-1358

© 2017 by The American Association for the Advancement of Science. All rights reserved. 29 September 2017

## Introductions

- 2 **The rise of SEM in the life sciences**  
Sean Sanders, Ph.D.  
*Science/AAAS*
- 3 **3D electron microscopy for the life sciences**  
Alexandra Elli, Ph.D.  
Eric Hummel, Ph.D.  
Jan Birkenbeil  
Carl Zeiss Microscopy GmbH, Germany

## Research articles

- 4 **Ultrastructural evidence for synaptic scaling across the wake/sleep cycle**  
Luisa de Vivo, Michele Bellesi, William Marshall *et al.*
- 8 **Increased spatiotemporal resolution reveals highly dynamic dense tubular matrices in the peripheral ER**  
Jonathon Nixon-Abell, Christopher J. Obara, Aubrey V. Weigel *et al.*
- 20 **Inflammation-induced disruption of SCS macrophages impairs B cell responses to secondary infection**  
Mauro Gaya, Angelo Castello, Beatriz Montaner *et al.*
- 25 **Development of the annelid axochord: Insights into notochord evolution**  
Antonella Lauri, Thibaut Brunet, Mette Handberg-Thorsager *et al.*

## Technical note

- 29 **Scanning Electron Microscopy in Life Sciences: Technical Solutions for Biological Applications**  
Alexandra Elli, Ph.D.; Robert Kirmse, Ph.D.;  
Bernhard Zimmermann, Ph.D.  
Carl Zeiss Microscopy GmbH, Germany

## Questions and answers

- 32 **A life of change in the brain: An interview with Jeff Lichtman**  
Mike May

## Application note

- 34 **Navigation of Bee Brains to Human Hip–Microscopy and the Modern Magellans**  
Melissa L. Knothe Tate, Ph.D.  
University of New South Wales

## The rise of SEM in the life sciences

The application of scanning electron microscopy in the biological sciences has enjoyed something of a renaissance.

The basic design and concept of the electron microscope (EM) have not changed much since its development in the 1930s. Nonetheless, incremental improvements in power and resolution have been achieved over the decades, even as prices have come down. More recently, however, and particularly in the last decade, the application of scanning electron microscopy in the biological sciences has enjoyed something of a renaissance, in part because of recent advances in EM technology. A quick PubMed search shows that the number of occurrences of the term “scanning electron microscope” (SEM) flatlined at around 150 per year through most of the 1980s and 1990s. Citations started to increase steadily beginning in the early 2000s, reaching over 1,100 in 2016—with no signs of slowing down.

These rough statistics support the notion that there has been an uptick in the introduction of SEM technology into life science laboratories to solve previously intractable problems. One area that has benefited considerably is neuroscience. SEM and transmission EM have been applied to reveal physiological changes during invertebrate development that can shed light on vertebrate evolution (see page 25). More recent advances, such as serial block-face SEM (SBEM)—the imaging of a tissue block following iterative removal of ultrathin (10 nm–50 nm) sections of the top layer of tissue using an ultramicrotome integrated into the EM—have allowed for the 3D reconstruction of neural tissue sample images, enabling scientists to study neurons and their connections in unprecedented detail (see page 4). Another recent advancement in EM hardware is focused ion beam SEM (FIB-SEM), which is also providing new opportunities to image cellular and subcellular structures in 3D. Rather than using a microtome to cut out thin sections of tissue, an ion beam is applied to carefully remove ultrathin layers of tissue, allowing for reconstruction of z-stacks capable of resolving intracellular organization in fine detail (see page 8).

Now that life science researchers have received a taste of what EM can do to drive their work forward, they are demanding increasingly advanced tools with more powerful capabilities. A number of companies—including ZEISS, the sponsor of this booklet—are stepping up to meet these demands and provide the technology needed to answer some of the most interesting biological questions, particularly in the field of neuroscience and neurological disease. No doubt there are many applications for this technology that have yet to be investigated and many new discoveries waiting to be made. All in all, this is a truly exciting time for the field of life sciences.

**Sean Sanders, Ph.D.**

Editor, Custom Publishing  
Science/AAAS

## 3D electron microscopy for the life sciences

The rapid evolution of innovative techniques in light microscopy has opened new horizons.

**"B**y the help of microscopes, there is nothing so small, as to escape our inquiry; hence there is a new visible world discovered to the understanding." The words of microscopy pioneer Robert Hooke fittingly reflect the great progress science has made in understanding the subcellular world in its most specific details.

Technical advances in the centuries after Hooke have brought to light many fascinating aspects of the microworld. The rapid evolution of innovative techniques in light microscopy has opened new horizons, but also (and to a much larger extent) new inquiries. New routes have emerged to enter the subcellular space with the use of electron microscopes (EM). Starting with transmission electron microscopy (TEM) and the work of German physicist Ernst Ruska, electron microscopes became routine tools to investigate the open questions in life science. The next big step was bringing 3D techniques into electron microscopy, such as tilt-based tomography that enabled the investigation of the 3D ultrastructure of organelles.

TEM, however, suffered from some limitations, including small sample volume and the fact that ultrastructural research was based primarily on TEM tomography or serial tomography. High-throughput and large-volume imaging methods using scanning electron microscopy (SEM) invigorated EM for the life sciences, making it possible to acquire large volumes in 3D using array tomography. Classical array tomography uses the sectioning capabilities of a microtome and—depending on the sample—typically reaches a z-resolution of 40 nm. A second groundbreaking development was the insertion of a microtome inside the SEM to section the block-surface after every image. Using this method, a z-resolution of 15 nm is achievable with samples of several hundred micrometers in height. A third approach has further improved z-resolution: Introduction of an ion gun into the SEM chamber allows researchers to get z-sections as thin as 3 nm.

One further sophisticated approach is to connect the world of light and EM. Correlative microscopy opens completely unexplored opportunities that could generate a wealth of scientific knowledge. For 170 years, ZEISS has pioneered many of the breakthroughs in the field and is now connecting its entire portfolio of advanced light, electron, ion, and X-ray microscopes, enabling researchers to gain fresh insights into the processes underlying life itself.

We hope you will find this collection of publications and peer-reviewed articles interesting and inspiring. At ZEISS, we believe that innovative electron microscopy and correlative techniques can make a big difference in your research, and we are excited to contribute to your success.

**Alexandra Elli, Ph.D.**

**Eric Hummel, Ph.D.**

**Jan Birkenbeil**

Carl Zeiss Microscopy GmbH, Germany  
microscopy@zeiss.com

## REPORT

## SLEEP RESEARCH

## Ultrastructural evidence for synaptic scaling across the wake/sleep cycle

Luisa de Vivo,<sup>1</sup> Michele Bellesi,<sup>1,2</sup> William Marshall,<sup>1</sup> Eric A. Bushong,<sup>3</sup> Mark H. Ellisman,<sup>3,4</sup> Giulio Tononi,<sup>1,\*</sup> Chiara Cirelli<sup>1,\*</sup>

It is assumed that synaptic strengthening and weakening balance throughout learning to avoid runaway potentiation and memory interference. However, energetic and informational considerations suggest that potentiation should occur primarily during wake, when animals learn, and depression should occur during sleep. We measured 6920 synapses in mouse motor and sensory cortices using three-dimensional electron microscopy. The axon-spine interface (ASI) decreased ~18% after sleep compared with wake. This decrease was proportional to ASI size, which is indicative of scaling. Scaling was selective, sparing synapses that were large and lacked recycling endosomes. Similar scaling occurred for spine head volume, suggesting a distinction between weaker, more plastic synapses (~80%) and stronger, more stable synapses. These results support the hypothesis that a core function of sleep is to renormalize overall synaptic strength increased by wake.

The cerebral cortex in humans contains 16 billion neurons and in mice 14 million neurons (1), and each neuron harbors thousands of synapses (2). Of the billions of cortical synapses of adult mice, ~80% are excitatory, and the majority of these are on dendritic spines (3). Spine size is tightly correlated with synaptic strength (3, 4); the area of the post-synaptic density (PSD), the area of the axon-spine interface (ASI), and the volume of the spine head (HV) are strongly correlated among themselves and with the number of vesicles in the presynapse (5–8), the number of synaptic AMPA receptors [AMPA receptors (9)], and the amplitude of AMPAR-mediated synaptic currents (10, 11).

Changes in synaptic strength are the primary mechanisms mediating learning and memory (12, 13). Synaptic potentiation and depression must be balanced to avoid either saturation or obliteration of neural signaling and memory traces (14), and it is usually assumed that overall synaptic strength is regulated throughout learning (15). The synaptic homeostasis hypothesis (SHY) (16) argues, however, that owing to energy and signaling requirements, learning should occur primarily through synaptic potentiation during wake, leading to a net increase in synaptic strength. This is because sparsely firing neurons can ensure that coincidences in their

inputs learned during wake are signaled throughout the brain only if the connections relating such coincidences are strengthened, not weakened. Overall synaptic renormalization by net weakening should occur during sleep, when animals are disconnected from the environment. The reason is that spontaneous neural activity can sample memories in a comprehensive and fair manner only if the brain is offline, without being at the mercy of current environmental inputs. Sleep can thus promote the acquisition, consolidation, and integration of new information as well as restore cellular function (16, 17).

Because stronger synapses are larger and weaker ones smaller (3, 4), SHY makes an intriguing prediction: Billions of cortical excitatory synapses should increase in size after wake and decrease after sleep, independent of circadian time. Furthermore, although synaptic renormalization should affect a majority of synapses, it should also be selective, to allow for both stability and plasticity (16–18).

We used serial block-face scanning electron microscopy (SBEM) (19) to obtain direct, high-resolution, three-dimensional (3D) volume measurements of synaptic size during the wake/sleep cycle and across thousands of synapses in two regions of mouse cortex. Brains were collected from three groups of mice (four mice per group) (Fig. 1A): S (sleep) mice spent at least 75% of the first ~7 hours of the light period asleep; EW (enforced wake) mice were kept awake during that time by exposure to novel objects; and SW (spontaneous wake) mice spent at least 70% of the first ~7 hours of the dark period spontaneously awake (Fig. 1B). S mice were compared with both SW and EW mice in order to tease apart sleep/wake effects from potential confounding factors due to time of day, light exposure, and stimulation or stress associated with enforced wake. In each mouse,

we sampled layer 2 of primary motor (M1) and primary somatosensory (S1) cortices. In these areas and layers, activity-dependent structural plasticity is well documented (3). Blocks of cortical tissue (~25 by 25 by 13–25 μm) were acquired and automatically aligned, and spiny dendritic segments were randomly selected within each block, balanced in size across groups (diameter =  $0.86 \pm 0.23$  μm, mean  $\pm$  SD) (table S1), and manually segmented by trained annotators blind to experimental condition (Fig. 1, C and D, and supplementary materials, materials and methods). Within each dendritic segment, all protrusions [also called “spines” (3)] were annotated, including spines forming synapses and a minority that lacked synapses (~13% of all protrusions) (table S1). Across all mice, 168 dendritic segments were segmented (101 in M1 and 67 in S1) (Fig. 1D and fig. S1), for a total of 8427 spines, of which 7149 formed a synapse. Synapses were defined by the presence of a presynaptic bouton with at least two synaptic vesicles within a 50-nm distance from the cellular membrane facing the spine, a visible synaptic cleft, and a PSD. In spines forming a synapse, ASI, HV—as well as vesicles, tubules, and multivesicular bodies (MVBs) that together form the nonsmooth endoplasmic reticulum (non-SER) compartment (20)—and the spine apparatus were segmented (Fig. 1, E and F) (supplementary materials, materials and methods). After excluding incomplete synapses, 6920 spines with a synapse contributed to the final analysis (tables S1 and S2).

ASI and PSD are strongly correlated with each other, and both become larger after synaptic potentiation (6–8). We focused on ASI—the surface of direct contact between axonal bouton and spine—as a structural measure of synaptic strength because in SBEM images, its exact borders are easier to identify than those of the PSD (21). First, we asked whether ASI sizes change as a function of wake and sleep using a linear mixed-effects (LME) model that included mouse and dendrite as random effects, condition (SW, EW, and S), and brain region (S1 and M1) as categorical fixed effects, and dendrite diameter as a linear fixed effect. Condition had a strong effect on ASI ( $\chi^2 = 10.159$ ,  $df = 2$ ,  $P = 0.0062$ ), which did not interact with either brain region or dendrite diameter. Post hoc analysis (adjusted for multiple comparisons) found that ASI sizes after sleep were reduced on average by 18.9% relative to spontaneous wake ( $P = 0.001$ ) and by 17.5% compared with enforced wake ( $P = 0.003$ ) (Fig. 2A and supplementary materials, materials and Methods, LME model for ASI). Spontaneous and enforced wake did not differ (SW versus EW,  $-1.7\%$ ;  $P = 0.957$ ). Thus, ASI sizes decrease with sleep on average by ~18% relative to both spontaneous and enforced wake, independent of time of day. There was instead no difference across groups in the distribution of dendrite ( $P = 0.248$ ) and mitochondrial ( $P = 0.445$ ) diameters, ruling out overall tissue shrinkage after sleep (fig. S2).

Consistent with the range of PSD and spine sizes in mouse somatosensory and auditory cortex (22, 23), the distribution of ASI sizes in our S1 and M1 samples was log-normal (Fig. 2B), a feature

<sup>1</sup>Department of Psychiatry, University of Wisconsin–Madison, 6001 Research Park Boulevard, Madison, WI 53719, USA.

<sup>2</sup>Department of Experimental and Clinical Medicine, Section of Neuroscience and Cell Biology, Università Politecnica delle Marche, Ancona, Italy. <sup>3</sup>National Center for Microscopy and Imaging Research, University of California, San Diego, 9500 Gilman Drive, La Jolla, CA 92093, USA. <sup>4</sup>Department of Neurosciences, School of Medicine, University of California, San Diego, 9500 Gilman Drive, La Jolla, CA 92093, USA.

\*Corresponding author. Email: ccirelli@wisc.edu (C.C.); gtononi@wisc.edu (G.T.)

thought to emerge from multiplicative dynamics (22). On the log scale, the S group showed an overall shift to the left relative to the SW and EW groups, suggesting that the decrease in ASI during sleep obeyed a scaling relationship (Fig. 2, B inset and C). Formal testing (supplementary materials, materials and methods) confirmed scaling, when sleep was compared with either spontaneous wake (average scaling  $-20.1\%$ ,  $P =$

$0.784$ ) or enforced wake (average scaling  $-19.1\%$ ,  $P = 0.648$ ). Monte Carlo simulations on bootstrapped data (supplementary materials, materials and methods) suggested that the change in ASI sizes between wake and sleep is not consistent with uniform scaling across all synapses but rather with selective scaling, in which a fraction of all synapses scales and the remaining portion does not. Of the models tested, the best fit was provided

when the likelihood of scaling decreased quadratically with increasing ASI size (Fig. 2D). This model fitted the actual data best, assuming that a majority of all synapses ( $>80\%$ ) would scale and that a minority ( $<20\%$ ) would be less likely to do so (Fig. 2D).

Do morphological features of synapses predict the likelihood of scaling? Given the results in Fig. 2D, we asked whether distinguishing between small to medium synapses (bottom 80%) versus large synapses would predict scaling versus no scaling. This distinction based on size was significant ( $P = 0.009$ ; small ASI: S versus SW  $-11.9\%$ ,  $P = 0.0002$ ; S versus EW  $-12.5\%$ ,  $P = 0.0001$ ; large ASI: S versus SW  $+0.7\%$ ,  $P = 0.999$ ; S versus EW  $+2.0\%$ ,  $P = 0.994$ ) (Fig. 3A) and robust for scaling fractions around 80% (supplementary materials, materials and methods). These results indicate that the ASIs of most synapses decrease during sleep in a manner proportional to their size, and that the largest 20% of spines are less likely to scale.

Plastic changes may preferentially occur in spines that contain recycling endosomes (24), whose presence reflects increased turnover of membranes, glutamate receptors, and other proteins that are essential to support activity-dependent structural changes (13, 24, 25). Indeed, only spines containing vesicles, tubules, and multivesicular bodies (MVBs), most of which are considered of endosomal origin (20), showed significant scaling ( $P = 0.00003$ ; vesicles/tubules, +: S versus SW  $-25.0\%$ ,  $P = 0.00001$ ; S versus EW  $-20.9\%$ ,  $P = 0.0008$ ; vesicles/tubules, -: S versus SW  $-2.9\%$ ,  $P = 0.985$ ; S versus EW  $-2.8\%$ ,  $P = 0.989$ ) (Fig. 3, B and C).

A spine's structural plasticity may be constrained by the overall spine density of its dendritic branch (26). Although synaptic density by itself was unaffected by wake and sleep ( $P = 0.761$ ), it interacted with the effect of sleep on ASI ( $P = 0.038$ ); the ASI decrease with sleep was largest in less spiny dendrites (S versus SW  $-36.4\%$ ; S versus EW  $-25.3\%$ ) and smallest in dendrites with higher synaptic density (S versus SW  $= 7.8\%$ ; S versus EW  $= -8.2\%$ ) (Fig. 3D).

In contrast, ASI decreased with sleep both in the spines with a spine apparatus (27)—a specialization of SER involved in calcium regulation and synthesis of transmembrane proteins—and in those without it (Fig. 3E) (28). Although spines facing an axonal bouton with one or more mitochondria were larger than spines lacking an axonal mitochondrion, scaling again occurred in both groups of spines (Fig. 3F). ASI size scales down between wake and sleep in small- and medium-sized synapses ( $\sim 80\%$  of the total population) but is less likely to do so in synapses that are large ( $\sim 20\%$ ) or in spines that contain no endosomes and is less marked in highly spiny dendrites.

Because HV is also strongly correlated with synaptic strength, we investigated changes in HV as a function of wake and sleep using a linear model that included the same random and fixed effects as for ASI (supplementary materials, materials and methods, LME model for HV). Results were consistent with those with ASI ( $\chi^2 = 6.942$ ,

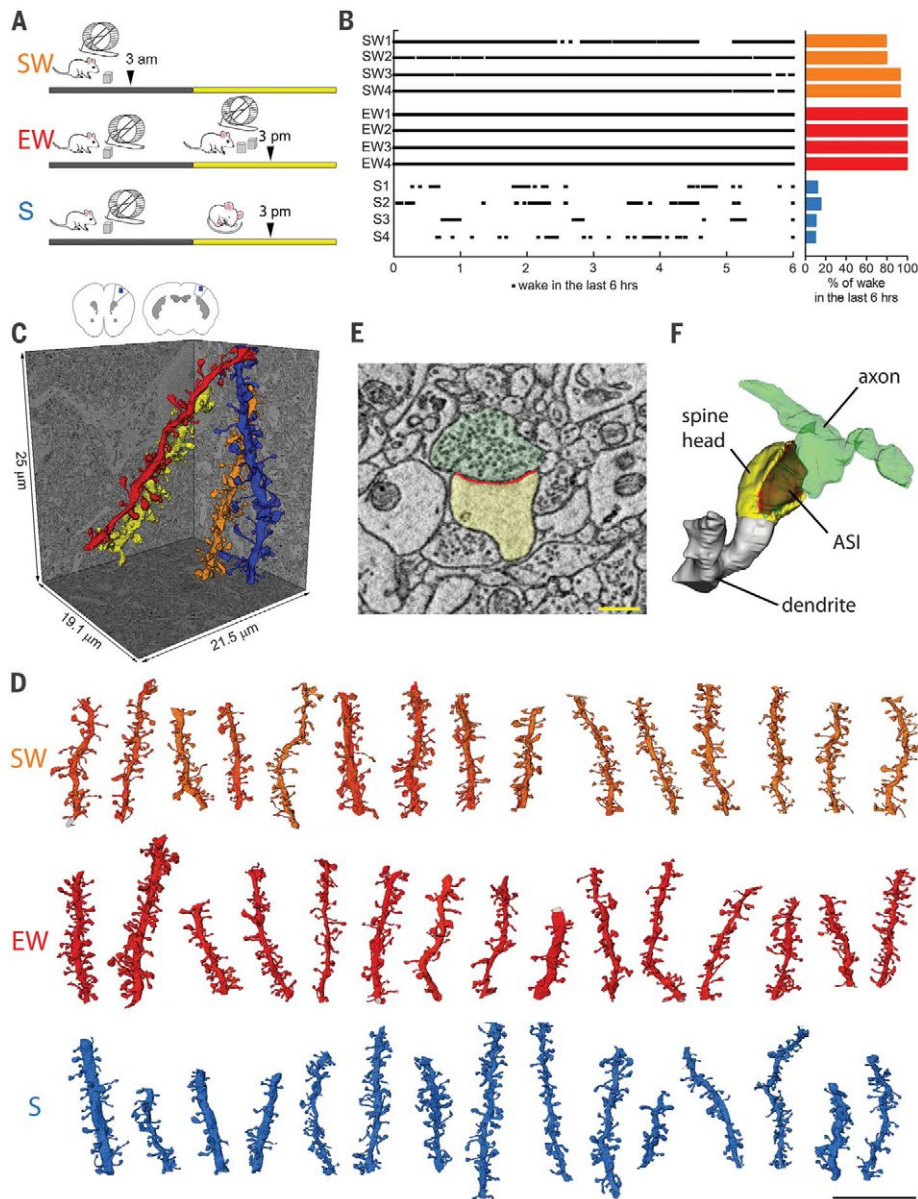


**Fig. 1. Experimental groups and SBEM segmentation of cortical synapses.** (A) The three experimental groups. SW, spontaneous wake at night; EW, wake during the day enforced by exposure to novel objects; S, sleep during the day. Arrowheads indicate time of brain collection. (B) Percent of wake in each mouse (four mice per group) during the last 6 hours before brain collection. (C) Schematic representation of mouse primary motor (M1, left) and somatosensory (S1, right) cortex, with the region of SBEM data collection indicated in layer 2 (blue box), and reconstruction of four spiny dendritic segments in S1. (D) Some of the dendritic segments from SW, EW, and S mice reconstructed in this study (all segments are shown in fig. S1). Scale bar, 15  $\mu\text{m}$ . (E and F) Raw image of a cortical spine containing a synapse and its 3D reconstruction. Spine head is in yellow, ASI is in red, and axonal bouton is in green. Scale bar, 350 nm.

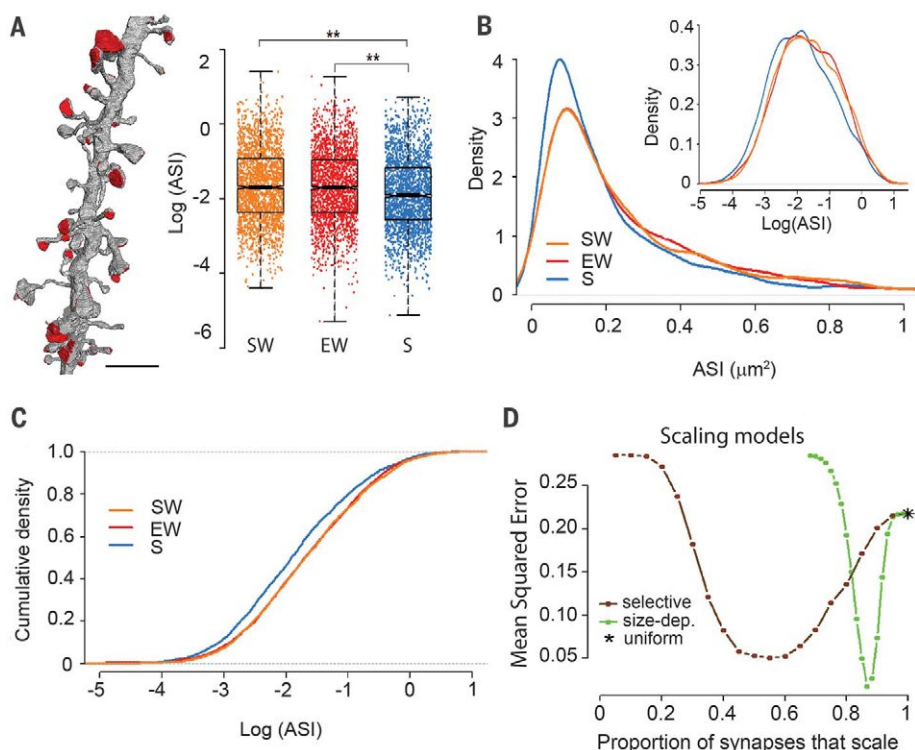


**Fig. 2. ASI size declines in sleep according to a scaling relationship.** (A) (Left) Visualization of ASIs in one dendrite. Scale bar, 2.5  $\mu\text{m}$ . (Right) Effect of condition. ASI size decreases in sleep (blue) relative to both spontaneous wake (orange) and enforced wake (red). ASI size is shown for all synapses, each represented by one dot.  $**P < 0.01$ . (B) Log-normal distribution of ASI sizes in the three experimental groups. (Inset) Same on a log scale. (C) The decrease in ASI size during sleep is due to scaling. (D) Monte Carlo simulations comparing different models of scaling. Size-dependent selective scaling (green) fits the actual data better than uniform scaling (asterisk) or selective scaling independent of size (brown) (supplementary materials, materials and methods).

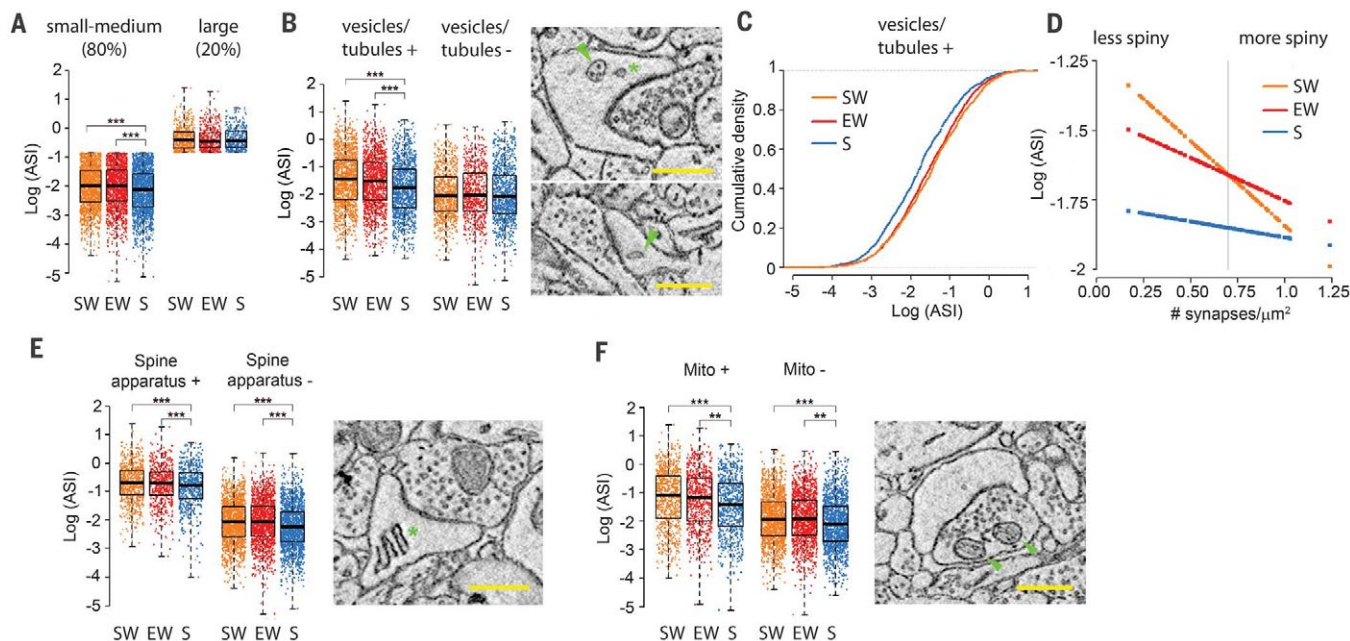


**Fig. 3. Scaling of ASI size is selective.** (A) The effect of sleep is present in small to medium synapses (80% of all synapses) but not in the largest ones (20% of all synapses). (B) The effect of sleep is present in spines with non-SER elements (vesicles, tubules, and multivesicular bodies, labeled “vesicles/tubules”). (Top right) A multivesicular body (arrowhead) and a coated vesicle (asterisk). (Bottom right) A non-SER tubule (arrowhead). (C) the ASI decrease during sleep in spines with vesicles/tubules is due to scaling. (D) The decline of ASI size in sleep is greatest in the dendrites with the lowest synaptic

density (range, 0.17 to 1.24/ $\mu\text{m}^2$ ). At the average value of synaptic density (vertical line; 0.70/ $\mu\text{m}^2$ ), the mean overall decrease is  $-17.3\%$  (S versus SW  $-17.4\%$ ,  $P = 0.002$ ; S versus EW  $-17.3\%$ ,  $P = 0.002$ ). (E and F) ASI size declines in sleep independently of the presence of spine apparatus (asterisk) or mitochondria in the axonal bouton (arrowheads). Scale bars, 500 nm. In all experimental groups, spines containing a spine apparatus or facing an axonal bouton with mitochondria are larger than spines lacking these elements.  $**P < 0.01$ ;  $***P < 0.001$ .

$df = 2, P = 0.031$ ), with one additional interaction (condition  $\times$  dendrite diameter): HV decreased most in the largest dendrites (S versus SW =  $-31.8\%$ ; S versus EW =  $-38.4\%$ ) and least in the smallest dendrites (S versus SW =  $-4.7\%$ ; S versus EW =  $1.3\%$ ) (fig. S3, A and B). Like ASIs, HVs followed a log-normal distribution (fig. S3C), and as a group, only the spines with vesicles, tubules, and MVBs showed a significant down-scaling in HV after sleep at an average value of dendrite diameter (vesicles/tubules +: S versus SW =  $-20.8\%$ ,  $P = 0.0006$ ; S versus EW =  $-14.3\%$ ,  $P = 0.045$ ; vesicles/tubules -: S versus SW =  $6.4\%$ ,  $P = 0.776$ ; S versus EW =  $1.3\%$ ,  $P = 0.999$ ) (fig. S3, D and E).

The ultrastructural demonstration of up- and down-scaling of synapse sizes with wake and sleep supports the hypothesis that wake leads to a net increase in synaptic strength, whereas a core function of sleep is to renormalize synaptic strength through a net decrease (16). Ultrastructural analysis provides the morphological ground truth, but it is necessarily limited to small brain samples. However, synaptic scaling across the wake/sleep cycle is likely to be a general phenomenon, irrespective of species, brain region, and specific plasticity mechanisms (16). We found similar changes in two different cortical regions. Moreover, protein levels of GluA1-containing AMPA receptors are higher after wake than after sleep (29) across the entire cerebral cortex. Also, the number of immunolabeled synaptic puncta increases with enriched wake and decreases with sleep in widespread regions of the fly brain (30). Last, electrophysiological markers of synaptic efficacy also increase broadly after wake and decrease after sleep (16).

The scaling of synaptic size is not uniform, which is consistent with the requirement that learning during wake must potentiate synapses selectively and with the hypothesis that selective renormalization during sleep favors memory consolidation, integration, and “smart” forgetting (16). We do not know how scaling is apportioned between wake and sleep. During wake, there may be a selective up-scaling of a smaller proportion of synapses because learning is limited to a particular environment (31), whereas down-scaling during sleep may be broader because the brain can sample

its memories comprehensively and fairly when it is offline (16). We also cannot rule out that a few synapses may up-scale in sleep (16, 17). Future studies labeling individual plastic events in the same synapses over wake and sleep may shed light on this issue. It will also be important to assess which molecular mechanisms are involved in the selective scaling of excitatory synapses in wake and sleep and to evaluate possible changes in inhibitory synapses (32).

We found that the synapses that most likely escape scaling are those that are large, those that lack endosomes, as well as those in crowded dendritic branches. These features may represent structural markers [besides molecular markers (33)] of synapses and associated memory circuits that are either committed or relatively stable despite the profound daily remodeling. We do not know, however, to what extent and over which time scale synapses may switch between this smaller pool of stronger, more stable synapses and the larger pool of weaker, more plastic synapses. An intriguing question is whether the subset of strong and stable synapses may originate preferentially from neurons at the top of the log-normal distribution of firing rates (34), whose level of activity seems to remain stable when the environment changes (35), or perhaps from neurons located in a specific layer (2/3 or 5).

#### REFERENCES AND NOTES

- S. Herculano-Houzel, *Front. Hum. Neurosci.* **3**, 31 (2009).
- Y. Tang, J. R. Nyengaard, D. M. De Groot, H. J. Gundersen, *Synapse* **41**, 258–273 (2001).
- A. Holtmaat, K. Svoboda, *Nat. Rev. Neurosci.* **10**, 647–658 (2009).
- J. Nishiyama, R. Yasuda, *Neuron* **87**, 63–75 (2015).
- K. M. Harris, J. K. Stevens, *J. Neurosci.* **9**, 2982–2997 (1989).
- N. L. Desmond, W. B. Levy, *Brain Res.* **453**, 308–314 (1988).
- P. A. Buchs, D. Muller, *Proc. Natl. Acad. Sci. U.S.A.* **93**, 8040–8045 (1996).
- C. E. Cheetham, S. J. Barnes, G. Albieri, G. W. Knott, G. T. Finnerty, *Cereb. Cortex* **24**, 521–531 (2014).
- Y. Katz et al., *Neuron* **63**, 171–177 (2009).
- M. Matsuzaki et al., *Nat. Neurosci.* **4**, 1086–1092 (2001).
- M. Bosch et al., *Neuron* **82**, 444–459 (2014).
- D. E. Feldman, *Annu. Rev. Neurosci.* **32**, 33–55 (2009).
- R. L. Huganir, R. A. Nicoll, *Neuron* **80**, 704–717 (2013).
- C. von der Malsburg, *Kybernetik* **14**, 85–100 (1973).
- M. Chistiakova, N. M. Bannon, J. Y. Chen, M. Bazhenov, M. Volgushev, *Front. Comput. Neurosci.* **9**, 89 (2015).
- G. Tononi, C. Cirelli, *Neuron* **81**, 12–34 (2014).
- B. Rasch, J. Born, *Physiol. Rev.* **93**, 681–766 (2013).
- W. C. Abraham, A. Robins, *Trends Neurosci.* **28**, 73–78 (2005).
- W. Denk, H. Horstmann, *PLOS Biol.* **2**, e329 (2004).
- J. R. Cooney, J. L. Hurlburt, D. K. Selig, K. M. Harris, J. C. Fiala, *J. Neurosci.* **22**, 2215–2224 (2002).
- P. S. Holcomb et al., *J. Neurosci.* **33**, 12954–12969 (2013).
- Y. Loewenstein, A. Kuras, S. Rumpel, *J. Neurosci.* **31**, 9481–9488 (2011).
- M. Cane, B. Maco, G. Knott, A. Holtmaat, *J. Neurosci.* **34**, 2075–2086 (2014).
- M. Park et al., *Neuron* **52**, 817–830 (2006).
- J. H. Tao-Cheng et al., *J. Neurosci.* **31**, 4834–4843 (2011).
- A. J. Holtmaat et al., *Neuron* **45**, 279–291 (2005).
- N. Holbro, A. Grunditz, T. G. Oertner, *Proc. Natl. Acad. Sci. U.S.A.* **106**, 15055–15060 (2009).
- L. E. Ostroff, C. K. Cain, J. Bedont, M. H. Monfils, J. E. Ledoux, *Proc. Natl. Acad. Sci. U.S.A.* **107**, 9418–9423 (2010).
- V. V. Vyazovskiy, C. Cirelli, M. Pfister-Genskow, U. Faraguna, G. Tononi, *Nat. Neurosci.* **11**, 200–208 (2008).
- D. Bushey, G. Tononi, C. Cirelli, *Science* **332**, 1576–1581 (2011).
- H. Makino, R. Malinow, *Neuron* **72**, 1001–1011 (2011).
- G. W. Knott, C. Quairiaux, C. Genoud, E. Welker, *Neuron* **34**, 265–273 (2002).
- G. H. Diering, A. S. Gustina, R. L. Huganir, *Neuron* **84**, 790–805 (2014).
- G. Buzsáki, K. Mizuseki, *Nat. Rev. Neurosci.* **15**, 264–278 (2014).
- A. D. Groszmark, G. Buzsáki, *Science* **351**, 1440–1443 (2016).

#### ACKNOWLEDGMENTS

We thank E. Christensen, P. Horvath, S. Koebe, S. Loschky, R. Massopust, M. Nagai, and A. Schroeder for their contribution to the manual segmentation of SBEM images. This work was supported by NIH grants DP 10D579 (G.T.), 1R01MH091326 (G.T.), 1R01MH099231 (G.T. and C.C.), 1P01NS083514 (G.T. and C.C.), and P41GM103412 for support of the National Center for Microscopy and Imaging research (M.H.E.). The other authors declare no competing financial interests. G.T. is involved in a research study in humans supported by Philips Respironics; this study is not related to the work presented in the current manuscript. The other authors declare no competing financial interests. Data (ASI and HV measures) are available at <http://centerforsleepandconsciousness.med.wisc.edu>.

#### SUPPLEMENTARY MATERIALS

[www.sciencemag.org/content/355/6324/507/suppl/DC1](http://www.sciencemag.org/content/355/6324/507/suppl/DC1)  
Materials and Methods  
Figs. S1 to S3  
Tables S1 and S2  
References (36–53)

19 July 2016; accepted 20 October 2016  
10.1126/science.aah5982

## RESEARCH ARTICLE

## CELLULAR STRUCTURE

# Increased spatiotemporal resolution reveals highly dynamic dense tubular matrices in the peripheral ER

Jonathon Nixon-Abell,<sup>1,2\*</sup> Christopher J. Obara,<sup>3,4\*</sup> Aubrey V. Weigel,<sup>3,4\*</sup> Dong Li,<sup>4,5</sup> Wesley R. Legant,<sup>4</sup> C. Shan Xu,<sup>4</sup> H. Amalia Pasolli,<sup>4</sup> Kirsten Harvey,<sup>2</sup> Harald F. Hess,<sup>4</sup> Eric Betzig,<sup>4</sup> Craig Blackstone,<sup>1†‡</sup> Jennifer Lippincott-Schwartz<sup>3,4†‡</sup>

The endoplasmic reticulum (ER) is an expansive, membrane-enclosed organelle that plays crucial roles in numerous cellular functions. We used emerging superresolution imaging technologies to clarify the morphology and dynamics of the peripheral ER, which contacts and modulates most other intracellular organelles. Peripheral components of the ER have classically been described as comprising both tubules and flat sheets. We show that this system consists almost exclusively of tubules at varying densities, including structures that we term ER matrices. Conventional optical imaging technologies had led to misidentification of these structures as sheets because of the dense clustering of tubular junctions and a previously uncharacterized rapid form of ER motion. The existence of ER matrices explains previous confounding evidence that had indicated the occurrence of ER “sheet” proliferation after overexpression of tubular junction-forming proteins.

The ER is a continuous, membranous network extending from the nuclear envelope to the outer periphery of cells; it plays vital roles in processes such as protein synthesis and folding, mitochondrial division, calcium storage and signaling, and lipid synthesis and transfer. In the cell periphery, the ER is thought to exist as an elaborate membrane system that makes contact with nearly every other cellular organelle. Prevailing models of its structure propose a complex arrangement of interconnected tubules and sheets, each of which is maintained by distinct mechanisms (1, 2). Numerous proteins are involved in maintaining this complex structural organization. Membrane curvature-stabilizing proteins, including members of the reticulon (RTN) and REEP families, contain hydrophobic hairpin domains that are thought to be responsible for promoting curvature in ER tubules via scaffolding and hydrophobic wedging. Members of the atlastin (ATL) family of dynamin-related guanosine triphosphatases (GTPases) are thought to mediate the formation of tubular three-way junctions, giving rise to the characteristic polygonal

tubular network (3). Meanwhile, an alternative complement of proteins is proposed to regulate the structure of ER sheets, with p180, kinectin, and CLIMP63 all thought to play a role in shaping, helicoidal stacking, and luminal spacing (3). Mutations in many of these ER-shaping proteins are connected to a variety of human disease conditions, most notably the hereditary spastic paraplegias (4). Thus, characterizing ER morphology is critical to understanding the basic biology of cells in both health and disease.

Determining the structure of the ER is challenging because of limitations in our ability to visualize the intricate nature of its morphology. The peripheral ER is particularly susceptible to this constraint, given its well-documented dynamic rearrangements and fine ultrastructure (5, 6). These characteristics impede attempts to derive functional information based on changes to ER structure. The recent development of various superresolution (SR) imaging approaches, however, offers an opportunity to examine ER structure and dynamism with substantially improved spatiotemporal resolution. Here, we used five different SR modalities, each having complementary strengths and weaknesses in the spatial and temporal domains, to examine ER structure and dynamics. A high-speed variation of structured illumination microscopy (SIM) allowed ER dynamics to be visualized at unprecedented speeds and resolution. Three-dimensional SIM (3D-SIM) and Airyscan imaging allowed comparison of the fine distributions of different ER-shaping proteins. Finally, lattice light sheet-point accumulation for imaging in nanoscale topography (LLS-PAINT) and focused ion beam scanning electron microscopy (FIB-SEM) permitted 3D char-

acterization of different ER structures. Thoroughly probing the ER in this manner provides unprecedented information about the morphology and dynamics of this organelle, including the characterization of a previously underappreciated structure within the peripheral ER.

## ER tubules and junctions undergo rapid motion in living cells

ER tubules are known to undergo rapid structural rearrangements, occurring over seconds or minutes, yet examination of these processes has typically been confined to the extension and retraction of tubules and the formation of tubular three-way junctions (5, 6). To obtain a more comprehensive picture of tubular motion, we used high-speed SIM with grazing incidence illumination (GI-SIM; see materials and methods) (7). This live SR imaging modality (resolution ~100 nm) uses light beams counterpropagating just above the sample substrate to image cellular features near the basal plasma membrane at frequencies up to 40 Hz. This translates to a factor of 4 to 10 increase in acquisition speed, relative to what can be practically achieved with spinning-disk confocal microscopy for imaging the ER, and a factor of ~2 improvement in resolution.

With GI-SIM, we imaged COS-7 cells expressing an ER membrane marker (mEmerald-Sec61 $\beta$ , henceforth Sec61 $\beta$ ) to track ER tubules. Increased spatiotemporal resolution revealed a novel form of ER motion consisting of remarkably rapid tubular fluctuations (Fig. 1 and movie S1). Using a modified skeletonization algorithm (8) to track the movement of ER tubules (Fig. 1B), we identified oscillations with a mean peak-to-peak amplitude of  $70 \pm 50$  nm, occurring an average of  $4 \pm 1$  times per second (means  $\pm$  SD;  $n = 1753$  tubules from 8 cells) (Fig. 1, C and D). Traditional imaging modalities have the ability to localize precisely this tubular motion only if the tubules and junctions are sufficiently sparse. Also, a large proportion of this motion often occurs on too short a time scale to be effectively tracked using spinning-disk confocal microscopy at imaging speeds commonly reported in the literature (6, 9). This suggests that in dense regions, tubular ER motion and morphology are likely to be obscured when using traditional imaging modalities. These rapid fluctuations we observed in COS-7 cells were also found in an unrelated cell type (U-2 OS) as well as in COS-7 cells expressing a luminal ER marker (mEmerald-ER3, henceforth ER3; see materials and methods) instead of Sec61 $\beta$  (Fig. 1, C to E, and tables S1 and S2).

In addition to the tubules themselves, three-way junctions also exhibited appreciable motion over very short time scales (Fig. 1, F and G, and movie S1). Three-way junctions were identified from the skeletonization of fluorescent ER images. Skeletonized pixels with exactly two neighbors were considered to be part of a branch (Fig. 1F, white), and pixels with more than two neighbors were considered junctions (Fig. 1F, overlaid with cyan dots). Three-way junctions were then treated as single particles and tracked (Fig. 1F, green). The time-averaged mean square displacement

<sup>1</sup>Cell Biology Section, Neurogenetics Branch, National Institute of Neurological Disorders and Stroke (NINDS), Bethesda, MD, USA. <sup>2</sup>Department of Pharmacology, UCL School of Pharmacy, University College London, London, UK. <sup>3</sup>Cell Biology and Metabolism Program, Eunice Kennedy Shriver National Institute of Child Health and Human Development (NICHD), Bethesda, MD, USA. <sup>4</sup>Janelia Research Campus, Howard Hughes Medical Institute (HHMI), Ashburn, VA, USA. <sup>5</sup>National Laboratory of Biomacromolecules, Institute of Biophysics, Chinese Academy of Sciences, Beijing, China.

\*These authors contributed equally to this work. †These authors contributed equally to this work. ‡Corresponding author. Email: blackste@ninds.nih.gov (C.B.); lippincottschwartz@janelia.hhmi.org (J.L.-S.)

(MSD) of three-way junctions can be described as  $\text{MSD} \sim t^\alpha$ , where  $\alpha$  describes a particle's motion as Brownian ( $\alpha = 1$ ), subdiffusive ( $\alpha < 1$ ), or superdiffusive ( $\alpha > 1$ ) (10). Junction dynamics exhibited a broad distribution of  $\alpha$  (Fig. 1G and table S1). Again, these results were consistent among cells expressing membrane or luminal markers as well as in other cell types such as U-2 OS (Fig. 1G and tables S1 and S2).

Such rapid dynamics can often represent thermally derived motion in systems, but in this context thermal energy alone does not appear to be responsible for driving ER dynamics. Indeed, the motion of both tubules and three-way junctions characterized above was substantially altered by a variety of biological perturbations. Diverse treatments affecting access to cellular energy sources [deoxyglucose (DOG) + sodium azide ( $\text{NaN}_3$ ); aluminum fluoride (AlF)], cytoskeletal dynamics (blebbistatin), or protein translation (puromycin; cycloheximide) each reduced the amplitude and increased the frequency of oscillations to levels consistent with thermally derived Brownian motion (11) (Fig. 1, C to E). Additionally, the motion of three-way junctions was dampened (Fig. 1G). Although the broad susceptibility of rapid ER dynamics to pharmacological perturbation does not elucidate the direct source of the motion, it suggests a broader role for cellular dynamics in driving ER motion, as it is affected by a range of disparate processes. Of note, treatment with the

microtubule-depolymerizing agent nocodazole increased the frequency of motion without any noticeable effect on amplitude (Fig. 1E and table S2), so it appears that at least in some situations, the amplitude and frequency of tubule oscillations can be uncoupled.

### Peripheral “sheets” appear highly dynamic and are riddled with spaces

GI-SIM also permitted rapid imaging of the morphology and dynamics of structures that appeared to be flat peripheral sheets by diffraction-limited epifluorescence, leading to several highly unexpected observations. At the improved spatiotemporal resolution afforded by GI-SIM, most peripheral “sheets” do not appear continuous, but rather are riddled throughout with spaces devoid of Sec61 $\beta$  fluorescence (Fig. 2, A and B). These spaces are highly dynamic and densely distributed across the structure (Fig. 2B, kymographs). To analyze these dynamics, we used a fluorescence inversion and image preparation protocol (see materials and methods) (12), transforming the dark areas into particle-like entities that are trackable using single-particle tracking (SPT) algorithms (13) (Fig. 2C and movie S2). The spaces were tracked and their lifetimes were extracted from the trajectories. For distances between tubules (spaces) larger than our ~100-nm limit of resolution, we quantified the average lifespan ( $250 \pm 250$  ms,  $n = 4292$  tracks from 4 cells)

and detectable separation between tubules ( $260 \pm 350$  nm,  $n = 1273$  spaces from 4 cells) (Fig. 2D and tables S3 and S4). There was no significant difference in the lifespan or apparent size of voids in intensity in either U-2 OS or COS-7 cells expressing Sec61 $\beta$  (table S4). Measurable gaps between tubules did, however, appear significantly smaller in cells expressing Sec61 $\beta$  than in cells expressing ER3, presumably because of the relocation of the fluorescence tag from the lumen to the cytoplasmic surface of the ER membrane (Fig. 2D and tables S3 and S4; see also supplementary text). This apparent dilatation of the structure would be predicted to lead to an appearance of constriction in remaining nonfluorescent spaces. Certainly, the size and lifetime of the spaces observed with GI-SIM within these peripheral structures would render a substantial proportion of them undetectable by more traditional imaging modalities.

To accompany the SPT of these transient spaces, we used an analysis that does not require a best-fit process, termed the temporal intensity derivative (detailed in materials and methods; see also fig. S1). This technique maps locations in the structure where substantial changes in fluorescence intensity occur over defined time windows. We found that even across a very short time frame (250 ms), we were able to detect substantial motion in ER tubules, consistent with the tubular oscillations described in Fig. 1. Intriguingly, nearly the entire area of structures that appeared as peripheral

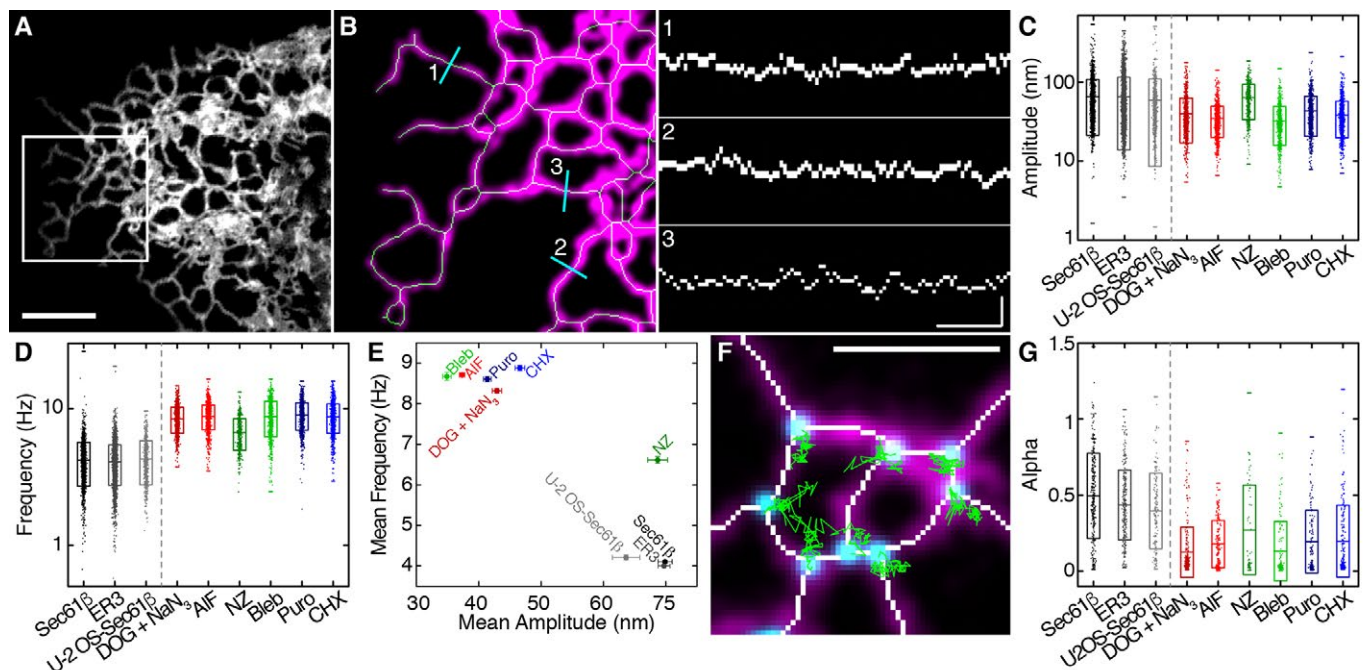


**Fig. 1. The peripheral ER moves at high speeds.** (A) Tubular ER in the periphery of a COS-7 cell expressing Sec61 $\beta$  imaged live at 40 Hz using GI-SIM microscopy. Scale bar, 2  $\mu\text{m}$ . (B) ER tubules within the boxed region in (A), identified using a skeletonization algorithm. Left: The midline of each tubule (green) is mapped onto the fluorescence (magenta). Right: Positions of the midlines are plotted as kymographs against time for each of the three locations shown in cyan at left; scale bars, 200 nm and 0.5 s. (C and D) Amplitudes (C) and frequencies (D) of tubular ER oscillations in COS-7 cells expressing Sec61 $\beta$  treated with deoxyglucose plus sodium azide (DOG +  $\text{NaN}_3$ ), AlF, nocodazole (NZ), blebbistatin

(Bleb), puromycin (Puro), and cycloheximide (CHX). Untreated controls using a luminal ER marker (ER3) and results for a different cell line (U-2 OS–Sec61 $\beta$ ) are also shown. (E) Plot of frequency versus amplitude for tubular oscillations in treated and untreated cells. Error bars represent SEM. (F) Locations of three-way junctions derived from skeletonized data (white). Original fluorescence is shown in magenta; example tracks of junctions (cyan) over 2.5 s are indicated in green. Scale bar, 2  $\mu\text{m}$ . (G) MSD scaling exponent ( $\alpha$  values) for treated and control cells. Box plots indicate the mean and SD in (C), (D), and (G); range is indicated by outer tick marks. See tables S1 and S2 for a detailed list of means and test statistics.

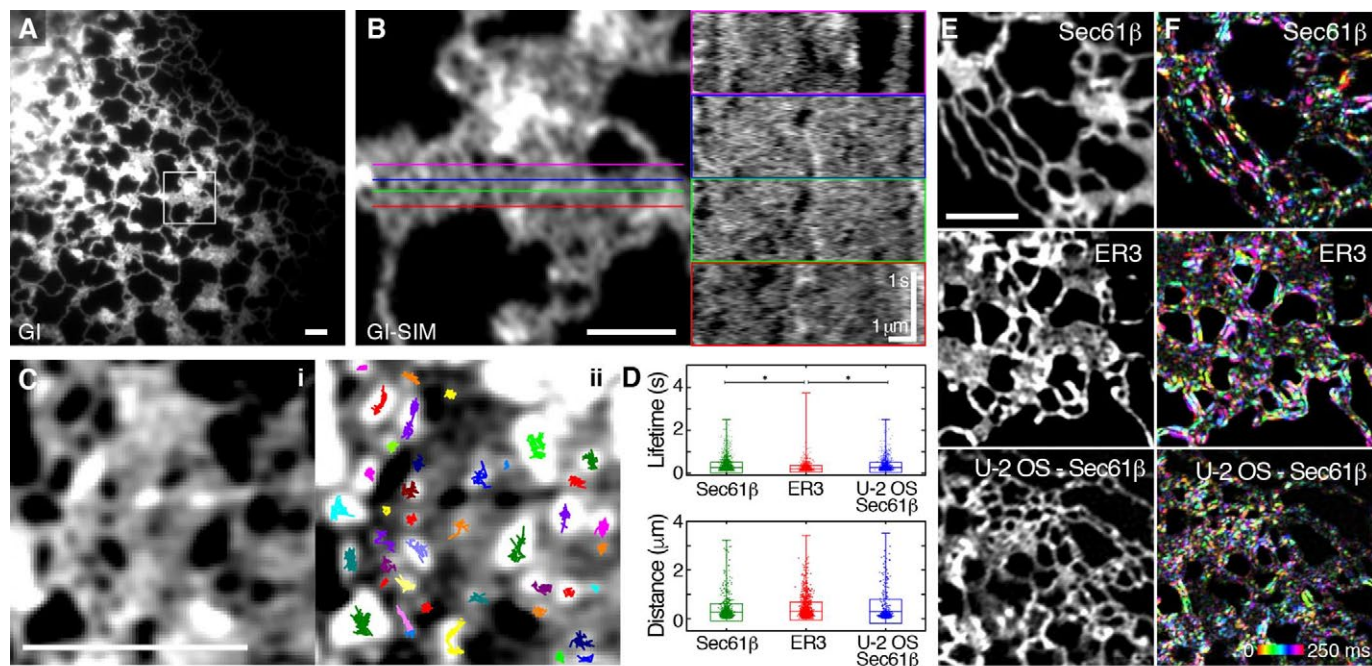


**Fig. 2. Peripheral ER “sheets” are highly dynamic and riddled with spaces.** (A) COS-7 cell expressing Sec61β imaged live by GI at 40 Hz exhibits many peripheral sheet-like structures. (B) GI-SIM of the boxed region in (A) shows many discrete spaces throughout the structure. Colored lines at left correspond to the locations of the kymographs shown at right. Voids in intensity within the structure can be seen appearing and disappearing over time. (C) Single-particle tracking (SPT) of dark spaces within the structure. The fluorescence image (i) was inverted and spaces were tracked using SPT algorithms. Tracks overlaid onto the inverted image are shown in (ii), with trajectories shown in different colors. (D) Each track length corresponds to

the lifetime of the space; distance across the space (i.e., distance between tubules) is also quantified. The box plot indicates the SD and mean; range is indicated by outer tick marks. The asterisks denote significant difference between means, detailed in table S4. (E and F) Temporal intensity derivative analysis (see materials and methods) of representative peripheral sheet-like structures in a COS-7 cell expressing Sec61β, with a luminal ER marker (ER3) and another cell line (U-2 OS-Sec61β) as controls. (E) Original fluorescence images. (F) Each consecutive frame over a 250-ms time period is color-coded, with intensity corresponding to the magnitude of fluorescence change. Scale bars, 2 μm. See tables S3 and S4 for a detailed list of means and test statistics.

“sheets” by conventional imaging also underwent fluctuations in fluorescence intensity similar to that of isolated tubules, suggesting major structural rearrangements within these structures over this time frame (Fig. 2, E and F). This phenomenon was consistently observed in COS-7 cells expressing either Sec61β or ER3, as well as in U-2 OS cells expressing Sec61β. Collectively, the rapid rearrangement of spaces and the magnitude of fluorescence changes across very short time scales within peripheral sheet-like structures imply that these regions are not likely to be continuous in nature.

### Rapid assembly and disassembly of sheet-like structures into isolated tubules

In further support of this idea, longer time-lapse imaging with GI-SIM revealed rapid assembly and disassembly of sheet-like structures from clearly isolated tubules (movie S3). Given that this process occurs over relatively short time frames, it seems unlikely that energetically costly fusion or fission of the ER membrane would be required. Instead, our data suggest a possible mechanism whereby tubules could coalesce until the spaces between them become too small to observe, leading to the discontinuities described above. Consequently, dense networks could expand outward to isolated tubules by the reverse mechanism, without requiring membrane fusion or fission. This could be achieved by well-characterized motion

through molecular motors or by the sliding of three-way junctions along tubules (3).

### SR imaging reveals the existence of dense tubular matrices in the peripheral ER

To gain a more comprehensive understanding of structures classically defined as peripheral sheets, we performed parallel experiments using SR imaging to reconstruct the protein and lipid distribution across the entire ER. COS-7 cells expressing Sec61β as an ER marker (thought to be expressed uniformly across the ER) were fixed and imaged by wide-field 3D-SIM, providing a representative map of ER transmembrane protein distribution throughout the cell (Fig. 3A). Remarkably, many structures that appeared to be intact sheets by diffraction-limited, wide-field imaging instead comprised a dense, cross-linked network of tubules enriched in three-way junctions (Fig. 3A). Notably, these structures were flat relative to their height but showed substantial variation in local topology (Fig. 3A, color coding).

To verify that the ER membrane itself shared this structure, we turned to an even higher-resolution imaging technique that directly probes the locations of the membranes themselves. LLS-PAINT microscopy uses single-molecule localization of individual fluorescent lipid molecules as they stabilize on cellular membranes (14). COS-7 cells expressing Sec61β were fixed and the

structure of the internal membranes was ascertained at the single-molecule level by LLS-PAINT microscopy (movie S4). In addition, for each cell, a single diffraction-limited 3D LLS image (15) was taken of the Sec61β signal to allow ER membranes to be distinguished from those of other organelles (Fig. 3B and movie S4). The resulting data set confirms that many ER structures that appear as continuous sheets with diffraction-limited imaging are shown to be dense tubular matrices when viewed using LLS-PAINT (Fig. 3B, insets). Many ER matrices had substantial topological variation across their structures, again supporting the notion that they are not strictly 2D (Fig. 3B, iii, and fig. S2). Thus, with improved spatial resolution in three dimensions, both protein and lipid components of the peripheral ER appear to comprise dense matrices of highly convoluted tubules.

### Limitations in spatiotemporal resolution obscure dense tubular matrices

Given our observations that ER tubules undergo very rapid motion (Fig. 1), that many spaces in structures previously described as sheets are near or beneath the diffraction limit (Fig. 2), and that SR imaging of both ER membrane protein and lipid reveals most of these structures to be dense tubular networks (Fig. 3), we hypothesized that limitations in spatiotemporal resolution might obscure dense tubular matrices and lead to their frequent

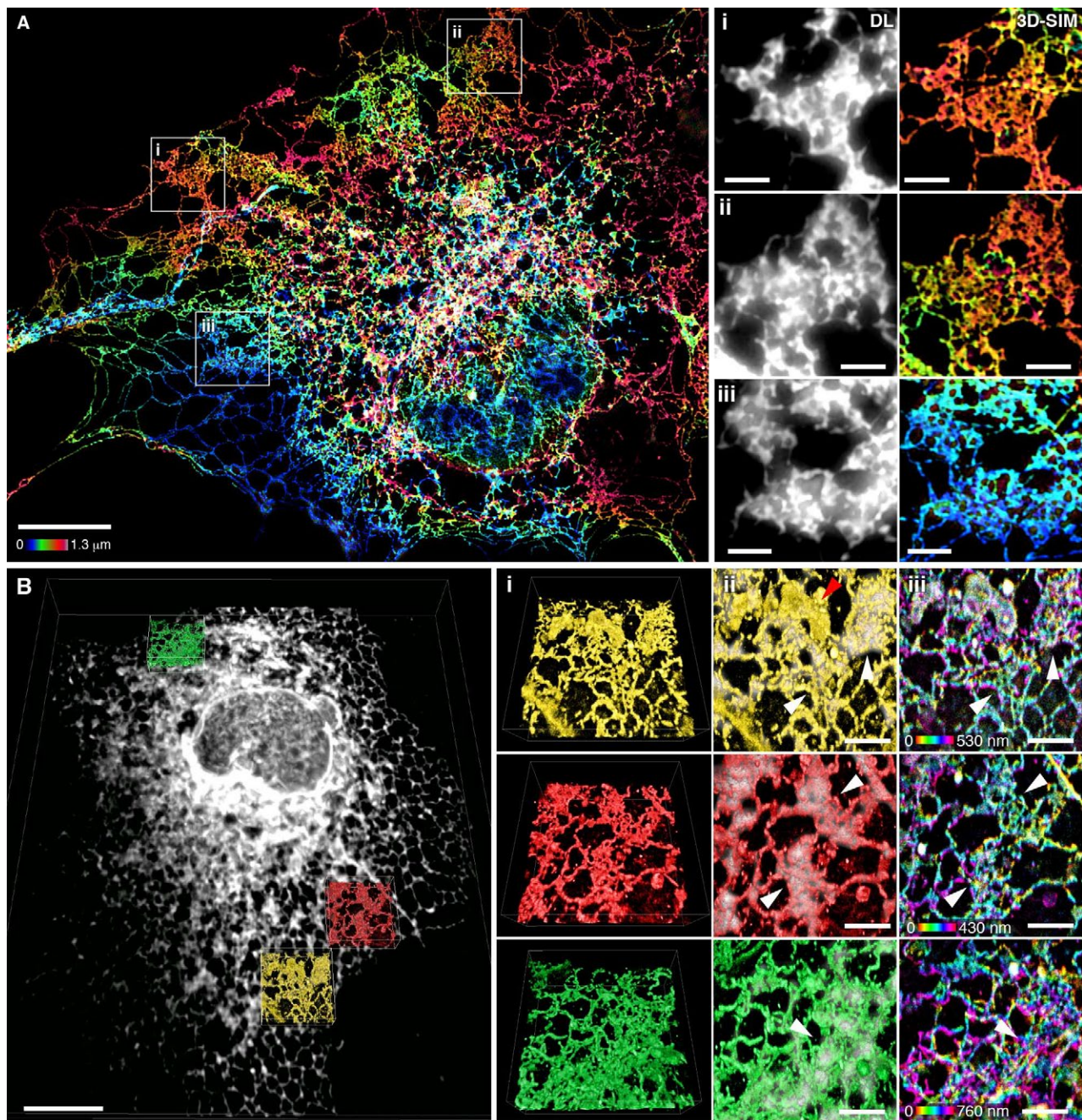


**Fig. 3. Many peripheral structures classically identified as sheets are instead dense matrices of tubules. (A)** Left: Fixed COS-7 cell expressing Sec61 $\beta$ , imaged by 3D-SIM and color-coded by z position. Scale bar, 10  $\mu$ m. Right: Magnified regions (i to iii) show that 3D-SIM reveals dense tubular matrices, which appear as sheets by diffraction-limited (DL) epifluorescence. Scale bars, 2  $\mu$ m. **(B)** Left: Deconvolved, diffraction-limited LLS imaging of a fixed COS-7 cell overexpressing Sec61 $\beta$  (gray). All internal lipid membranes were

reconstructed using LLS-PAINT microscopy. Data from three regions containing ER matrices are shown in colored insets. Scale bar, 10  $\mu$ m. Right: The three boxed regions are enlarged, showing (i) 3D orientation of LLS-PAINT volume rendering, (ii) overlay of LLS-PAINT and diffraction-limited LLS imaging volume rendering (gray), and (iii) LLS-PAINT color-coded by z position. White arrowheads mark areas that appear as sheets by diffraction-limited imaging; the red arrowhead [top of (ii)] denotes a mitochondrion. Scale bars, 2  $\mu$ m.

misinterpretation as sheets. To test this directly, we compared images of peripheral ER matrices collected by either diffraction-limited GI or GI-SIM using two different simulated exposure times (see materials and methods for details) (Fig. 4A). We found that the loss of either spatial or temporal resolution was sufficient to obscure the majority of gaps between tubules within the matrix.

In the case of live-cell imaging, tubular motion can occur faster than the acquisition time of a single frame, creating a blurring artifact and thus increasing the apparent diameter of tubules as the temporal resolution decreases (Fig. 4B and tables S5 and S6). Likewise, the resolvable separation between tubules in a matrix is affected not only by the true distance across the space be-

tween tubules, but also by temporal blurring due to oscillations of the surrounding tubules and motion of their three-way junctions. We therefore expected gaps in tight tubular matrices to appear smaller in active, living cells than in fixed ones. Indeed, the average apparent distance between tubules in fixed 3D-SIM (220 nm) was greater than that observed using live GI-SIM

(150 nm). Consequently, we predicted that decreasing temporal resolution would preferentially blur smaller spaces, as tubular oscillations and junction movement would mask them more readily. To quantify this, we summed GI-SIM images of tubular matrices over an increasing number of 25-ms frames to simulate longer exposure times. As predicted, longer simulated exposure times resulted in blurring of matrices until they ultimately resembled continuous sheets (Fig. 4D). On the other hand, improving temporal resolution decreased the minimum distance required between tubules before a space became detectable (Fig. 4E and tables S5 and S6), thereby increasing the density of measurable spaces within a dynamic matrix (Fig. 4F and tables S5 and S6).

To quantify the contribution of insufficient spatial resolution in obscuring the structure of ER tubular matrices, we compared cells in the absence of motion (i.e., in fixed cells) using three different imaging modalities of varying spatial resolution (diffraction-limited GI, 3D-SIM, or LLS-PAINT) (Fig. 4G). Predictably, improvements in spatial resolution decreased the measurable diameter of ER tubules (Fig. 4C and tables S5 and

S6). Moreover, imaging with diminishing spatial resolution limited the detectable degree of separation of tubules in a matrix (Fig. 4H and tables S5 and S6), decreasing their detectable density (Fig. 4I and tables S5 and S6). Thus, sufficient spatial and temporal resolution are both required to resolve the fine structure of tubular matrices in living cells, and with any imaging modality an apparently continuous structure may conceal spaces if they are beneath the resolvable power of the technique.

### FIB-SEM reveals tubular matrices with heterogeneous topology

To overcome the limitations of optical microscopy in resolving the very fine structure of tubular matrices, we studied their morphology by electron microscopy (EM). FIB-SEM was performed in native, untransfected cells to provide an additional control against the possibility that overexpression of both Sec61 $\beta$  and ER3 coincidentally induces matrices. The conditions used for FIB-SEM were selected to result in 8-nm steps in the  $z$  position (see materials and methods), which provides extremely high resolution in the  $z$  dimension and ensures that even thin structures

such as tubular matrices can be captured (Fig. 5A). This fine  $z$  resolution allowed the reconstruction of remarkably intricate 3D tubular structures even within very thin sections of the cell (Fig. 5B and Movie 1). In contrast, we found that the topological complexity of matrices in the  $z$  dimension would be lost with diffraction-limited confocal imaging, as nearly the entire structure shown in Fig. 5B falls within the focal plane of a single confocal slice. Indeed, a projection of a theoretical confocal image derived from the EM data in Fig. 5B (see materials and methods) results in an image indistinguishable from that of an intact ER sheet (Fig. 5B, green footprint). In agreement with the LLS-PAINT data described above, we found that these structures can contain substantial vertical topology even within a thin space, and a single slice through the structure often revealed only a few isolated tubules (Fig. 5A). Inspection of the FIB-SEM data also revealed heterogeneity in matrix structures, from highly convoluted 3D structures to nearly planar arrays of tubes (e.g., Fig. 5B versus Fig. 5C). Additionally, some matrices were incredibly tightly clustered, with spaces less than 50 nm between tubules (Fig. 5C). As such, it

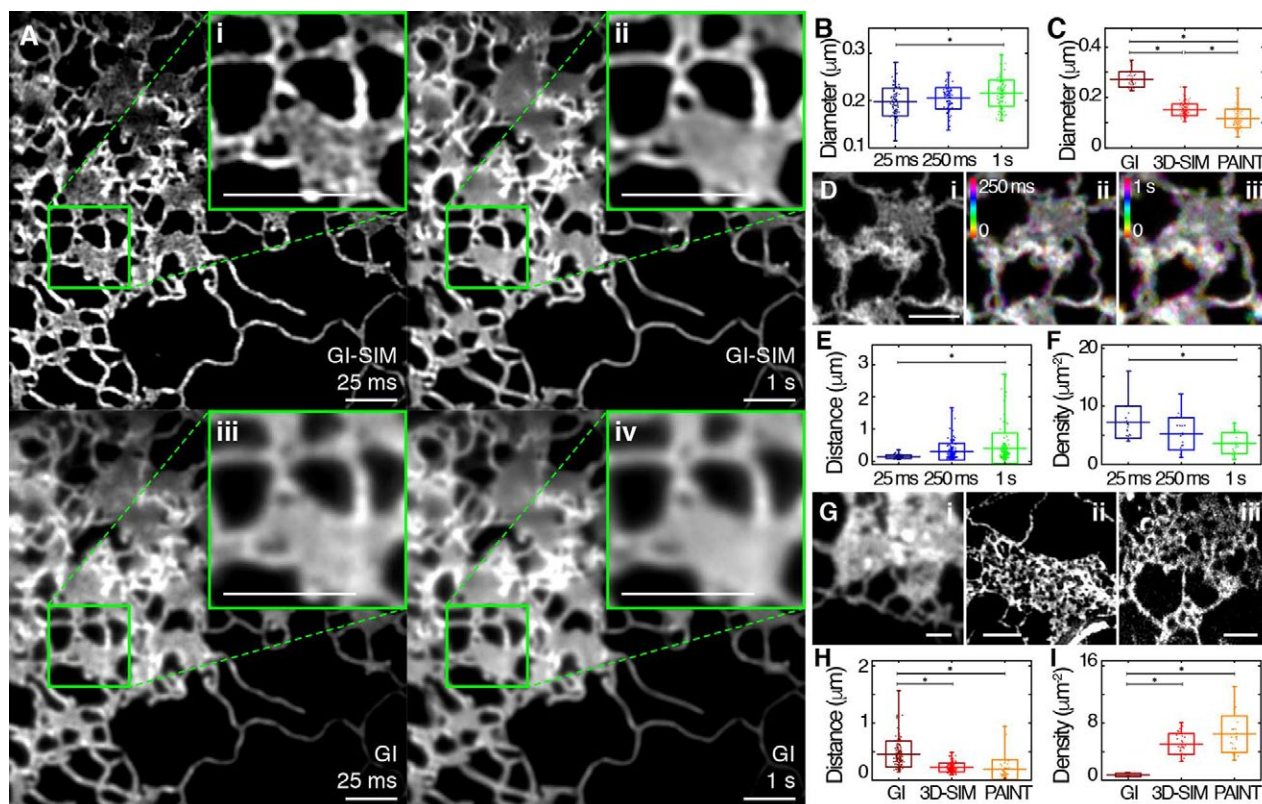


**Fig. 4. Effects of spatiotemporal blurring on imaging ER tubular matrices.** (A) A COS-7 cell expressing Sec61 $\beta$ , imaged live using GI-SIM, showing both single 25-ms frames (i, iii) and 40 frames averaged over 1 s (ii, iv). The top row shows the GI-SIM images; the bottom row shows the corresponding diffraction-limited images with GI illumination, demonstrating the combined effects of spatial and temporal limitations in resolution. (B and C) The measurable diameter of isolated ER tubules found outside of matrices also decreases with increasing temporal (B) and spatial (C) resolution. (D) Structure of a representative tubular ER matrix imaged in a live cell by GI-SIM when integrating image frames for (i) 25 ms (1 frame), (ii) 250 ms (10 frames), or (iii) 1 s (40 frames)

as in (A). (E and F) Quantification of the measurable distance between tubules (E) and density of these spaces (F) within tubular matrices for each functional exposure time. (G) Representative images of tubular matrices imaged in fixed cells by diffraction-limited GI (i), 3D-SIM (ii), and LLS-PAINT (iii). (H and I) Quantification of the measurable distance between tubules (H) and density of these spaces (I) in tubular matrices, as identified by imaging modalities of increasing spatial resolution. Scale bars, 2  $\mu$ m. Box plots indicate the mean and SD in all panels; range is indicated by outer tick marks. The asterisks denote statistical significance between the means, as detailed in tables S5 and S6.

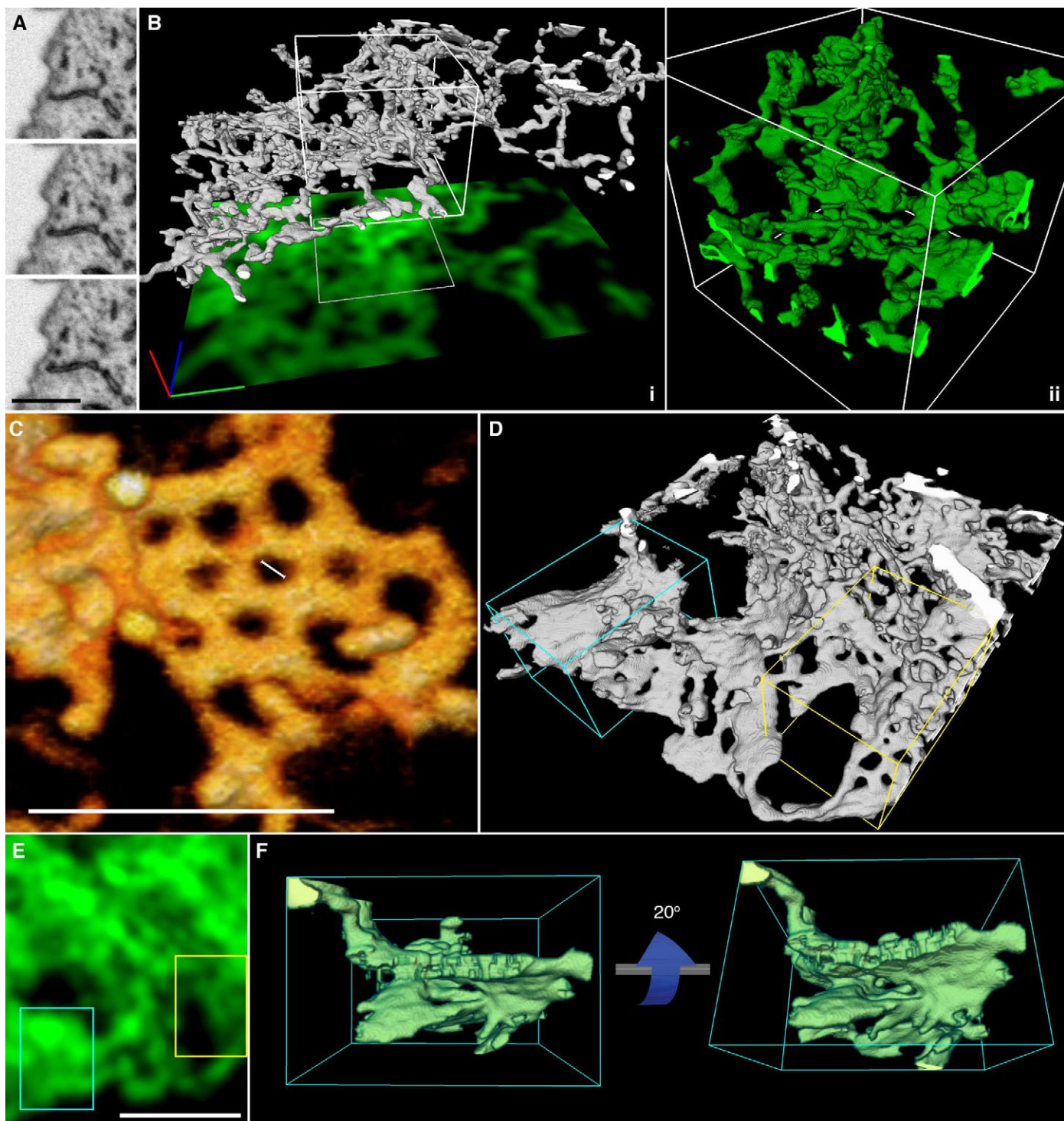


**Fig. 5. ER tubules form highly convoluted and intricate structures within the resolvable volume limits of any optical imaging technique.** (A) Three consecutive FIB-SEM slices through an ER matrix spaced by 8 nm. Scale bar, 1  $\mu\text{m}$ . (B) Three-dimensional reconstruction of a tubular matrix in a thin section (~600 to 1200 nm between the plasma membranes) of the cell. (i) The footprint shows the theoretically highest resolution that could be achieved with a single confocal slice through the structure directly shown above. Scale bar, 1  $\mu\text{m}$  in each direction. (ii) Close-up of the reconstruction of the boxed region in

(i). (C) 3D rendering of raw EM data showing an example of an approximately planar ER matrix with subresolution spaces (large scale bar, 500 nm; small scale bar, 50 nm). (D) 3D rendering of the ER at the border of perinuclear and peripheral regions of the cell, showing stacked helicoidal sheets (cyan box) and ER matrices (yellow box). (E) A theoretical confocal image of the structure, showing the difficulty in distinguishing these structures by diffraction-limited imaging. (F) Views from the side of a stacked helicoidal sheet in the perinuclear region of the ER [from cyan box in (D)], showing the pitch of the intact membranes.

would be impossible to resolve these structures as distinct from sheets by SIM, and it would be difficult to do so even by LLS-PAINT.

Generally, areas of flat continuous membrane are described as having net zero curvature, whereas highly curved regions of membrane have either net positive or negative curvature (7). In addition to the aforementioned tubular matrices, we also observed a number of structures in the ER that show local regions of near-zero curvature in the ER membrane. The largest of these regions are in true stacked ER sheets near the nucleus (Fig. 5D, cyan box), which have been described extensively (16). When imaged with diffraction-limited techniques, these structures are nearly impossible to differentiate from tubular ER matrices (Fig. 5, D and E). We also observed that whenever stacked sheets are seen, they appear to be connected by membrane “ramps” [as described in (16)] and generally are close to the nucleus, where the cell height is much greater than in the periphery (Fig. 5F and movie S5).

### Localizing ER-shaping proteins to tubular matrices

Given the highly variable and complex nature of ER matrices identified in the FIB-SEM data, we speculated that examining the distribution of well-characterized ER-shaping proteins may provide insights into the diversity of these structures. ATL GTPases have been well characterized as three-way junction-forming proteins localized within ER tubules, where they also bind ER-shaping RTNs (17, 18). Thus, although they would not be expected to be enriched in sheets, they would be expected in matrices composed of densely packed tubules and three-way junctions. We transfected COS-7 cells with HaloTag-ATL1 (one of three human ATL paralogs) and assessed the localization of ATL1 in live cells by means of diffraction-limited confocal microscopy (Fig. 6A). ATL1 was present in all structures classically considered as peripheral sheets. This was verified by immunostaining of endogenous ATL3 in HeLa cells (Fig. 6B).

Overexpression of ATLs was previously shown to induce massive proliferation of “aberrant sheet-like structures” in a GTPase-dependent manner (17). This finding has been difficult to explain in light of the known role of ATL GTPases as mediators of three-way junction formation between tubules. We hypothesized that ATL overexpression might drive the formation of increasingly dense tubular matrices, which would appear as peripheral sheets under standard confocal imaging because of insufficient spatiotemporal resolution. COS-7 cells coexpressing Sec61 $\beta$  and HaloTag-ATL1 were fixed and imaged using both diffraction-limited epifluorescence and 3D-SIM (Fig. 6C). Epifluorescence revealed the presence of peripheral sheet-like structures (Fig. 6C, i), as previously reported (17). However,

the improved spatial resolution offered by 3D-SIM showed these “aberrant sheet-like structures” to be dense tubular matrices (Fig. 6C, ii). These matrices contained ATL1 throughout (Fig. 6C, iii). Collectively, these data suggest that overexpression of ATLs does not drive formation of aberrant sheets, but rather induces the formation of dense tubular matrices, consistent with the known cellular functions of ATLs.

We also looked at the distributions of other proteins associated with driving or stabilizing particular ER shapes. RTNs are a highly conserved

strated in some peripheral sheet-like structures (2) (fig. S3). This complex heterogeneity in protein localization across matrices is unlikely to be a staining artifact, as overexpression of CLIMP63 or a variety of RTN isoforms also resulted in the presence of these proteins in some, but not all, ER matrices (fig. S3 and supplementary text). It is possible that heterogeneity in the distribution of these proteins is linked to the highly variable topologies shown in Fig. 5, which may correspond to functionally distinct classes of structures that appear identical when imaged with insufficient resolution.

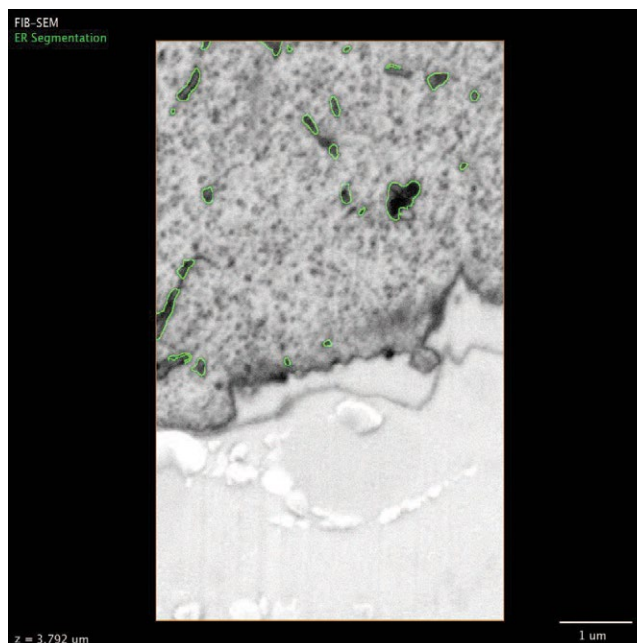
To explore whether our observations hold true for multiple cell types, we examined the structure of the ER in three dimensions using either 3D-SIM or Airyscan in a variety of cell lines with highly variant morphology and diverse organisms and tissues of origin. In all 10 cell lines examined, peripheral ER matrices were visible (Fig. 7). Although across cell types there seems to be substantial variation in the topology, density, and cellular location of these structures, they are uniformly present and clearly visible using either of the two independent imaging techniques.

### Discussion

Taken together, our data indicate that most previously described “sheet-like” ER structures within the thin periphery of cells are actually dense tubular matrices. Limitations in spatiotemporal resolution using conventional microscopy result in their appearance as continuous or fenestrated sheets. Additionally, we show a previously uncharacterized, rapidly dynamic state in the peripheral ER that is broadly dependent on cellular energy sources and that contributes to the misidentification of ER matrices in living cells.

Why would the peripheral ER be organized in this way? The structural conformation of tubular matrices is likely to be imperative to multiple features of ER biology, such as the ability of the ER to rapidly alter its conformation in response to changing cellular needs. Interconversions among loose polygonal networks and dense matrices could be accomplished by simply sliding tubules along one another, rather than requiring energetically costly fusion or fission of ER membranes. This rapid interconversion between loose and tight polygonal arrays of tubules (e.g., movie S3) is likely to be important in enabling the ER to rapidly reconfigure its spatial footprint in response to intracellular structural rearrangements or cell shape changes, or during cell migration. Indeed, the ER and cytoskeleton coexert a driving force for cytoplasmic streaming during cell expansion in *Arabidopsis*, and this is altered in mutants in which ER morphology is affected (21).

Clustering of tubules into tight arrays of three-way junctions might also function to decrease curvature stress across the ER, because the negative curvature of three-way junctions could help



**Movie 1. Three-dimensional reconstruction of FIB-SEM data reveals a convoluted ER matrix.** Raw 2D FIB-SEM data of ER tubules are shown in a series of sequential planes. The ER is segmented in green; the 3D reconstruction is shown, revealing an ER matrix. When confocal resolution is simulated, the convoluted nature of the structure is masked.

family of ER proteins sharing substantial sequence homology; multiple isoforms are present in most cell types and are typically associated with inducing and maintaining the curvature of the ER membrane in tubules (3). Classic work in the field has demonstrated localization of RTNs to tubular structures and their exclusion from sheet-like structures (19, 20). Conversely, CLIMP63 is a traditional marker used to identify ER sheets, as it is believed to be involved in stabilizing the diameter of the ER lumen through interactions between long, dimeric coiled-coil domains (2). U-2 OS cells expressing Sec61 $\beta$  were stained with antibodies to endogenous CLIMP63 and RTN4A/B and imaged using Airyscan, a technique capable of achieving subdiffraction-limited imaging independent of SIM. In concordance with their tubular nature, many peripheral ER matrices were found to be positive for RTN4A/B, and some of these were also enriched in CLIMP63 (Fig. 6D). There are also a smaller number of ER matrices that exclude RTN4A/B staining, as has been previously demon-

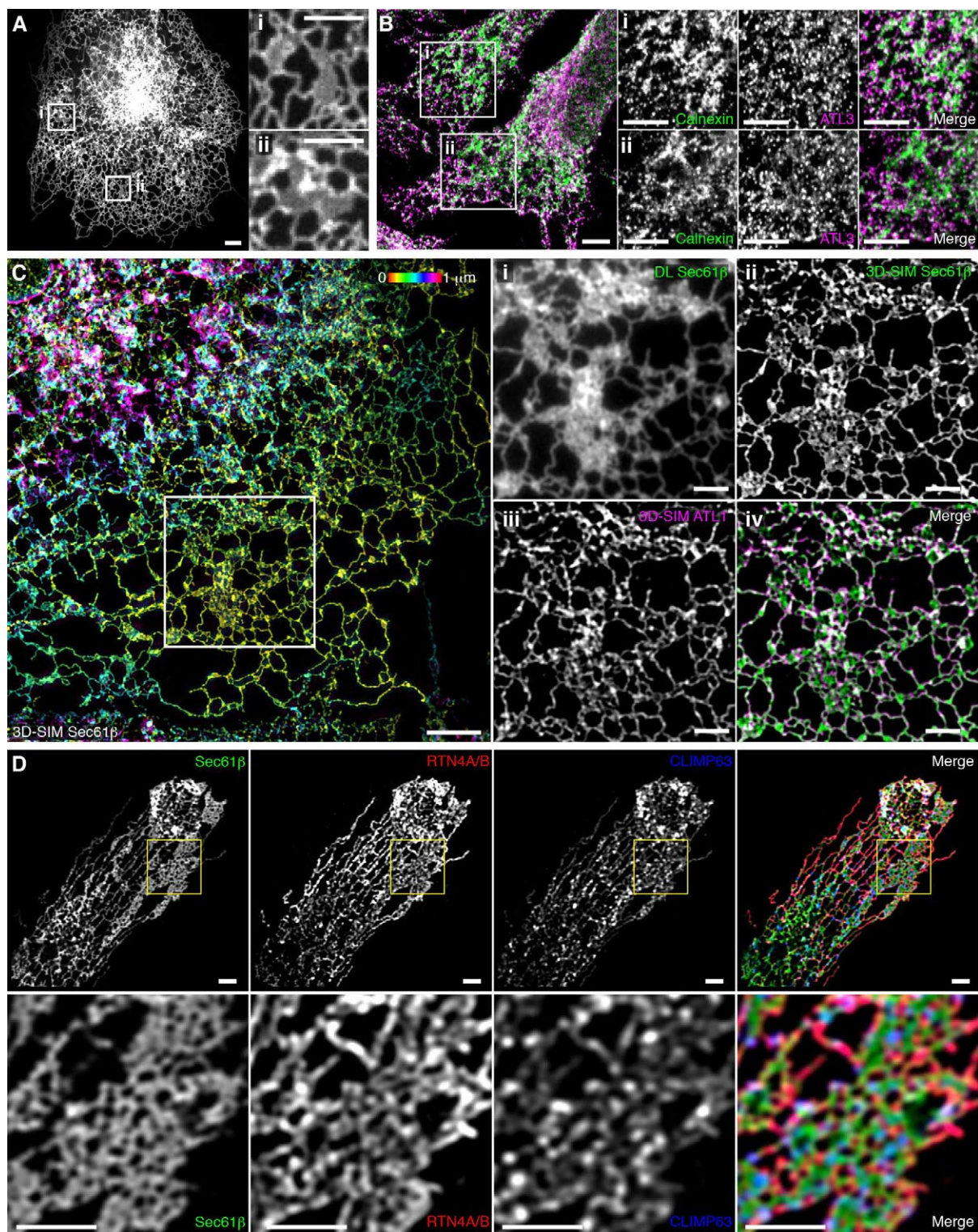


**Fig. 6. Localization of ER-shaping proteins within dense tubular matrices.**

(A) COS-7 cell expressing low levels of HaloTag-ATL1 imaged live with conventional spinning disk microscopy. Boxed regions (i) and (ii) demonstrate ATL1 localization throughout structures that appear to be peripheral sheets by spatiotemporally limited imaging techniques. (B) Left: A fixed HeLa cell acquired with conventional scanning point confocal microscopy, stained for the endogenous ER marker calnexin and endogenous ATL3 (merged image); boxed regions (i) and (ii) show endogenous ATL3 localization to structures that appear as sheets. Right: Regions shown in (i) and (ii) were stained for the

endogenous ER marker calnexin and endogenous ATL3. (C) A fixed COS-7 cell expressing Sec61 $\beta$  and HaloTag-ATL1 imaged by wide-field SIM. Sec61 $\beta$  fluorescence is color-coded by z position. Boxed region is enlarged in panels at right. Structures that appear as sheets by diffraction-limited imaging (i) are revealed to be dense tubular matrices (ii) that are positive for ATL1 (iii); the merged image of (ii) and (iii) is shown in (iv). (D) U-2 OS cell expressing Sec61 $\beta$  stained for endogenous RTN4A/B and CLIMP63 with the boxed region magnified (bottom row), illustrating localizations of both proteins within a tubular matrix. Merged images are at the far right. Scale bars, 2  $\mu$ m.

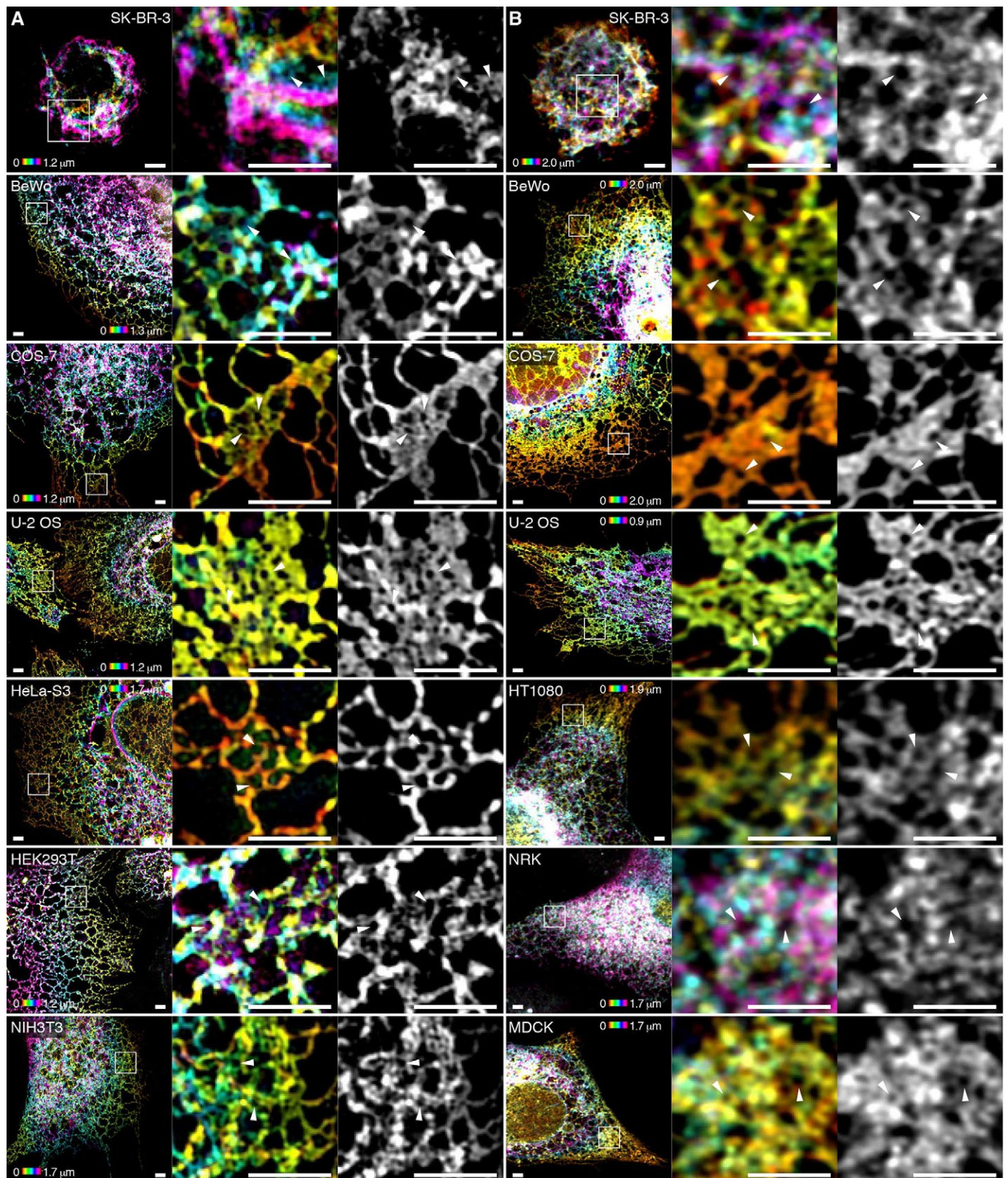


**Fig. 7. Tubular ER matrices are present in different cell types.** (A and B) Various cell lines expressing Sec61 $\beta$  were imaged using 3D-SIM (A) or, where fluorescence intensity was insufficient, Airyscan (B). The first four cell lines were imaged using both modalities, demonstrating that the dense matrix structures are not artifacts of any given imaging modality. Boxed regions highlighting representative tubular ER matrices in each cell type are magnified at the right. White arrowheads indicate subdiffraction-limited spaces between tubules. Scale bars, 2  $\mu$ m. The signal of Sec61 $\beta$  fluorescence is color-coded by z position in the left and center panels corresponding to each cell line and technique.

to neutralize the positive curvature associated with tubules (1). Thus, a relatively planar network could be formed (e.g., Fig. 5C) in the thin periphery of cells, where a lack of vertical space might prevent the formation of stacked helicoidal sheets (16). Dense ER matrices are also predicted to have greater membrane surface area than a flat sheet of similar dimensions, so they may allow storage of excess membrane proteins and lipids or provide increased surface for modulating lipid synthesis or protein folding. Such a tubular membrane reservoir may also be needed to facilitate the availability of ER membrane for modulating interactions with other organelles, such as mitochondria, lipid droplets, or endocytic compartments.

Our data do not conflict with the impressive literature describing the structures of flattened regions of the ER associated with specialized functions, such as the nuclear envelope (22), helicoidal stacks in the perinuclear region (16), or flattened cisternal structures close to the plasma membrane (23). Rather, these structures represent one end of a spectrum of curvatures across the ER membrane, with the other end of the spectrum dominated by more prevalent ER tubules and the dense tubular matrices we have described.

The heterogeneity observed in fine ultrastructure and ER protein content also suggests that there may be several distinct types of ER matrices. It is therefore possible that these different structures may carry out distinct functions. For instance, our FIB-SEM data support previous 3D EM reconstructions in suggesting that tubular morphology is far more heterogeneous than the cylindrical structures often depicted in models based on optical microscopy studies (24, 25). Tubules can also take on flattened or highly irregular structures along their lengths, as has been described in ER contact sites with the plasma membrane (23). There is no reason to think that tubules within ER matrices could not also undergo these sorts of deformations; hence, ER matrices close to the plasma membrane or other organelles (e.g., Fig. 3B) could potentially play important roles in rapidly facilitating calcium signaling or lipid transfer. These altered morphologies may also explain some of the variability in distribution of ER-shaping proteins across matrices, as structures may become too dense or too deformed to stably hold certain classes of ER proteins. These data may thus suggest another mechanism for modulating peripheral ER function. It seems clear, in any event, that given the pathogenic role of impaired ER shaping and protein distribution in disorders such as the hereditary spastic paraplegias (4), the ER structure and dynamics described here will have important implications for understanding both basic cell biology and disease pathogenesis.

## Materials and methods

### Plasmids and antibodies

Constructs expressing Myc- and HA-tagged  $\alpha$ -lastins have been previously described (26), with HaloTag-ATL1 purchased from Promega. Constructs expressing mEmerald-Sec61 $\beta$  and mApple-Sec61 $\beta$  were generated by replacing the GFP cassette of pAcGFP1-Sec61 $\beta$  (2) with corresponding fluorescent proteins, using flanking *AgeI* and

*BsrG1* restriction sites. Reticulon constructs were cloned from whole brain cDNA and inserted into pmCherry-C1 using the *BglII* and *SalI* restriction sites. Lifeact-mApple has been previously described (27), and mEmerald-ER-3 (ER3) was a gift from Michael Davidson (Addgene plasmid # 54082). ER3 consists of an ER lumen-targeting motif fused to mEmerald with a C-terminal KDEL tag.

Commercially available mouse monoclonal anti-Myc epitope (1:200; IgG<sub>1</sub>, clone 9E10; Santa Cruz Biotechnology) and rabbit polyclonal anti-HA epitope (1:200; IgG, clone Y-11; Santa Cruz Biotechnology) antibodies were used for immunocytochemistry. In addition, a custom affinity-purified mouse monoclonal anti-ATL3 (No. 6115, IgG, clone 9H2B12; residues 561–578; acetyl-CATVRDAVVGPRSPMDKKAQ-OH) antibody was used at 1:100. The anti-RTN4A/B antibody was a kind gift from Riqiang Yan, and was used as described previously (28). CLIMP63 was stained using a commercial antibody purchased from Enzo Lifesciences (1:250; IgG<sub>2a</sub>, clone G1/296).

### Cell culture, transfection, and plating

COS-7, U-2 OS and HeLa cells (ATCC) were grown in phenol red-free Dulbecco's Modified Eagle Medium (DMEM) supplemented with 10% (v/v) FBS (Corning), 2 mM L-glutamine, 100 U/ml penicillin and 100  $\mu$ g/ml streptomycin at 37°C and 5% CO<sub>2</sub>. MDCK cells were a line stably expressing ER-RFP (29, 30) generously provided by Erik Snapp. All other cells (SK-BR-3, BeWo, HeLa-S3, HEK293T, HT1080, NRK and NIH3T3) were grown according to manufacturer's specifications (ATCC).

Coverslips and chambers were pre-coated with 400–600  $\mu$ g/ml Matrigel (Corning), and cells were seeded to achieve ~60% confluency at the time of imaging. Transfections were executed using Lipofectamine 3000 (Thermo Fisher Scientific) according to the manufacturer's specifications. Fluorescently-tagged Sec61 $\beta$  alone was transfected at 1  $\mu$ g/ 35 mm chamber, or else cotransfected at a ~3–4:1 ratio with the additional plasmid. Imaging was performed between 14–22 hours post-transfection. Where indicated, HaloTag-ATL1 was labeled with JF549 as previously described (31), and cells were imaged immediately post-labeling.

### Drug treatments

All drugs used in the paper were purchased from Sigma Aldrich and used as has been described (32). Drugs were diluted from high concentration stocks reconstituted in DMSO, and diluted to the appropriate concentration in complete medium unless otherwise indicated. Cycloheximide (CHX) and Puromycin (Puro) were used at a final concentration of 100  $\mu$ g/ml, Nocodazole (NZ) was used at 30  $\mu$ M, and Blebbistatin (Bleb) was used at a final concentration of 50  $\mu$ M. ATP depletion was accomplished by incubating the cells for one hour in 10 mM 2-deoxyglucose (DOG) and 2 mM sodium azide (NaN<sub>3</sub>) in PBS at 37°C, and AIF treatment was performed as previously described (33) in HBSS. HBSS-only controls were also run for all experiments using AIF, and no difference in any phenotype studied was seen compared to untreated controls (data not shown).

### Immunocytochemistry

For immunocytochemistry staining, cells were seeded into No. 1.5 imaging chambers (Lab-Tek) coated with Matrigel, and then fixed with 4% (w/v) paraformaldehyde (PFA) for 20 min at room temperature (RT). Cells were then permeabilized with 0.2% (w/v) saponin (Sigma-Aldrich) for 30 min, and blocked in 5% (v/v) donkey serum (Sigma-Aldrich) doped with 0.05% (w/v) saponin for 1 hour at RT. Primary antibodies were diluted in block to the aforementioned concentrations, added to samples, and incubated overnight at 4°C. Secondary anti-mouse and anti-rabbit antibodies conjugated to Alexa 488, Alexa 555 (1:1000; Life Technologies) were made in block and incubated with samples for 30 min at RT. Imaging was performed in fresh PBS.

### Confocal microscopy

Live-cell confocal imaging was performed using a customised Nikon TIE inverted scope outfitted with a Yokogawa spinning-disk scan head (#CSU-X1, Yokogawa) and a Photometrics EM-CCD camera (Evolve 512) with 500 ms exposure time. Fluorescence was collected using a 60 $\times$  Plan-Apochromat 1.40 NA oil objective (Nikon) with the additional use of a 1.5 $\times$  optovar to create a final pixel size of 130 nm. Cells were imaged in DMEM and incubated with a LiveCell Imaging Chamber (Nikon) at 37°C and 5% CO<sub>2</sub>.

Fixed-cell confocal microscopy was performed using a Zeiss 780 laser scanning confocal microscope equipped with a 32-channel multi-anode spectral detector. Excitations were performed sequentially using 405, 488, 561, or 633 nm lines as needed, and imaging conditions were experimentally selected to minimize crosstalk. The resulting fluorescence was collected using a 100 $\times$  Plan-Apochromat 1.4 NA oil objective (Carl Zeiss) and images were prepared using the commercial Zen software package (Carl Zeiss).

Airyscan imaging was performed in fixed cells using a Zeiss 880 outfitted with an Airyscan module. Cells were seeded onto matrigel-coated coverslips, fixed in 4% (w/v) PFA supplemented with 0.2% (w/v) glutaraldehyde at RT for 20 min. After fixation, cells were washed in RT PBS and imaged in clean PBS. Data was collected using a 63 $\times$  1.4 NA objective and immersion oil optimized for 30°C (Carl Zeiss). Colors were collected sequentially to minimize crosstalk, and Airyscan processing was performed using the Airyscan module in the commercial ZEN software package (Carl Zeiss).

### Structured illumination microscopy (SIM)

Fixed cell, 3D-SIM was performed using a commercial Zeiss microscope (ELYRA SR-SIM, Carl Zeiss Microimaging) outfitted with a Plan-Apochromat 63 $\times$  1.4 NA objective lens. Samples were fixed in 4% PFA supplemented with 0.1% glutaraldehyde at RT for 20 min. Cells were imaged in PBS at RT with a final pixel size of 40 nm and 110 nm  $z$  plane spacing using three rotations of the SIM grating. SIM processing was performed using the SIM module in the Zen software package (Carl Zeiss Microimaging), and multicolor images were channel aligned using a matrix generated with Tetraspeck beads (Life

Technologies) imaged on the same day as the cells.

### Grazing incidence-structured illumination microscopy (GI-SIM)

GI-SIM was performed in a high speed SIM microscope previously adapted for total internal reflection fluorescence (TIRF)-SIM (34). GI-SIM shared the same beam path configuration as the high-speed TIRF-SIM system. In TIRF illumination mode, because the intensity of evanescent wave of excitation light exponentially decayed from the interface between cover slip and cell sample, the characteristic penetration depth of the evanescent wave limited the TIRF-SIM imaging depth to around 100 nm (34), in which much of the ER network lies outside. In order to increase the imaging depth, it is straightforward to tune down the incident angle that is inversely proportional to the penetration depth of the evanescent wave (34). We realized that when the incident angle was tuned to slightly smaller than the critical angle, where the refraction angle at the interface was near 90 degrees, and the refracted light grazed the surface of the cover slip, the grazing incident light actually formed a thin light sheet parallel to the cover slip surface. The thin light sheet intensity remained constant in both lateral and axial directions, and its thickness could be adjusted by tuning the incident angle of excitation light. The optimum thickness of grazing incident light sheet should match the depth-of-focus of the high NA objective (Zeiss alpha Plan-Apochromat 100x/1.57 Oil-HI), which is around 700 nm. To implement GI-SIM, we used the grating pattern generation algorithm previously developed for patterned activation nonlinear SIM. It permitted us to finely tune the incident angle of excitation light, i.e., the period of illumination pattern (34). We identified the optimum incident angle by keeping the out-of-focus background of the TIRF image as little as possible, meanwhile observing as much ER structure as possible. After we identified the critical angle for grazing incidence, the raw image acquisition and SIM image reconstruction procedure is the same as TIRF-SIM (34). Time-lapse images were also subject to a traditional bleach correction algorithm by histogram matching in ImageJ (NIH). Cells were plated and transfected on Matrigel-coated high-NA coverslips (Zeiss) and imaging was performed the following day.

### Lattice light sheet-point accumulation for imaging in nanoscale topography (LLS-PAINT)

LLS-PAINT was performed as described elsewhere (14) using a custom built Lattice Light Sheet microscope (15). Membrane labeling was performed sequentially with BODIPY-TR (LifeTechnologies) followed by AZEP-Rh (31) to label intracellular membranes and carried out over 14 days total. The final image was reconstructed from 548,792,627 individual molecular localizations with a median precision of 7.2 nm laterally and 41.0 nm axially. Immediately prior to PAINT imaging, a diffraction limited dithered LLS image of mEmerald-Sec61 $\beta$  was taken for comparison in the same cell.

### Electron microscopy (EM)

In preparation for EM, cells were grown in 100 mm culture dishes (Corning) in standard cell culture conditions. Cells were fixed in 2% (w/v) glutaraldehyde in 0.08 M cacodylate buffer for one hour. Cells were then post-fixed with osmium according to a modified ROTO (reduced osmium thiocarbonylhydrazide-osmium) protocol (35). Briefly, fixation was performed in 1% (w/v) OsO<sub>4</sub> in 0.1 M cacodylate buffer for 30 min on ice, followed by a wash in cacodylate buffer. The cells were then incubated with 1% (w/v) thiocarbonylhydrazide in water for 10 min at room temperature, followed by immersion in 1% (w/v) OsO<sub>4</sub> in 0.1 M cacodylate for 30 min at 4°C. Cells were contrasted en bloc with 1% (v/v) uranyl acetate, dehydrated in ethanol, and embedded in Durcupan ACM (Fluka). FIB-SEM was performed using a Zeiss NVision40 Focused Ion Beam Scanning Electron Microscope. SEM and FIB milling steps were optimized to produce isotropic 8 nm voxels. The SEM image stack was acquired at 300 kHz/voxel using a 3-nA electron beam at 1.5 kV landing energy for imaging and a 30-kV gallium ion beam for FIB milling.

### Structured illumination microscopy reconstruction and Fourier filtering

SIM reconstruction was performed utilizing a modified reconstruction algorithm based on the previously described Gustafsson algorithm (36). During reconstruction, data was filtered in Fourier space using a variety of filters to minimize the appearance of reconstruction artifacts. This included at least a one log scan of the Wiener filter and a variety of suppression radii around the peaks at Abbe's limit (fig. S4), in addition to a variety of apodization functions designed to roll off the noise at the limit of resolution. While the first two filters were selected individually for each image, the apodization function was decided collectively for the data and applied to every image in the paper. The apodization function was a single Gaussian blur using a radius that is smaller than the resolution limit of the technique,  $\sigma = 45$  nm in real space. This allows most SIM reconstruction artifacts to be filtered out, maximizing the potential signal to noise with only a small price in functional resolution (fig. S4).

### Reconstruction of three-dimensional EM data

Three dimensional FIB-SEM data was reconstructed and the ER segmented using a pseudo-automated approach. First, images were prepped, cropped, and inverted using ImageJ, so that osmium signal appeared as fluorescence for subsequent analysis. Images were then loaded into Ilastik (37) for pixel classification. The pixel classification algorithm was used to generate a probability map for cellular membranes, based upon the osmium signal. A carving algorithm within Ilastik was then utilized. The resulting segmentation was overlaid onto the raw EM data using Amira (FEI) and quality checked by eye throughout each slice of the reconstruction. Simulation of serial section data was performed by simply summing the requisite number of FIB-SEM slices that would

have been present in a single slice acquired by serial section.

### Data visualization

Two dimensional image preparation and analysis was generally performed using ImageJ (NIH), and three dimensional image preparation was performed using Amira (FEI).

### Skeletonization

Skeletonization of images was performed using ImageJ (NIH). First, images were pre-processed using enhanced local contrast (CLAHE) to help flatten the intensity of the ER. The images were then manually thresholded, made binary, and skeletonized. Using the AnalyzeSkeleton (8) plugin in ImageJ, branches and junctions were determined from the skeletonized images. In short, skeletonized pixels with exactly two neighbors are considered branches and pixels with more than two neighbors, junctions.

### Analysis of tubule motion

After obtaining the skeletonized image, lines were drawn perpendicular to the skeletonized structure over a number of tubules that were to be analyzed. In order to avoid the confounding effects of junctions crossing the line, lines were placed on sections of tubule that were spatially separated from any junctions. Kymographs of the skeletonized data were then generated along the lines over a total time lapse of 100 frames (2.5 s) (see Fig. 1B, for example). Amplitude was extracted from the kymograph by using a custom written peak finding algorithm in Labview, then measuring the distance between the maximum and minimum of peaks of the skeleton during the kymograph's time window. The frequency was defined as the inverse of the period, which was measured by dividing the length of the time course by the number of paired maxima and minima within the data.

### Junction tracking

Junctions were determined directly from the AnalyzeSkeleton plugin in ImageJ. Junctions from the tagged skeleton output of the AnalyzeSkeleton plugin typically occupy 1-5 pixels. The binary junction images were smoothed with a Gaussian kernel having a standard deviation of 1.0 pixel, resulting in single-particle-like images. The resulting images were then fed directly into the u-track SPT software (13).

### Mean square displacement analysis

Trajectories, with a lifetime of at least 10 frames (0.25 s) were obtained. The trajectories were characterized through their mean square displacement (MSD).  $MSD = (1/T) \sum_{t=1}^T (r(t) - r_0)^2$ , where  $T$  is the total movie time and  $r$  the displacement. The MSD can be described as  $MSD \sim t^\alpha$  where  $\alpha$  can be used to describe a particle's motion as Brownian ( $\alpha = 1$ ), subdiffusive ( $\alpha < 1$ ), or superdiffusive ( $\alpha > 1$ ) (10).

### Kymographs

Kymographs were prepared from time lapse images by manually drawing lines across the

image and using the standard reslice package in ImageJ. The resulting figure represents the intensity by pixel along the line graphed against time. Axes are labeled to indicate the respective  $x$  ( $\mu\text{m}$ ) and  $t$  (s).

### Tracking spaces in sheets

GI-SIM images of the ER were cropped such that the ROI was an individual sheet. The area outside of the sheet was then subtracted and the intensity of the images inverted. The transformation resulted in local intensity minima (spaces) becoming local intensity maxima. These maxima were then directly entered into the u-track SPT algorithm.

### Space lifetime and density

Track length corresponds to the lifetime of the spaces. To account for clipping of lifetimes at either the start or end of the movie, the distribution of lifetimes was corrected following Loerke and colleagues (38, 39). To measure the density of spaces, the area of each sheet was measured by drawing a freehand ROI around the sheet and then measuring the area of the ROI in ImageJ. The density of spaces was then calculated as the number of spaces within the sheet divided by the area of that particular sheet.

### Temporal intensity derivative

The derivative was calculated by choosing a defined region and time series of interest and processing the data as described for GI-SIM (fig. S1A). Each frame of the time-lapse image was then subtracted pixel by pixel from the following frame using a floating 32-bit depth pixel to ensure negative signals were not lost (fig. S1B). The resulting image was squared on a per-pixel basis, to make all changes positive integers (fig. S1C). The upper limit of the dynamic range was reset to the theoretical maximum in order to normalize the derivative between samples. The resulting time-lapse image was temporally color coded, yielding a spatial map of the change in fluorescence intensity over time (fig. S1D).

### Measuring the diameter of tubules and spaces in matrices

The size of apparent spaces within tubular matrices was measured by fitting the intensity cross-section profile of each minima to a Gaussian curve. The full width at half-maximum of the Gaussian curves provides a good estimate of the distance across the space. The diameter of tubules was measured in a similar fashion: intensity cross-sections along several locations of tubules were fit to a Gaussian curve and the full width at half-maximum was reported as the diameter of the tubule.

### Temporal blurring

To simulate the effects of longer exposure times in GI-SIM, the appropriate number of SIM frames collected at 40 Hz were merged using a simple sum projection in ImageJ. Thus, 250 ms images are the sum of 10 individual 25 ms frames, and 1 s images are the sum of 40 separate 25 ms frames. When color-coding by frame is shown, the temporal color code projection tool was used in place of the simple sum projection.

## REFERENCES AND NOTES

1. T. Shemesh *et al.*, A model for the generation and interconversion of ER morphologies. *Proc. Natl. Acad. Sci. U.S.A.* **111**, E5243–E5251 (2014). doi: 10.1073/pnas.1419997111; pmid: 25404289
2. Y. Shibata *et al.*, Mechanisms determining the morphology of the peripheral ER. *Cell* **143**, 774–788 (2010). doi: 10.1016/j.cell.2010.11.007; pmid: 21111237
3. U. Goyal, C. Blackstone, Untangling the web: Mechanisms underlying ER network formation. *Biochim. Biophys. Acta* **1833**, 2492–2498 (2013). doi: 10.1016/j.bbamcr.2013.04.009; pmid: 23602970
4. C. Blackstone, Cellular pathways of hereditary spastic paraplegia. *Annu. Rev. Neurosci.* **35**, 25–47 (2012). doi: 10.1146/annurev-neuro-062111-150400; pmid: 22540978
5. C. Lee, L. B. Chen, Dynamic behavior of endoplasmic reticulum in living cells. *Cell* **54**, 37–46 (1988). doi: 10.1016/0092-8674(88)90177-8; pmid: 3383243
6. A. R. English, G. K. Voeltz, Rab10 GTPase regulates ER dynamics and morphology. *Nat. Cell Biol.* **15**, 169–178 (2013). doi: 10.1038/ncb2647; pmid: 23263280
7. D. Li *et al.*, Extended-resolution structured illumination imaging of endocytic and cytoskeletal dynamics. *Science* **349**, aab3500 (2015). doi: 10.1126/science.aab3500; pmid: 26315442
8. I. Arganda-Carreras, R. Fernández-González, A. Muñoz-Barrutia, C. Ortiz-De-Solorzano, 3D reconstruction of histological sections: Application to mammary gland tissue. *Microsc. Res. Tech.* **73**, 1019–1029 (2010). doi: 10.1002/jemt.20829; pmid: 20324655
9. S. Chen *et al.*, Lunapark stabilizes nascent three-way junctions in the endoplasmic reticulum. *Proc. Natl. Acad. Sci. U.S.A.* **112**, 418–423 (2015). doi: 10.1073/pnas.1423026112; pmid: 25548161
10. R. Metzler, J. Klafter, The random walk's guide to anomalous diffusion: A fractional dynamics approach. *Phys. Rep.* **339**, 1–77 (2000). doi: 10.1016/S0370-1573(00)00070-3
11. M. Guo *et al.*, Probing the stochastic, motor-driven properties of the cytoplasm using force spectrum microscopy. *Cell* **158**, 822–832 (2014). doi: 10.1016/j.cell.2014.06.051; pmid: 25126787
12. C. Kural *et al.*, Tracking melanosomes inside a cell to study molecular motors and their interaction. *Proc. Natl. Acad. Sci. U.S.A.* **104**, 5378–5382 (2007). doi: 10.1073/pnas.0700145104; pmid: 17369356
13. K. Jaqaman *et al.*, Robust single-particle tracking in live-cell time-lapse sequences. *Nat. Methods* **5**, 695–702 (2008). doi: 10.1038/nmeth.1237; pmid: 18641657
14. W. R. Legant *et al.*, High-density three-dimensional localization microscopy across large volumes. *Nat. Methods* **13**, 359–365 (2016). doi: 10.1038/nmeth.3797; pmid: 26950745
15. B.-C. Chen *et al.*, Lattice light-sheet microscopy: Imaging molecules to embryos at high spatiotemporal resolution. *Science* **346**, 1257998 (2014). doi: 10.1126/science.1257998; pmid: 25342811
16. M. Terasaki *et al.*, Stacked endoplasmic reticulum sheets are connected by helical membrane motifs. *Cell* **154**, 285–296 (2013). doi: 10.1016/j.cell.2013.06.031; pmid: 23870120
17. J. Hu *et al.*, A class of dynamin-like GTPases involved in the generation of the tubular ER network. *Cell* **138**, 549–561 (2009). doi: 10.1016/j.cell.2009.05.025; pmid: 19665976
18. G. Orso *et al.*, Homotypic fusion of ER membranes requires the dynamin-like GTPase atlastin. *Nature* **460**, 978–983 (2009). doi: 10.1038/nature08280; pmid: 19633650
19. G. K. Voeltz, W. A. Prinz, Y. Shibata, J. M. Rist, T. A. Rapoport, A class of membrane proteins shaping the tubular endoplasmic reticulum. *Cell* **124**, 573–586 (2006). doi: 10.1016/j.cell.2005.11.047; pmid: 16469703
20. Y. Shibata *et al.*, The reticulon and DPL/Yoplp proteins form immobile oligomers in the tubular endoplasmic reticulum. *J. Biol. Chem.* **283**, 18892–18904 (2008). doi: 10.1074/jbc.M800986200; pmid: 18442980
21. G. Stefano, L. Renna, F. Brandizzi, The endoplasmic reticulum exerts control over organelle streaming during cell expansion. *J. Cell Sci.* **127**, 947–953 (2014). doi: 10.1242/jcs.139907; pmid: 24424025
22. M. W. Hetzer, The nuclear envelope. *Cold Spring Harb. Perspect. Biol.* **2**, a000539 (2010). doi: 10.1101/cshperspect.a000539; pmid: 20300205
23. R. Fernández-Busnadiego, Y. Saheki, P. De Camilli, Three-dimensional architecture of extended synaptotagmin-mediated endoplasmic reticulum-plasma membrane contact sites. *Proc. Natl. Acad. Sci. U.S.A.* **112**, E2004–E2013 (2015). doi: 10.1073/pnas.1503191112; pmid: 25787254
24. M. Puhka, M. Joensuu, H. Vihinen, I. Belevich, E. Jokitalo, Progressive sheet-to-tubule transformation is a general mechanism for endoplasmic reticulum partitioning in dividing mammalian cells. *Mol. Biol. Cell* **23**, 2424–2432 (2012). doi: 10.1091/mbc.E10-12-0950; pmid: 22573885
25. M. Puhka, H. Vihinen, M. Joensuu, E. Jokitalo, Endoplasmic reticulum remains continuous and undergoes sheet-to-tubule transformation during cell division in mammalian cells. *J. Cell Biol.* **179**, 895–909 (2007). doi: 10.1083/jcb.200705112; pmid: 18056408
26. P.-P. Zhu, C. Soderblom, J.-H. Tao-Cheng, J. Stadler, C. Blackstone, SPG3A protein atlastin-1 is enriched in growth cones and promotes axon elongation during neuronal development. *Hum. Mol. Genet.* **15**, 1343–1353 (2006). doi: 10.1093/hmg/ddl054; pmid: 16537571
27. J. Riedl *et al.*, Lifeact: A versatile marker to visualize F-actin. *Nat. Methods* **5**, 605–607 (2008). doi: 10.1038/nmeth.1220; pmid: 18536722
28. W. He *et al.*, Reticulon family members modulate BACE1 activity and amyloid- $\beta$  peptide generation. *Nat. Med.* **10**, 959–965 (2004). doi: 10.1038/nm1088; pmid: 15286784
29. C. W. Lai, D. E. Aronson, E. L. Snapp, BiP availability distinguishes states of homeostasis and stress in the endoplasmic reticulum of living cells. *Mol. Biol. Cell* **21**, 1909–1921 (2010). doi: 10.1091/mbc.E09-12-1066; pmid: 20410136
30. E. L. Snapp, A. Sharma, J. Lippincott-Schwartz, R. S. Hegde, Monitoring chaperone engagement of substrates in the endoplasmic reticulum of live cells. *Proc. Natl. Acad. Sci. U.S.A.* **103**, 6536–6541 (2006). doi: 10.1073/pnas.0510657103; pmid: 16617114
31. J. B. Grimm *et al.*, A general method to improve fluorophores for live-cell and single-molecule microscopy. *Nat. Methods* **12**, 244–250 (2015). doi: 10.1038/nmeth.3256; pmid: 25599551
32. N. B. Cole, Compendium of drugs commonly used in cell biology research. *Curr. Protoc. Cell Biol.* 00:1B.1B.1–1B.26 (1998).
33. J. G. Donaldson, R. A. Kahn, J. Lippincott-Schwartz, R. D. Klausner, Binding of ARF and beta-COP to Golgi membranes: Possible regulation by a trimeric G protein. *Science* **254**, 1197–1199 (1991). doi: 10.1126/science.1957170; pmid: 1957170
34. J. A. Steyer, W. Almers, A real-time view of life within 100 nm of the plasma membrane. *Nat. Rev. Mol. Cell Biol.* **2**, 268–275 (2001). doi: 10.1038/35067069; pmid: 11283724
35. T. J. Deerinck, E. A. Bushong, A. Thor, M. H. Ellisman, NCMIR methods for 3D EM: A new protocol for preparation of biological specimens for serial block face scanning electron microscopy (National Center for Microscopy and Imaging Research, 2010). www.ncmir.ucsd.edu/sbem-protocol.
36. P. Kner, B. B. Chhun, E. R. Griffis, L. Winoto, M. G. L. Gustafsson, Super-resolution video microscopy of live cells by structured illumination. *Nat. Methods* **6**, 339–342 (2009). doi: 10.1038/nmeth.1324; pmid: 19404253
37. C. Sommer, C. Straehle, U. Kothe, F. A. Hamprecht, Ilastik: Interactive learning and segmentation toolkit. In *2011 8th IEEE International Symposium on Biomedical Imaging (ISBI 2011)*, pp. 230–233 (2011). doi: 10.1109/ISBI.2011.5872394
38. D. Loerke *et al.*, Cargo and dynamin regulate clathrin-coated pit maturation. *PLoS Biol.* **7**, e1000057 (2009). doi: 10.1371/journal.pbio.1000057; pmid: 19296720
39. A. V. Weigel, M. M. Tamkun, D. Krapp, Quantifying the dynamic interactions between a clathrin-coated pit and cargo molecules. *Proc. Natl. Acad. Sci. U.S.A.* **110**, E4591–E4600 (2013). doi: 10.1073/pnas.1315202110; pmid: 24218552

## ACKNOWLEDGMENTS

Supported by a NIGMS Postdoctoral Research Associate Program fellowship (A.V.W.), an Intramural AIDS research fellowship from the NIH Office of AIDS Research (C.J.O.), a grant from the NIH Intramural AIDS Targeted Antiviral Program (J.L.-S. and C.J.O.), National Key Research Program of China grant 2016YFA0500200 (D.L.), and HHMI and the Intramural Research Programs of NINDS and NICHD. J.N.-A. is supported by a UCL School of Pharmacy PhD studentship (to K.H.). We thank H. White for assistance with cell culture, L. Shao for assistance with imaging and data processing, P.-P. Zhu for advice on immunocytochemistry, R. Yan for a generous gift of an RTN4A/B antibody, and E. Snapp for provision of an MDCK ER-RFP stable cell line and critical reading of the manuscript. The authors declare that there are no conflicts of interest. All data to support the conclusions are provided either in the manuscript or in the supplementary materials.

## SUPPLEMENTARY MATERIALS

www.sciencemag.org/content/354/6311/aaf3928/suppl/DC1  
Supplementary Text  
Figs. S1 to S8  
Tables S1 to S6  
Movies S1 to S5  
References (40–48)

3 February 2016; accepted 16 September 2016  
10.1126/science.aaf3928

## RESEARCH ARTICLE

## HOST RESPONSE

# Inflammation-induced disruption of SCS macrophages impairs B cell responses to secondary infection

Mauro Gaya,<sup>1\*</sup> Angelo Castello,<sup>1\*</sup> Beatriz Montaner,<sup>1</sup> Neil Rogers,<sup>2</sup> Caetano Reis e Sousa,<sup>2</sup> Andreas Bruckbauer,<sup>1</sup> Facundo D. Batista<sup>1†</sup>

The layer of macrophages at the subcapsular sinus (SCS) captures pathogens entering the lymph node, preventing their global dissemination and triggering an immune response. However, how infection affects SCS macrophages remains largely unexplored. Here we show that infection and inflammation disrupt the organization of SCS macrophages in a manner that involves the migration of mature dendritic cells to the lymph node. This disrupted organization reduces the capacity of SCS macrophages to retain and present antigen in a subsequent secondary infection, resulting in diminished B cell responses. Thus, the SCS macrophage layer may act as a sensor or valve during infection to temporarily shut down the lymph node to further antigenic challenge. This shutdown may increase an organism's susceptibility to secondary infections.

The highly organized architecture of the lymph node (LN) is critical for mounting effective immune responses against pathogens. One particular facet of this organization is the layer of CD169<sup>+</sup> macrophages at the subcapsular sinus (SCS) floor; strategically positioned at the lymph-tissue interface to capture pathogens as they enter the LN (1). This prevents systemic dissemination of pathogens (2–5) and allows presentation of intact antigen in the form of immune complexes, viruses, and bacteria to cognate B cells for the initiation of humoral immune responses (2, 6–8).

Infection causes a remodeling of the global architecture of the LN (9, 10). However, how this process affects the organization of the SCS macrophage layer is not well defined. To address this, we visualized the distribution of SCS macrophages in draining LNs of C57BL/6 mice after ear skin infection with *Staphylococcus aureus*, the most common etiological organism of skin and soft tissue infection. Cryosections of superficial cervical LNs were immunostained and examined 7 days after infection by confocal microscopy. The overall dimensions of the LNs were increased around fourfold with considerable enlargement of the B220<sup>+</sup> follicular regions and a marked disruption of the CD169<sup>+</sup> population at the SCS and interfollicular regions (Fig. 1A). We observed a similar disruption in the SCS macrophage organization after localized infection with

influenza A virus, *Vaccinia* virus (VACV), and group B *Streptococcus* (GBS) but not after administration of ultraviolet (UV)-inactivated virus or inert beads (fig. S1, A to C). Notably, mice receiving either the Toll-like receptor 9 (TLR9) agonist CpG or the TLR4 agonist lipopolysaccharide (LPS) in the footpad display similar changes in the LN organization (Fig. 1B and figs. S1D and S2). This is a temporary process as the compact layer of SCS macrophages is reestablished after 28 days (fig. S1E). Overall, these data show that disruption of SCS macrophages in draining LNs is a frequent feature associated with inflammation and viral or bacterial infections.

We further investigated this loss of integrity in the SCS macrophage layer following inflammation by using two high-resolution technologies. Three-dimensional (3D) multiphoton imaging of whole explanted LNs showed a decrease in the number and density of CD169<sup>+</sup> macrophages accompanied with a change in morphology and retraction of these cells from the SCS (Fig. 1C and movie S1). Three-dimensional electron tomography, scanning 100-nm LN sections over a distance of 100  $\mu$ m, revealed that macrophages are located toward the follicular interior during inflammation, whereas they are positioned longitudinally on the inner wall of the SCS on steady state (Fig. 1D and movie S2). Together, this shows that the characteristic disruption of SCS macrophages is a result of both cell loss and displacement of cells toward inner follicular areas.

To analyze the mechanism by which inflammation triggers alterations in SCS macrophage organization, we used the CpG-mediated inflammation model and a series of mouse strains in which different components

of the TLR signaling pathway have been genetically ablated. Mice deficient in TLR9, MyD88-TRIF adaptors, or MyD88 alone did not exhibit SCS macrophage disruption, concordant with the notion that responses to CpG are mediated by TLR9 signaling via MyD88 (Fig. 2A and fig. S3). To determine which MyD88-expressing immune cell population is required for this process, we deleted MyD88 in B cells (*Myd88<sup>fllox/fllox</sup> Cd19 Cre<sup>+</sup>* mice), dendritic cells (DCs) (*Myd88<sup>fllox/fllox</sup> Cd11c Cre<sup>+</sup>* mice), and neutrophils (*Myd88<sup>fllox/fllox</sup> Lyz2 Cre<sup>+</sup>* mice) (fig. S4). As revealed by flow cytometry, MyD88 abundance in SCS macrophages remains unchanged in the different transgenic models (fig. S4). B cells are not required for SCS macrophage disruption, as this process was observed in *Myd88<sup>fllox/fllox</sup> Cd19 Cre<sup>+</sup>* and Rag2-deficient mice (Fig. 2A and fig. S5A). Furthermore, the disruption was not prevented by lack of expression of MyD88 in neutrophils or their *in vivo* depletion with an antibody against Ly6G (anti-Ly6G) (Fig. 2A and fig. S5, B and C). In contrast, whereas draining LNs were enlarged in *Myd88<sup>fllox/fllox</sup> Cd11c Cre<sup>+</sup>* mice following inflammation, disruption of the SCS macrophage layer was significantly reduced (Fig. 2A and fig. S3B). These observations demonstrate that SCS macrophage disruption during inflammation is not simply due to associated enlargement of draining LNs but requires the expression of MyD88 in the DC population.

In line with these observations, we found a significant accumulation of DCs in the SCS following inflammation (Fig. 2, B and C, and fig. S6, A and B). Therefore, to determine if DC arrival is necessary for the disruption of the SCS macrophage layer, we injected phosphate-buffered saline (PBS) or CpG into either wild-type mice or mice lacking CCR7, the main LN-homing chemokine receptor for DCs (fig. S6, C and D) (11). Indeed, disruption of the macrophage layer was significantly reduced in CCR7-deficient animals (Fig. 2D). To evaluate whether DC arrival to the LN is sufficient for this disruption, we adoptively transferred into the footpad bone marrow-derived DCs (BM-DCs) that were previously treated with CpG *in vitro*. We observed disruption of the SCS macrophage layer in draining LNs of animals receiving CpG-treated BM-DCs but not control DCs; neither PBS-treated nor TLR9-deficient DCs (Fig. 2E and fig. S6E). Noticeably, a marked disruption was also observed when BM-DC migration was induced independently of TLR signaling with prostaglandin E2 (12), suggesting that DC migration per se can alter SCS macrophage organization (fig. S6F). Our observations suggest that the arrival of mature DCs during inflammation plays an important role in the disruption of SCS macrophages.

We next examined the functional implications of the impaired integrity of SCS macrophages for the retention and presentation of antigen arriving in a subsequent wave. We treated mice with PBS (control), CpG, VACV, or GBS and then challenged them with fluorescent microspheres (0.2  $\mu$ m) or fluores-

<sup>1</sup>Lymphocyte Interaction Laboratory, London Research Institute, Cancer Research UK, 44 Lincoln's Inn Fields, London WC2A 3LY, UK. <sup>2</sup>Immunobiology Laboratory, London Research Institute, Cancer Research UK, 44 Lincoln's Inn Fields, London WC2A 3LY, UK.

\*These authors contributed equally to this work. †Corresponding author. E-mail: facundo.batista@cancer.org.uk



to five HEL-coated microspheres, whereas in CpG-treated mice, only 3% of B cells acquire HEL-coated microspheres and never more than one per cell (Fig. 3C and fig. S7, H and I). Thus, concordant with the reduction in antigen retention by SCS macrophages, the acquisition of cognate antigen by B cells is reduced in draining LNs following inflammation.

Does the observed reduction in antigen acquisition during inflammation affect the capacity of B cells to respond to subsequent antigen challenge in vivo? To address this, wild-type mice were adoptively transferred with *Tlr9*<sup>-/-</sup> MD4 B cells and OT-II T cells (ovalbumin-specific T cell receptor). Afterwards, they were treated with PBS or CpG followed by administration of HEL-ovalbumin-coated microspheres. LNs from control mice contained ≈10<sup>3</sup> HEL-specific antibody-secreting cells (ASCs), although this was significantly lower in LNs from CpG-treated mice (Fig. 3D). We observed a similar reduction in HEL-specific ASC formation when mice were adoptively transferred with *Tlr9*<sup>-/-</sup> MD4 B cells followed by injection of CpG and HEL-αGalCer-coated microspheres (13) (Fig. 3E). These approaches demonstrate that inflammatory signals affect the extent to which B cells can acquire and respond to further antigenic challenge in vivo.

We then examined the potential impact that inflammation-mediated disruption of the SCS layer has on B cell responses to a subsequent viral infection. Wild-type mice were treated with PBS (control) or CpG and then infected with VACV. Control LNs exhibited an expansion of GL7<sup>+</sup>Fas<sup>+</sup>Bcl6<sup>+</sup> germinal center (GC) B cells and CD138<sup>+</sup>IgD<sup>lo</sup> virus-specific plasma cells (PCs) (Fig. 4, A to D). Instead, both GC

and PC formation were impaired when infection was initiated after inflammation induction (Fig. 4, A to D). B cell responses to VACV were restored to control levels when infection occurred 4 weeks after CpG administration

(fig. S8), a time frame consistent with the recovery of the structural integrity of the SCS macrophage layer (fig. S1E). Similar reductions in B cell responses were observed when *Diphtheria* toxin or clodronate liposomes were used

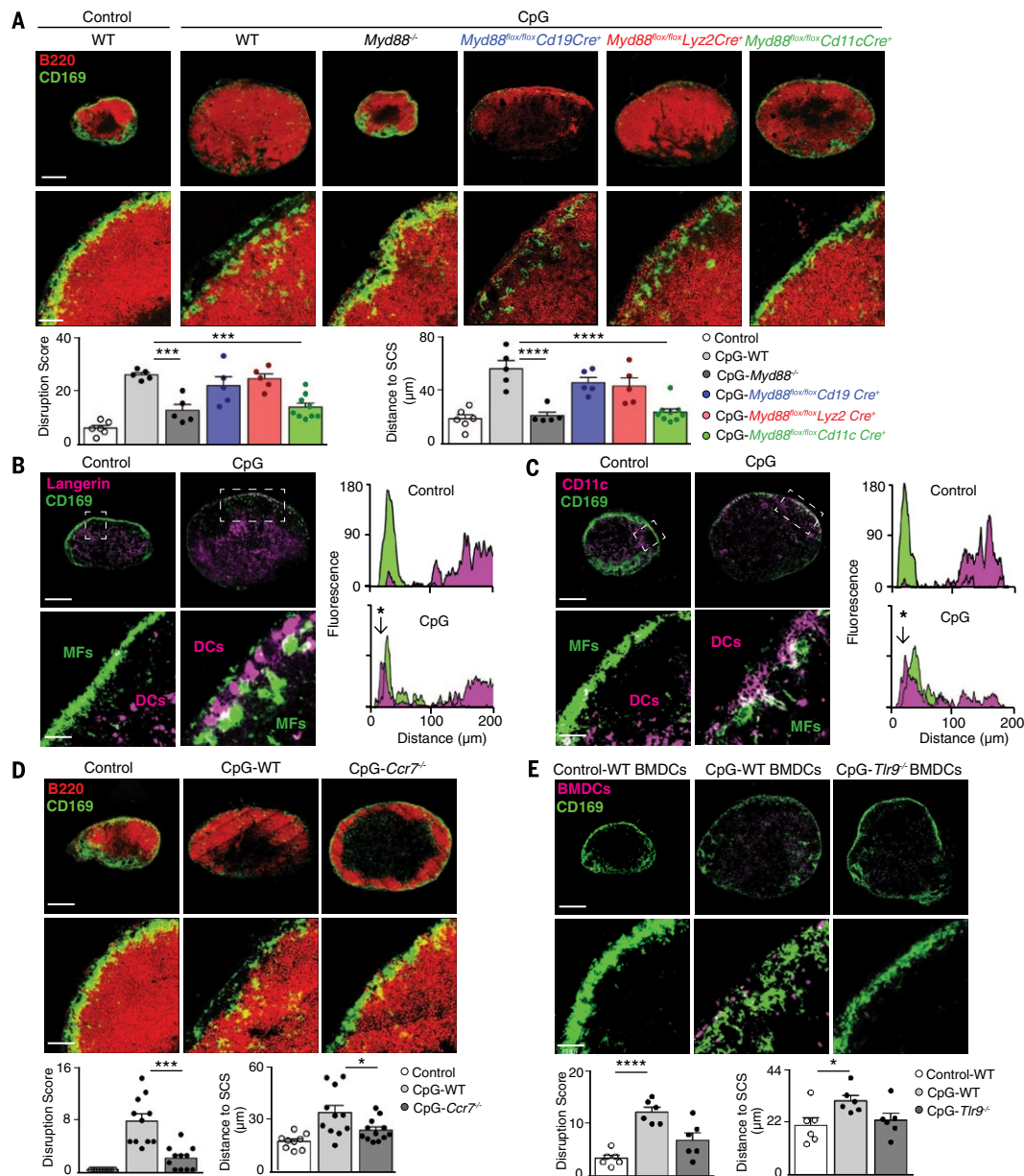


**Fig. 2. DC arrival at draining LN during inflammation is necessary for SCS macrophage disruption.** (A) Confocal microscopy images of popliteal LNs from WT, *Myd88*<sup>-/-</sup>, *Myd88*<sup>lox/lox</sup> *Cd19* *Cre*<sup>+</sup>, *Myd88*<sup>lox/lox</sup> *Lyz2* *Cre*<sup>+</sup>, and *Myd88*<sup>lox/lox</sup> *Cd11c* *Cre*<sup>+</sup> mice collected 4 days after footpad administration of PBS or CpG. Cryosections were stained with anti-mouse monoclonal antibodies (mAbs) to CD169 (green) and B220 (red). Scale bars, 300 μm (top); 60 μm (bottom). Bar charts represent quantification of SCS macrophage disruption and distance of macrophages to LN border in each condition for an individual experiment. Each dot represents a distinct follicle. Data are shown as mean ± SEM and are representative of three independent experiments. (B and C) Confocal microscopy images of popliteal LN sections stained with mAbs to CD169 (green) and (B) Langerin (magenta) or (C) CD11c (magenta) derived from mice that were injected with PBS or CpG 4 days previously. Scale bars,

300 μm (top); 60 μm (bottom). Histograms represent CD169, Langerin, and CD11c fluorescence measured from the outer edge of the LN to the inner areas. Stars indicate DCs at the SCS. (D) Confocal images of popliteal LNs cryosections stained as in (A) from WT and *Ccr7*<sup>-/-</sup> mice 4 days after footpad administration of PBS or CpG. Scale bars, 300 μm (top); 60 μm (bottom). Quantifications were performed as in (A). Data are representative of three independent experiments. (E) Confocal images of popliteal LN cryosections 4 days after footpad injection with 3 × 10<sup>6</sup> carboxyfluorescein diacetate succinimidyl ester (CFSE)-labeled (magenta) control BMDCs, CpG-treated WT BMDCs, or CpG-treated *Tlr9*<sup>-/-</sup> BMDCs. Sections were stained with mAb to CD169 (green). Scale bars, 300 μm (top); 60 μm (bottom). Quantifications were performed as in (A). Data are representative of three independent experiments. Student *t* test, \**P* < 0.05, \*\*\**P* < 0.001, \*\*\*\**P* < 0.0001.

to deplete SCS macrophages (14, 15) before VACV infection (fig. S9) or when mice received CpG or clodronate in the ear before infection with *S. aureus* (fig. S10). Therefore, it appears that the SCS macrophage disruption triggered by inflammation affects the ability of B cells to mount responses to viral or bacterial antigen arriving in a secondary wave.

Finally, we asked whether SCS macrophage disruption during a primary infection impedes the ability of B cells to respond to a secondary pathogen. After PBS (control) or GBS administration, mice were infected with VACV. The formation of VACV-specific PCs was significantly reduced in GBS-infected mice (Fig. 4E). This is consistent with the notion that loss of integrity of the SCS macrophage layer during primary infections severely affects the capacity of B cells to respond to secondary pathogens.

SCS macrophages have been placed at the heart of antipathogen responses because of their key role in antigen trapping and im-

mune response initiation (1–8, 16–20). We found that infection or inflammation leads to a significant loss of CD169<sup>+</sup> macrophages at the SCS and to a displacement of these cells toward inner follicular areas. Regardless of whether this is due to cell death (5) and/or macrophage redistribution, these observations raise the important question of the potential benefit of such a phenomenon. We speculate that this marked architectural reorganization might be beneficial in allowing the entry of afferent lymph-derived immune cells directly through the SCS floor (21); it may facilitate antigen relay to follicular DCs (7) or it might maximize presentation of antigen to B cells.

However, although these scenarios would be likely to enhance immune responses in a primary infection, the disruption of SCS macrophages would also render draining LNs temporarily refractory to newly arriving pathogens. This inability to respond to subsequent pathogens parallels recent findings that the

failure of host defenses to counteract secondary infections results from loss of lymphoid tissue integrity or compromised innate host defense (22, 23). Here, we propose a model in which SCS macrophages function as a valve that senses inflammation within draining LNs, triggering the temporary shutdown of humoral responses to secondary infections to prioritize the effective control of contemporaneous lymph-borne infecting pathogens (fig. S11).

## REFERENCES AND NOTES

1. F. D. Batista, N. E. Harwood, *Nat. Rev. Immunol.* **9**, 15–27 (2009).
2. T. Junt et al., *Nature* **450**, 110–114 (2007).
3. M. Iannacone et al., *Nature* **465**, 1079–1083 (2010).
4. S. F. Gonzalez et al., *Nat. Immunol.* **11**, 427–434 (2010).
5. W. Kastenmüller, P. Torabi-Parizi, N. Subramanian, T. Lämmermann, R. N. Germain, *Cell* **150**, 1235–1248 (2012).
6. Y. R. Carrasco, F. D. Batista, *Immunity* **27**, 160–171 (2007).

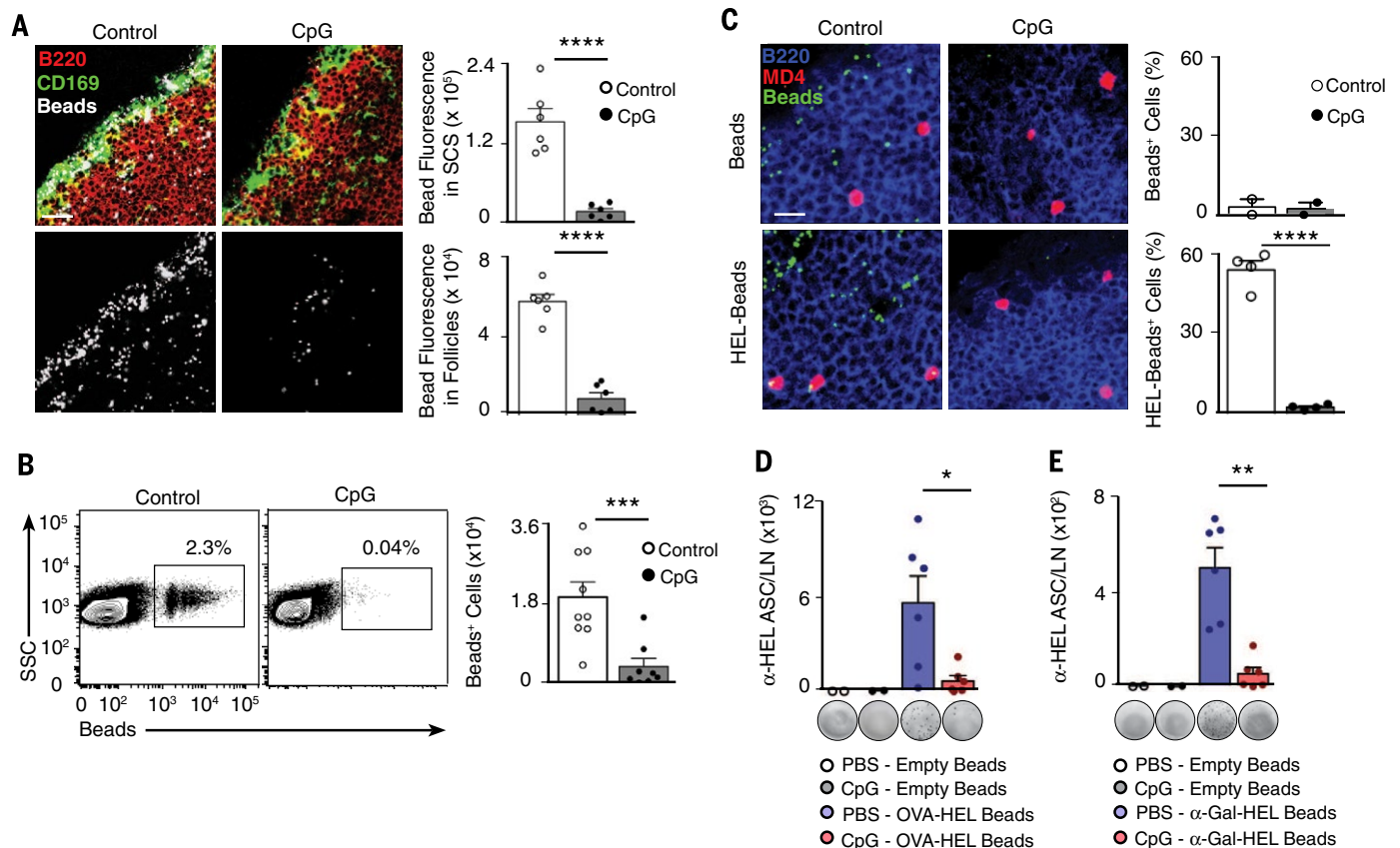


**Fig. 3. Inflammation impedes acquisition of subsequent antigen by SCS macrophages and cognate B cells.** (A) Confocal microscopy images of popliteal LNs from mice injected in the footpad with PBS or CpG and 4 days later injected again with  $8 \times 10^8$  fluorescent microspheres ( $0.2 \mu\text{m}$ , white). Sections were labeled with antibodies to B220 (red) and CD169 (green). Scale bar,  $70 \mu\text{m}$ . Bar charts represent beads fluorescence quantification in SCS and follicles from three independent experiments. (B) Flow cytometry analysis of popliteal LNs from animals treated as in (A). Representative dot plots depict beads acquisition by B220<sup>+</sup> CD3<sup>+</sup> cells. Quantification of beads-positive cells from three independent experiments is shown in the bar chart. (C) Confocal microscopy images of LNs from mice that were (i) adoptively transferred with  $5 \times 10^6$  SNARF-labeled MD4<sup>+</sup> *Tlr9*<sup>-/-</sup> B cells (red) on day 0, (ii) administered PBS or CpG in the footpad on day 1, (iii) injected again with  $8 \times 10^8$  avidin fluorescent

particles (green) coated or not with HEL on day 5, and (iv) killed after 6 hours. Sections were stained with B220 antibody (blue). Scale bar,  $20 \mu\text{m}$ . Bar charts represent the proportion of MD4<sup>+</sup> B cells loaded with particles for an individual experiment. Data are representative of three independent experiments. (D and E) ELISPOT analysis of HEL-specific ASCs (day 14) in popliteal LNs of animals that were (i) adoptively transferred with (D)  $5 \times 10^5$  MD4 *Tlr9*<sup>-/-</sup> B cells and  $5 \times 10^6$  OT-II T cells or (E)  $2 \times 10^6$  MD4 *Tlr9*<sup>-/-</sup> B cells, (ii) injected with PBS or CpG in the footpad on day 1, and (iii) injected again with (D) OVA-HEL beads or (E)  $\alpha$ GalCer-HEL beads on day 7. Bar charts represent the number of HEL-specific ASCs in each condition for an individual experiment. Data are representative of three independent experiments. In all panels, each dot in bar charts represents a single mouse. Data are shown as mean  $\pm$  SEM. Student's *t* test, \* $P < 0.05$ , \*\* $P < 0.01$ , \*\*\* $P < 0.001$ , \*\*\*\* $P < 0.0001$ .

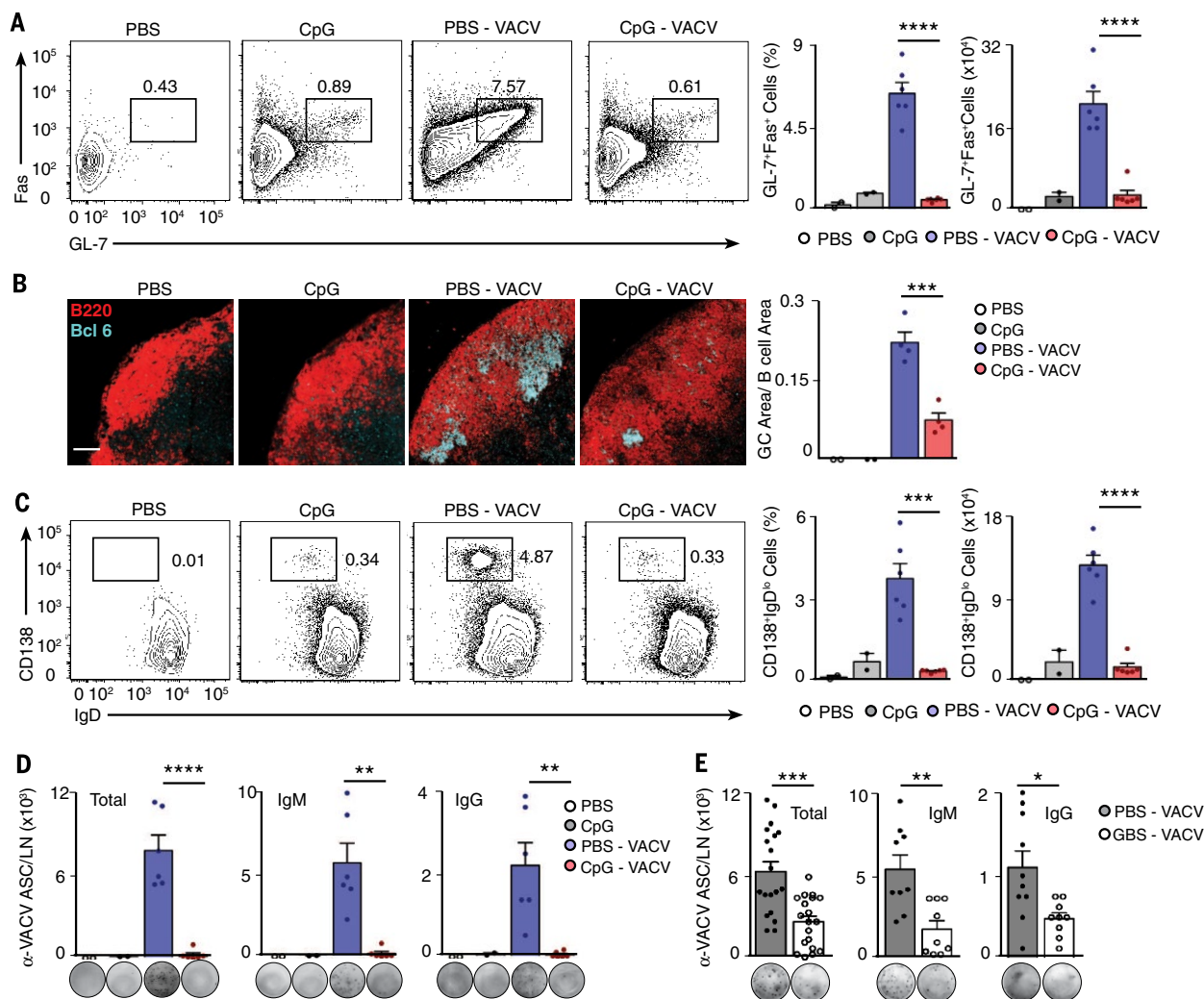


**Fig. 4. Inflammation and primary infection shut down B cell responses to subsequent pathogens.** (A) Flow cytometry analysis of GC formation (day 14) in popliteal LNs from mice that were administered PBS or CpG in the footpad and 7 days later infected with  $10^4$  plaque-forming units (PFU) of VACV. Representative contour plots display the percentage of B220<sup>+</sup> cells that are GL-7<sup>+</sup>Fas<sup>+</sup>. Bar charts display the quantification of GL-7<sup>+</sup>Fas<sup>+</sup> B cells in the different conditions for a single experiment. (B) Confocal microscopy analysis of popliteal LNs from mice treated as in (A). Sections were stained with mAbs to B220 (red) and Bcl-6 (cyan). Scale bar, 60  $\mu$ m. Quantification of the GC area for an individual experiment is depicted on the right bar chart. (C) Flow cytometry analysis of PC formation in mice treated as in (A). Representative contour plots show the

percentage of B220<sup>+</sup> cells that are also CD138<sup>+</sup>IgD<sup>low</sup>. The quantification of CD138<sup>+</sup>IgD<sup>low</sup> B cells for a single experiment is shown on the right bar charts. (D) ELISPOT analysis of total, immunoglobulin M (IgM) and IgG VACV-specific ASCs in popliteal LNs from mice that were treated as in (A). Bar charts represent the number of VACV-specific ASCs for an individual experiment. (E) ELISPOT analysis of total, IgM, and IgG VACV-specific ASCs (day 14) from mice that were administered PBS or  $10^6$  CFU of GBS in the footpad and then infected with  $10^4$  PFU of VACV on day 7. Bar charts represent the number of VACV-specific ASCs from three independent experiments. In all panels, experiments were performed at least three times and each dot represents a different mouse. Data are shown as mean  $\pm$  SEM. Student's *t* test, \**P* < 0.05, \*\**P* < 0.01, \*\*\**P* < 0.001, and \*\*\*\**P* < 0.0001.

7. T. G. Phan, I. Grigorova, T. Okada, J. G. Cyster, *Nat. Immunol.* **8**, 992–1000 (2007).
8. T. G. Phan, J. A. Green, E. E. Gray, Y. Xu, J. G. Cyster, *Nat. Immunol.* **10**, 786–793 (2009).
9. T. Junt, E. Scandella, B. Ludewig, *Nat. Rev. Immunol.* **8**, 764–775 (2008).
10. V. Kumar *et al.*, *Blood* **115**, 4725–4733 (2010).
11. G. J. Randolph, V. Angeli, M. A. Swartz, *Nat. Rev. Immunol.* **5**, 617–628 (2005).
12. J.-H. Yen, T. Khayrullina, D. Ganea, *Blood* **111**, 260–270 (2008).
13. P. Barral *et al.*, *Proc. Natl. Acad. Sci. U.S.A.* **105**, 8345–8350 (2008).
14. Y. Miyake *et al.*, *J. Clin. Invest.* **117**, 2268–2278 (2007).
15. F. G. Delemarre, N. Kors, G. Kraal, N. van Rooijen, *J. Leukoc. Biol.* **47**, 251–257 (1990).

16. P. Barral *et al.*, *Nat. Immunol.* **11**, 303–312 (2010).
17. T. Chtanova *et al.*, *Immunity* **31**, 342–355 (2009).
18. J. L. Coombes, S.-J. Han, N. van Rooijen, D. H. Raulet, E. A. Robey, *Cell Reports* **2**, 124–135 (2012).
19. Z. Garcia *et al.*, *Blood* **120**, 4744–4750 (2012).
20. T. Chtanova *et al.*, *Immunity* **29**, 487–496 (2008).
21. A. Braun *et al.*, *Nat. Immunol.* **12**, 879–887 (2011).
22. E. Scandella *et al.*, *Nat. Immunol.* **9**, 667–675 (2008).
23. A. M. Jamieson, S. Yu, C. H. Annicelli, R. Medzhitov, *Cell Host Microbe* **7**, 103–114 (2010).

**ACKNOWLEDGMENTS**

We thank A. Rot and D. Withers for the CCR7 knockout mouse strain. We thank L. Collinson, H. Armer, and C. Peddie from the electron microscopy facility for electron microscopy and 3View analysis of lymph nodes; the experimental histopathology facility for the initial preparation of tissue cryosections; and S.

Lutter for assistance with whole-body imaging. We thank N. Harwood and J. Coleman for editing of the manuscript, and P. Barral, J. Caamaño, R. Germain, and the members of the Lymphocyte Interaction Laboratory for critical reading of the manuscript. We thank F. Sallusto for feedback and suggestion of the term “shut down.” The data presented in this manuscript are tabulated in the main paper and in the supplementary materials. Supported by Cancer Research UK.

**SUPPLEMENTARY MATERIALS**

www.sciencemag.org/content/347/6222/667/suppl DC1  
Materials and Methods  
Figs. S1 to S11  
References (24–29)  
Movies S1 and S2

21 October 2014; accepted 11 December 2014  
10.1126/science.aaa1300

## ORIGIN OF NOTOCHORD

# Development of the annelid axochord: Insights into notochord evolution

Antonella Lauri,<sup>1\*†</sup> Thibaut Brunet,<sup>1\*</sup> Mette Handberg-Thorsager,<sup>1,2‡</sup>  
 Antje H.L. Fischer,<sup>1§</sup> Oleg Simakov,<sup>1</sup> Patrick R. H. Steinmetz,<sup>1||</sup> Raju Tomer,<sup>1,2¶</sup>  
 Philipp J. Keller,<sup>2</sup> Detlev Arendt<sup>1,3#</sup>

The origin of chordates has been debated for more than a century, with one key issue being the emergence of the notochord. In vertebrates, the notochord develops by convergence and extension of the chordamesoderm, a population of midline cells of unique molecular identity. We identify a population of mesodermal cells in a developing invertebrate, the marine annelid *Platynereis dumerilii*, that converges and extends toward the midline and expresses a notochord-specific combination of genes. These cells differentiate into a longitudinal muscle, the axochord, that is positioned between central nervous system and axial blood vessel and secretes a strong collagenous extracellular matrix. Ancestral state reconstruction suggests that contractile mesodermal midline cells existed in bilaterian ancestors. We propose that these cells, via vacuolization and stiffening, gave rise to the chordate notochord.

**D**efining the properties and characteristics of the last common ancestor of bilaterian animals, Urbilateria, is a key question of the evolution and development field (1). In an attempt to infer a possible urbilaterian precursor for the chordate notochord (2, 3), we reasoned that this structure should occupy a similar position with regard to overall morphology and molecular topography during development and in the adult body plan of living descendants (Fig. 1, A and B); that it should express, during its development, a suite of genes that have proven specific and indispensable for notochord formation in the chordates; and that it should be of widespread occurrence in bilaterian body plans (Fig. 1C). We focused our search on the model annelid *Platynereis dumerilii*, which is amenable to molecular studies and has retained more ancestral features than *Drosophila melanogaster* or *Caenorhabditis elegans* (4). By looking for cell populations that would resemble the vertebrate chordamesoderm (a population of mesodermal midline cells that converge medially to give rise to the notochord; red in Fig. 1A), we identified segmental pairs of mesodermal cells on the non-

bone morphogenetic protein (BMP) body side (5) that stood out by early and continuous expression of *col1A1*, encoding collagen type A (Fig. 2, A to D). SiMView light sheet microscopy (6) revealed that these cells moved underneath the neuroectoderm toward the midline until they contacted their bilateral counterpart (movie S1 and Fig. 2E). Subsequently, these cells narrowed and elongated without a net increase in cell surface (fig. S1), and additional adaxial mesodermal cells were observed to intercalate between the elongating pairs (Fig. 2E), reminiscent of the processes by which the chordamesoderm converges and extends (table S1) (7). Lineage tracking by targeted photoconversion of the fluorescent protein kikGR confirmed the origin of these cells from the mesodermal bands (fig. S2).

The unique location, large size, and specific arrangement of the *Platynereis* mesodermal midline cells allowed their unambiguous identification after whole-mount in situ hybridization (WMISH) and thus expression profiling by confocal imaging. To test a possible homology of these cells with the chordamesoderm, we chose a chordamesoderm-specific gene set according to the following criteria: (i) specificity—their combined expression uniquely defines the chordamesoderm; (ii) conservation—their chordamesoderm expression is conserved in at least three of four vertebrate species; and (iii) function—they have proven essential for chordamesoderm development or signaling. We thus investigated expression of seven transcription factors (*brachyury*, *foxA*, *foxD*, *twist*, *not*, *soxD*, and *soxE*), the signaling molecules *noggin* and *hedgehog* [*chordin* appears absent from annelid genomes (8)], and the guidance factors *netrin* and *slit* (table S2 for references). Transcripts for all but one [the *not* gene (2)] were detected (figs. S3 to S5) in accordance with previously reported *brachyury* expression (9), and their coexpression confirmed

by double WMISH (Fig. 2, F to L). Although none of the genes were exclusively expressed in the annelid mesodermal midline, their combined coexpression was unique to these cells (implying that mesodermal midline in annelids and chordamesoderm in vertebrates are more similar to each other than to any other tissue). It is unlikely that the molecular similarity between annelid and vertebrate mesodermal midline is due to independent co-option of a conserved gene cassette, because this would require either that this cassette was active elsewhere in the body (which is not the case) or that multiple identical independent events of co-option occurred (which is unparsimonious). As in vertebrates, the mesodermal midline resembles the neuroectodermal midline, which expresses *foxD*, *foxA*, *netrin*, *slit*, and *noggin* (figs. S6 and S7) but not *brachyury* or *twist*. However, unlike in chicken (10), the annelid mesodermal and ectodermal midline populations are not directly related by lineage (fig. S2). Last, the *Platynereis* mesodermal midline is devoid of *paraxis*, which is exclusively expressed in laterally adjacent mesoderm (fig. S8), in line with its vertebrate ortholog demarcating paraxial mesoderm (11). In vertebrates, this segregation depends on canonical Wnt signaling, with  $\beta$ -catenin-positive cells preferentially adopting a paraxial fate and position (12). Consistently, we observed nuclear localization of  $\beta$ -catenin in the more-lateral mesoderm only, and  $\beta$ -catenin overactivation converted the mesodermal midline toward a more lateral fate and position (fig. S8).

We next compared the developmental fate of annelid and vertebrate mesodermal midline cells. Phalloidin staining and expression analysis of muscle markers (fig. S9) revealed that, after elongation, the *Platynereis* mesodermal midline cells differentiate into the previously described “medial ventral longitudinal muscle” (13) (Fig. 3A). Given the ropelike appearance and axial position of this muscle, we propose to call it “axochord.” A muscular nature of a putative invertebrate counterpart of the chordate notochord is consistent with the observation that in the most basal chordate, amphioxus, the notochord is composed of specialized muscle cells (14) and expresses the same muscle markers (15). We further observed segmental sets of transverse muscles connecting to the axochord (“ventral oblique muscles”) (13) (Fig. 3, A and B, and fig. S3). Scanning electron microscopy revealed that, in adult worms, the axochord is deeply embedded in the fibrous sheath of the ventral nerve cord (16) and remains connected to the transverse muscles (Fig. 3, C and D). Immunostainings confirmed its axial position between neuropil and blood vessel (fig. S12; similar to the notochord; Fig. 1, A and B). Axochord contractility was evident from live imaging (fig. S9, E to G, and movie S2) and occurred in alternation with the transverse muscles (movie S3). Electron micrographs confirmed the muscular nature of axochordal cells and revealed a tight physical connection to transverse muscles (Fig. 3, E to I). Laser ablation of the axochord impaired crawling (fig. S10 and movie S4) and confirmed anchoring of the transverse musculature. Additionally, we found that the

<sup>1</sup>Developmental Biology Unit, European Molecular Biology Laboratory (EMBL), D-69117 Heidelberg. <sup>2</sup>Janelia Farm Research Campus, 19700 Helix Drive, Ashburn, VA 20147, USA. <sup>3</sup>Centre for Organismal Studies, University of Heidelberg, Heidelberg, Germany.

\*These authors contributed equally to this work. †Present address: Institute for Biological and Medical Imaging and Institute of Developmental Genetics, Helmholtz Zentrum München, Ingolstädter Landstrasse 1, D-85764 Neuherberg, Germany. ‡Present address: Max Planck Institute of Molecular Cell Biology and Genetics, Pfotenhauerstrasse 108, 01307 Dresden, Germany. §Present address: Department for Molecular and Cell Biology, Harvard University, 16 Divinity Ave, Cambridge, MA 02138, USA. ||Present address: Department for Molecular Evolution and Development, University of Vienna, Althanstrasse 14, A-1090 Wien, Austria. ¶Present address: Howard Hughes Medical Institute, Stanford University, Stanford, CA 94305, USA. #Corresponding author. E-mail: detlev.arendt@embl.de

*Platynereis* transverse muscles share a specific molecular profile (*en+foxA*; fig. S11) with the vertebrate pioneer myocytes flanking the notochord (17).

We next examined whether an axochord is also present in other annelids, lophotrochozoans, or protostomes (Fig. 1C). Phalloidin stainings had revealed ventral midline muscles in almost all annelid families (table S3), yet in some cases only pairs of ventral muscles had been reported (18, 19). One such example is *Capitella teleta*, which belongs to the second big clade of annelids, the Sedentaria (beside Errantia, to which *Platynereis*

belongs). We investigated development and molecular identity of ventral muscle fibers in *Capitella* (18) and found that (i), preceding metamorphosis, these converge and fuse into an axochord (Fig. 4, A to D, and fig. S13); (ii) the expression patterns of *foxA*, *noggin*, *brachyury*, *netrin* (Fig. 4, B and D, and fig. S13, B and C); *twist2* (20); and *hedgehog* (21) are consistent with coexpression in the axochord; and (iii) pairs of transverse muscles connect to the *Capitella* axochord (Fig. 4E) as in *Platynereis*. We also investigated the annelid *Owenia fusiformis* that belongs to the most basal annelid family

(22) and likewise found an axochord connected to transverse muscle fibers (Fig. 4F). A similar arrangement also occurs in mollusk (23) and brachiopod larvae (24), and ventral midline muscles are observed in most lophotrochozoan phyla (table S3), suggesting that an axochord is ancestral for lophotrochozoa. The lophotrochozoan axochord is a genuinely paired structure, composed of left and right adjacent muscle strands that often bifurcate anteriorly and/or posteriorly, as also observed in chaetognaths (Fig. 4, G and H), a possible protostome outgroup (25, 26) (Fig. 1C).

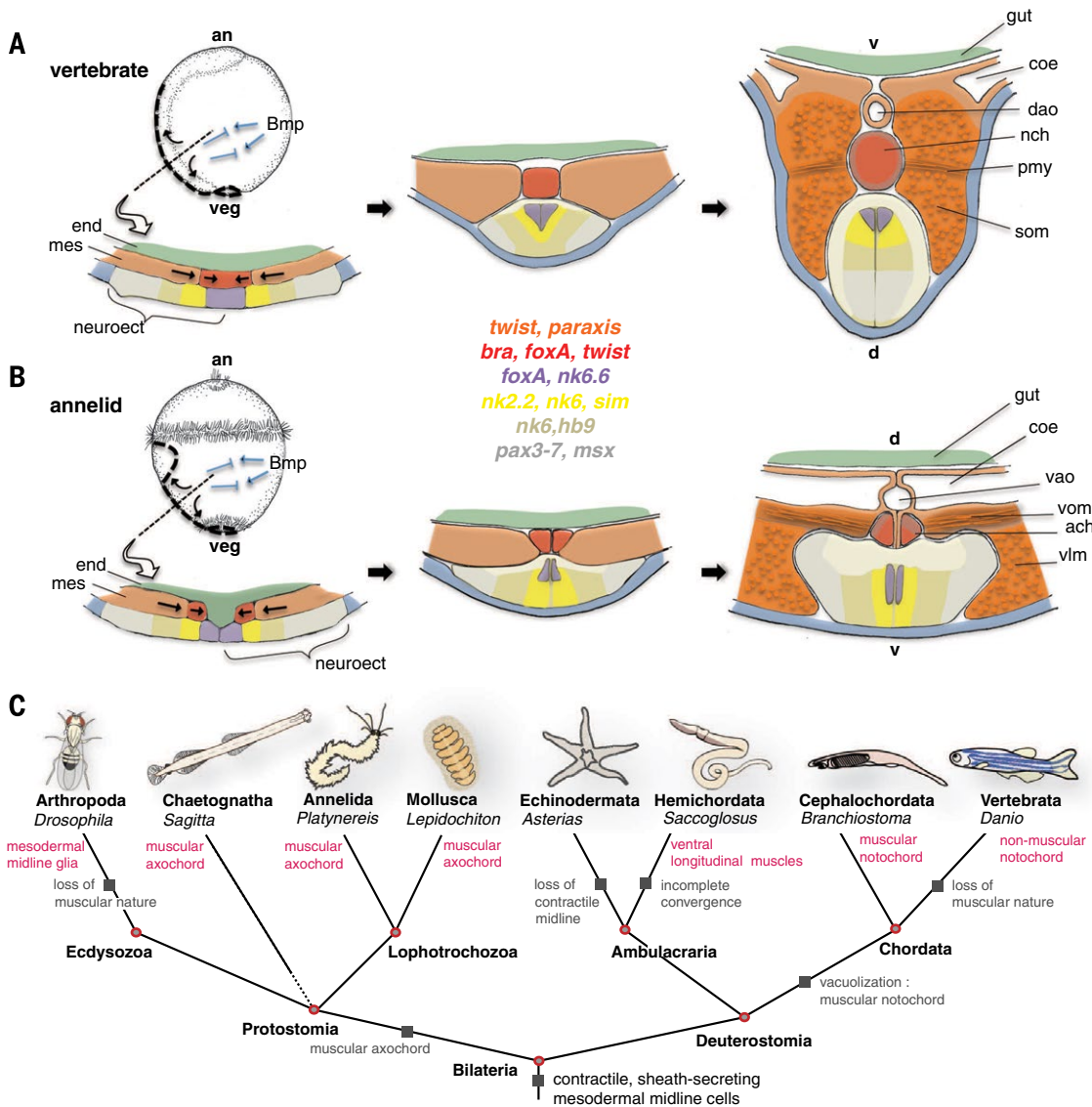


**Fig. 1. Comparison of notochord and axochord development, gene expression, and anatomy.** (A) Notochord development schematized for zebrafish at 9 hours post fertilization (hpf) or 90% epiboly, 14 hpf/neural keel, and 30 hpf/organogenesis stages. (B) Axochord development schematized for *Platynereis* at 34 hpf, 72 hpf, and 2 months of development. Top left images are in similar orientation with regard to the animal (an)–vegetal (veg) axis. Bold dashed lines represent lines of convergence of neuroectodermal and mesodermal cells, opposite to BMP signaling (blue arrows). The non-BMP body side will be dorsal (d) in vertebrate and ventral (v) in annelid, reflecting inversion of body posture in early chordate evolution (35). Thin black arrows indicate convergence and

extension. Thin black dashed lines indicate positions of transverse sections (bottom left). Red, notochord (nch) or axochord (ach); orange, mesoderm (mes); purple, neuroectodermal midline; yellow, medial interneuron column; faint yellow, motor neuron column; gray, sensory interneuron column; blue, epidermis; green, endoderm (end)/gut. Transcription factors defining the respective tissues are written in corresponding colors. Bold black arrows indicate developmental progression. neuroect, neuroectoderm; coe, coelom; dao, dorsal aorta; pmy, primary myocyte; som, somite; vao, ventral aorta; vom, ventral oblique muscle; vlm, ventral longitudinal muscle. (C) Simplified phylogenetic tree. Black boxes illustrate the proposed evolutionary transition from ventral midline contractile cells to notochord.

An ancestral state reconstruction based on our data and on a survey of bilaterian musculature (table S3) favored the presence of an axochord in protostome ancestors (fig. S14).

Regarding deuterostomes, previous studies on the origin of the notochord focused on the

hemichordate stomochord, an unpaired chordoid outpocketing of the pharynx, as a possible notochord homolog (27). Speaking against this hypothesis is its very anterior position and the absence of *brachyury*, *foxA*, and *noggin* expression (27, 28). *gooseoid*, *hedgehog*, and *colA*

expression rather suggest homology to the vertebrate prechordal plate (29–33). The pygochord, a stiff vacuolated rod in the posterior trunk of Ptychoderid hemichordates (34), lies dorsal to the ventral blood vessel in the ventral mesentery. This stands in contrast to both axochord and

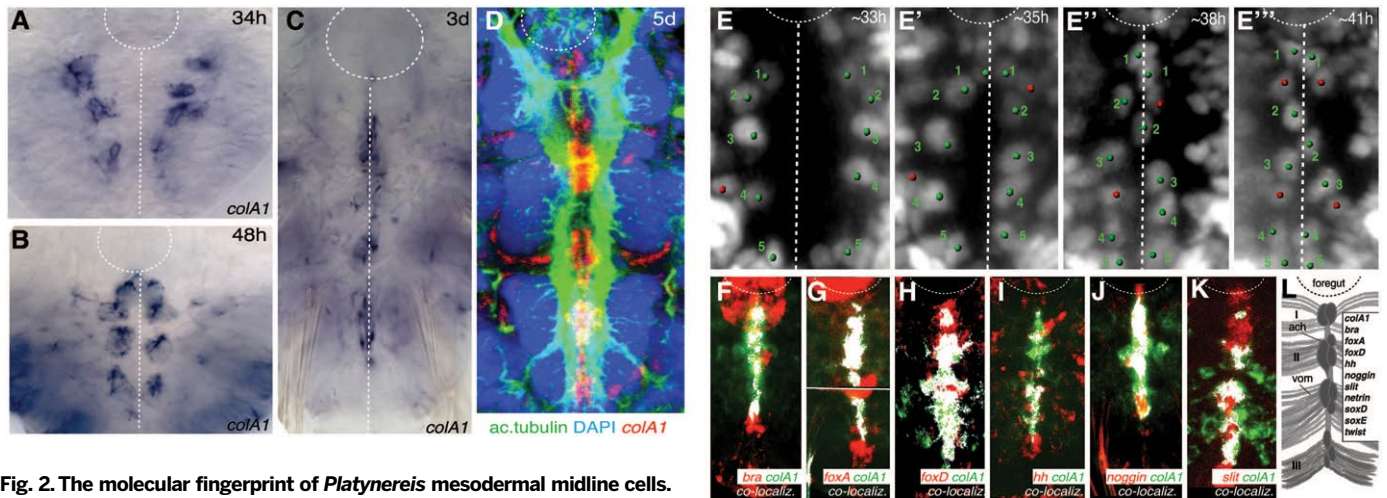
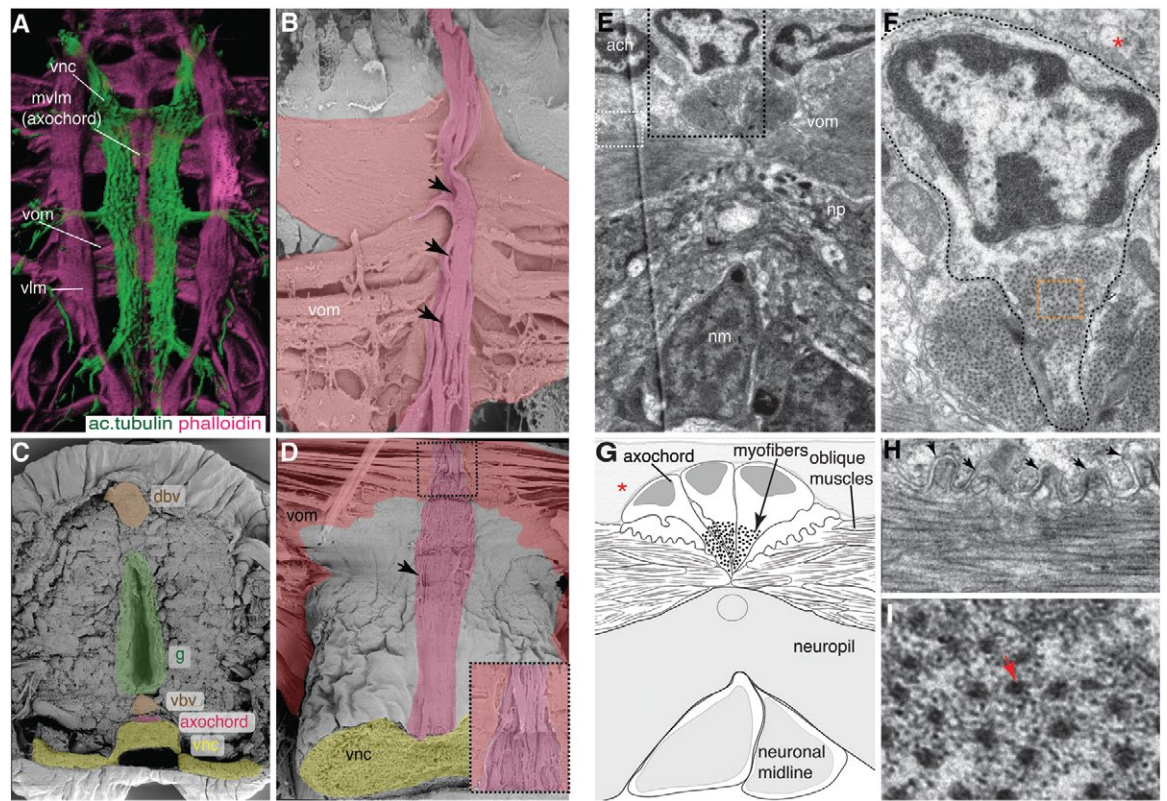


**Fig. 2. The molecular fingerprint of *Platynereis* mesodermal midline cells.**

(A to C) Bright-field images and (D) confocal z-projection of *colA1* WMISH. Dotted white circle and line indicate foregut and midline, respectively. DAPI, 4',6-diamidino-2-phenylindole. (E to E''') Snapshots of SiMView time lapse of a live larva with fluorescently labeled nuclei showing ventrally converging (green dots) and intercalating (red dots) axochordal cells. Time interval, 2 to 3 hours. (F to K) Confocal z-projections of double WMISH 3-dpf larvae, ventral views, anterior up. (L) Explanatory scheme. vom also weakly express *colA* and *foxD*. Foregut also expresses *bra* and *foxA*.

**Fig. 3. The axochord is a ventral medial longitudinal muscle.**

(A) Ventral view of *Platynereis* immunolabeled musculature and nervous system, z-projection of confocal stack. Vnc, ventral nerve cord; mvlm, median ventral longitudinal muscle (axochord). (B) Pseudocolored scanning electron micrograph of *Platynereis* juvenile trunk, dorsal view. Axochord (deep pink) and attached oblique muscles (light pink). (C and D) Pseudocolored scanning electron micrographs. (C) Adult cross section. g, gut; vbv/dbv, ventral/dorsal blood vessel. (D) Dissected specimen showing axochord and oblique muscles embedded in the vnc sheath. Closeup illustrates axochord cell morphology. (E) Transmission electron micrograph showing axochordal cells, ventral oblique muscles, neuronal midline (nm), and the neuropil (np). (F) Closeup of area in black square in (E). One axochordal cell is outlined with dashed black line; asterisk indicates extracellular matrix. (G) Schematic drawing of (E). (H) Closeup of area in white square in (E), showing interdigitations between axochordal cells and oblique muscles. (I) Closeup of (F) (orange square) showing cross-sectioned myofibers (red arrow).



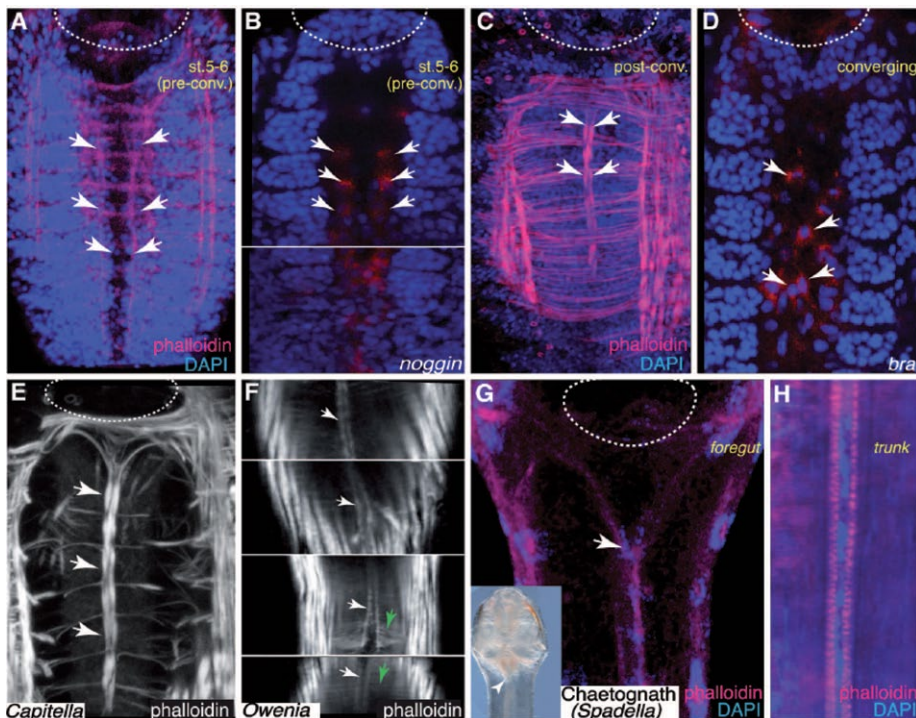


**Fig. 4. An axochord is widespread in protostomes.** (A to D) Convergence of ventral muscles into an axochord (white arrows) in *Capitella*, illustrated by phalloidin stainings (A and C) and WMISH (red in B and D) of selected axochord markers. (E) Axochord and transverse musculature in a stage-9 *Capitella* larva. Axochord bifurcation at the level of the foregut. (F) Axochord (white arrows) and transverse muscle fibers (green arrows) in juvenile *Owenia*, below the circumferential layer of longitudinal muscles. (G) Axochord (white arrow) in adult chaetognath (inset) bifurcating at the level of foregut. (H) Closeup of the axochord in the same specimen. Note elongated median nuclei and the two parallel strands of striated myofibers. All panels are z-projections of confocal stacks, ventral view, anterior up, white dashed line outlining foregut.

notochord, which are positioned between blood vessel and nerve cord (Fig. 1). Thus, vacuolization in the hemichordate stomochord and pygochord might have occurred independent to that of the chordate notochord. Unfortunately, no data are available for the specification and developmental fate of ventral mesodermal midline cells in hemichordates or larval echinoderms; except for *Protoglossus*, no ventromedian musculature has yet been observed (table S3).

Our study of annelid development reveals a population of mesodermal cells that converge and extend along the ventral midline and express a combination of transcription factors, signaling molecules, and guidance factors that closely matches that of the vertebrate chordamesoderm. These comparative data suggest that a similar population of mesodermal midline cells already existed in urbilaterian ancestors but leave open its ancient developmental fate. In annelids, these cells differentiate into an axochord; our investigation of chaetognath musculature and an ancestral state reconstruction based on comparative anatomy (fig. S14) suggest that a similar paired longitudinal muscle existed in protostome ancestors. Yet, in the absence of detailed investigations of expression profile and developmental fate of mesodermal midline cells in basal ecdysozoans and deuterostome ambulacrarians, the nature of ventral midline tis-

sue in urbilaterians remains undecided. It might have constituted sheath-secreting mesenchyme that was independently converted into muscular axochord and notochord in lophotrochozoans and chordates, respectively; alternatively, this tissue might have been contractile already and transformed into axochord in protostomes and notochord in chordates (Fig. 1C). Regardless of its nature, dorsoventral axis inversion (35) would have brought the ventral midline tissue into a dorsal position in the chordate lineage, and the appearance of incompressible vacuoles (14) would have gradually transformed it into a stiff rod of constant length; the amphioxus notochord could then be regarded a vestige of a contractile-cartilaginous transition. This transition could have involved the co-option of *not* expression (which is absent from the axochord, see above) given that zebrafish *not* null mutants form muscle tissue instead of notochord (36). Last, in vertebrates, the notochord was complemented by a rigid backbone that crucially contributed to the success of our phylum.

**REFERENCES AND NOTES**

1. E. M. De Robertis, Y. Sasai, *Nature* **380**, 37–40 (1996).
2. D. L. Stemple, *Development* **132**, 2503–2512 (2005).
3. N. Satoh, K. Tagawa, H. Takahashi, *Evol. Dev.* **14**, 56–75 (2012).
4. A. S. Denes et al., *Cell* **129**, 277–288 (2007).
5. D. Arendt, K. Nübler-Jung, *Mech. Dev.* **61**, 7–21 (1997).
6. R. Tomer, K. Khairy, F. Amat, P. J. Keller, *Nat. Methods* **9**, 755–763 (2012).

7. J. B. Wallingford, S. E. Fraser, R. M. Harland, *Dev. Cell* **2**, 695–706 (2002).
8. O. Simakov et al., *Nature* **493**, 526–531 (2013).
9. D. Arendt, U. Technau, J. Wittbrodt, *Nature* **409**, 81–85 (2001).
10. M. Catala, M. A. Teillet, E. M. De Robertis, M. L. Le Douarin, *Development* **122**, 2599–2610 (1996).
11. R. Burgess, P. Cserjesi, K. L. Ligon, E. N. Olson, *Dev. Biol.* **168**, 296–306 (1995).
12. W. E. Reintsch, A. Habring-Mueller, R. W. Wang, A. Schohl, F. Fagotto, *J. Cell Biol.* **170**, 675–686 (2005).
13. A. H. Fischer, T. Henrich, D. Arendt, *Front. Zool.* **7**, 31 (2010).
14. J. E. Webb, *J. Zool.* **170**, 325–338 (1973).
15. M. M. Suzuki, N. Satoh, *Dev. Biol.* **224**, 168–177 (2000).
16. D. G. Baskin, *Tissue Cell* **3**, 579–587 (1971).
17. P. D. Currie, P. W. Ingham, *Nature* **382**, 452–455 (1996).
18. S. D. Hill, B. C. Boyer, *Biol. Bull.* **201**, 257–258 (2001).
19. A. Filippova, G. Purschke, A. B. Tzvetlin, M. C. M. Müller, *Zoomorphology* **124**, 1–8 (2005).
20. K. K. Dill, K. Thamm, E. C. Seaver, *Dev. Genes Evol.* **217**, 435–447 (2007).
21. E. C. Seaver, L. M. Kaneshige, *Dev. Biol.* **289**, 179–194 (2006).
22. A. Weigert et al., *Mol. Biol. Evol.* **31**, 1391–1401 (2014).
23. M. Scherholz, E. Redl, T. Wollesen, C. Todt, A. Wanninger, *Curr. Biol.* **23**, 2130–2134 (2013).
24. A. Altenburger, A. Wanninger, *Front. Zool.* **6**, 3 (2009).
25. F. Marlétaz et al., *Curr. Biol.* **16**, R577–R578 (2006).
26. F. Marlétaz et al., *Genome Biol.* **9**, R94 (2008).
27. K. J. Peterson, R. A. Cameron, K. Tagawa, N. Satoh, E. H. Davidson, *Development* **126**, 85–95 (1999).
28. J. Gerhart, C. Lowe, M. Kirschner, *Curr. Opin. Genet. Dev.* **15**, 461–467 (2005).
29. J. Gerhart, *J. Cell. Physiol.* **209**, 677–685 (2006).
30. N. Miyamoto, H. Wada, *Nat. Commun.* **4**, 2713 (2013).
31. J. A. Belo, L. Leyns, G. Yamada, E. M. De Robertis, *Mech. Dev.* **72**, 15–25 (1998).
32. E. M. Pera, M. Kessel, *Development* **124**, 4153–4162 (1997).
33. A. W. L. Leung, S. Y. Y. Wong, D. Chan, P. P. L. Tam, K. S. E. Cheah, *Dev. Dyn.* **239**, 2319–2329 (2010).
34. K. Nübler-Jung, D. Arendt, *J. Zool. Syst. Evol. Res.* **37**, 93–100 (1999).
35. D. Arendt, K. Nübler-Jung, *Nature* **371**, 26 (1994).

**ACKNOWLEDGMENTS**

We thank A. Miyawaki for kikGR, R. Renkawitz-Pohl for the antibody against  $\beta$ -tubulin; P. McCrea for the antibody against  $\beta$ -catenin. A. Altenburger for brachiopod data; S. Kaul-Strehlow, G. Mayer, M. V. Sørensen, and K. Worsaae for insightful discussions; I. Hauber-Siller at the Electron Microscopy Core Facility (EMCF) (BioQuant, Heidelberg University); and the EMBL EMCF. The work was supported by the European Union's Seventh Framework Programme project "Evolution of gene regulatory networks in animal development (EVONET)" [215781-2] (A.L.), the Zoonet EU-Marie Curie early training network [005624] (A.F. and R.T.), the European Molecular Biology Laboratory (A.L., T.B., M.T.H., A.H.L.F., O.S., P.R.H.S., and R.T.), the EMBL International Ph.D. Programme (A.L., T.B., A.H.L.F., P.R.H.S., R.T.), the Boehringer Ingelheim Foundation (O.S.), the Howard Hughes Medical Institute (P.J.K.), and the Visiting Scientist Program at the Janelia Farm Research Campus (M.H.T., R.T., D.A., and P.J.K.). A.L. and T.B. designed, performed, and documented most of the experiments; developed protocols; and wrote the manuscript. R.T. initiated and, together with M.H.T. and P.J.K., developed the *Platynereis* SIMView live imaging assay, and M.H.T. acquired the SIMView data. A.H.L.F. investigated musculature development and gene expression in *Platynereis*. M.H.T. contributed to the expression analysis. O.S. did transmission electron microscopy with T.B. and A.L. P.R.H.S. cloned and characterized *twist*. R.T. developed the injection protocol with N. Kegel and B. Backfisch. D.A. coordinated the study, wrote the manuscript, and drew the summary figure. The plasmid encoding the kikGR construct is covered by a material transfer agreement provided by the RIKEN Brain Science Institute. Alignments used for tree building are deposited on Dryad (10.5061/dryad.1ct82).

**SUPPLEMENTARY MATERIALS**

www.sciencemag.org/content/345/6202/1365/suppl/DC1  
 Materials and Methods  
 Figs. S1 to S16  
 Tables S1 to S3  
 References (37–152)  
 Movies S1 to S4

14 March 2014; accepted 6 August 2014  
 10.1126/science.1253396

# Scanning Electron Microscopy in Life Sciences

## Technical Solutions for Biological Applications

Authors: Alexandra Elli, Ph.D.; Robert Kirmse, Ph.D.;  
Bernhard Zimmermann, Ph.D.  
Carl Zeiss Microscopy GmbH, Germany

Date: September 2017

**As a leading company in light, electron, X-ray, and helium ion microscopy, ZEISS continues to search for the best solution to make scientific life easier. ZEISS Scanning Electron Microscopes (SEM) address a wide variety of biological questions by unveiling sample ultrastructure in 2D and 3D. The microscopes image 3D volumes with pixel sizes down to a few nanometers, and provide a high degree of automation and imaging throughput.**

### Imaging with Highest Resolution at Low Voltages

Realized in the ZEISS Sigma and GeminiSEM families, field emission (FE) technology together with the proprietary Gemini column delivers the highest resolution and brilliant contrast performance. The Gemini column produces excellent contrast images at low voltages particularly suitable for biological samples, which are sensitive and nonconductive. Ultrathin sections, for example, can be easily imaged with our FE-SEMs to obtain TEM-like images at a resolution to resolve even lipid bilayers. A huge range of sample carriers can be mounted in an SEM, overcoming the size and number limitations of a TEM grid and TEM grid holders, thus supporting the use of a large variety of samples. Investigating resin-embedded samples,

which are typical for many biological applications, is readily amenable to SEM-based imaging. One possible approach involves cutting the sample into ultrathin sections. Either single or serial ultrathin sections can be imaged easily with different types of SEM detectors, such as the secondary electron (SE) detector, the backscattered electron (BSE) detector, or the STEM (scanning transmission electron microscopy) detector. The SE detector as well as the BSE detector provide images in excellent resolution and contrast even at extremely low voltages. Imaging sections on grids with a STEM detector deliver the highest resolution possible in a SEM, albeit with the limitation of TEM grids as sample carriers with the additional benefit of loading up to 12 grids into the SEM. However, the use of indium tin oxide (ITO)-coated cover glasses or silicon wafers as sample carriers enables the imaging of large numbers of serial sections with unprecedented speed for high throughput in a FE-SEM. Furthermore, the individual sections can be much larger and typically, one section alone is similar in or even exceeds the size of a TEM grid. TEM grids are enabling access to much larger sample areas than ever before.

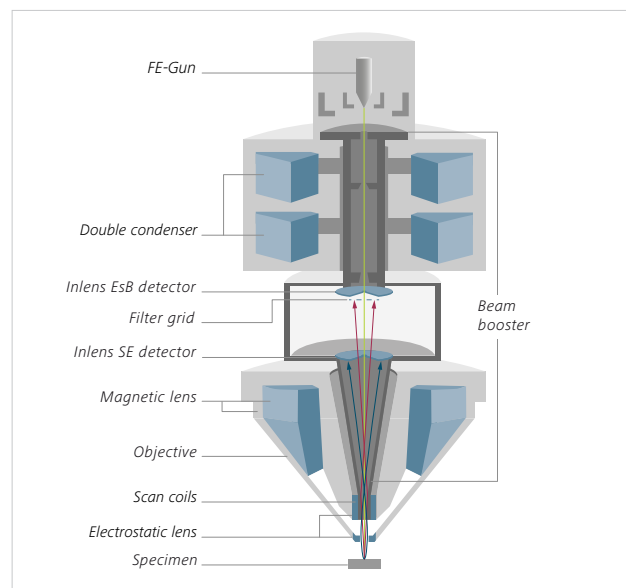
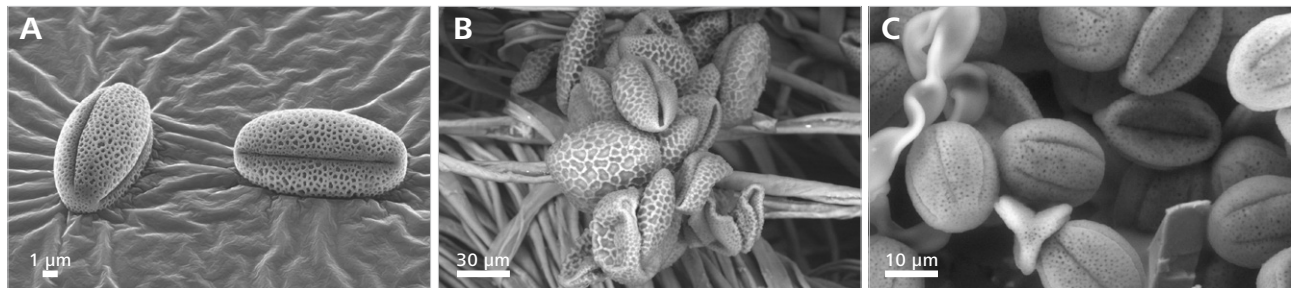


**Figure 1** FE-SEM GEMINI II detection system

### Topographical Imaging Under Environmental Conditions

Conventional scanning electron microscopes like the ZEISS EVO series enable the imaging of surface topography of samples such as insects and plants under environmental conditions. The biological specimens can be analyzed in their natural hydrated state, with extended pressures and water vapor revealing fine surface details without artifacts induced by a dehydration procedure.



SE detector, 10 kV, High Vacuum

BSE detector, 5 kV, 30 Pa air

EPSE, 15 kV, 1.5°C, 780 Pa Water Vapor

**Figure 2** Images of pollen taken under (A) high vacuum, under (B) air conditions and (C) environmental conditions, with water vapor. Utilizing environmental conditions reduces shrinking effects.

### 3D Imaging

Single images are snapshots of a complex 3D situation reduced to a 2D image. To fully understand the compartmentalization and the functionality beyond the ultrastructure of the sample, volume data is necessary. ZEISS supports a broad variety of techniques to enter the 3D world. One option is ZEISS Array Tomography (AT): Here, a resin-embedded sample is cut into ultrathin serial sections. The sequence of the sections defines the z-information of a subsequently computationally reconstructed 3D data set, and the thickness of the sections determines the z-resolution of this z-stack. The thickness of the sections is typically between 40–100 nm. To make your life much easier, a tape-collecting ultramicrotome (ATUMtome) can be used to produce and collect the sections automatically on a continuous tape. Likewise, data acquisition, i.e., the imaging of the resulting series of sections, is a highly automated process with ZEISS AT.

The 2D images are then computed into a 3D model. In addition, 3D SEM data sets can also be correlated with 3D light microscopic data sets of the same sample acquired with the ZEISS AT solution for fluorescence light microscopes. The serial sections can be stored and used for further imaging and labeling experiments.

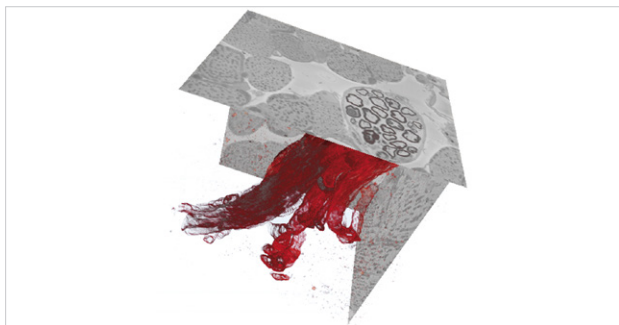


**Figure 3** 100 × 100 × 100 µm reconstructed mouse extraocular muscle. Reconstructed peripheral nerves are painted red and show the intricate detail of the nerve network, nodes, and bends. Courtesy of P. Munro, University College London, UK.

As an alternative to sequentially cutting a tissue block into serial sections and following image-acquisition imaging, resin-embedded cells or tissues may be imaged in 3D directly within the SEM chamber in a fully automated workflow: The surface of a specimen block is repetitively cut away with images of the exposed block surface taken after each sectioning event (block-face imaging). ZEISS offers two solutions to cut the sample within the scanning electron microscope: Either you use an ultramicrotome inside the SEM chamber (3View) or a focused ion beam (FIB)-SEM that combines a FE-SEM with a focused ion beam for milling. While 3View provides the fastest imaging of large 3D volumes with z-resolutions down to 15 nm, FIB-SEM is the best choice for higher z-resolutions down to 3–4 nm.

	FIB-SEM	3View	AT
<b>Sample Preparation</b>	Resin Block / Cryo	Resin Block	Ribbons on TEM grids, cover glasses or Wafers
<b>Sample</b>	Destroyed	Destroyed	Maintained
<b>z-Resolution</b>	3 nm	15 nm	40 nm
<b>EM Platform</b>	Crossbeam 340 / 540 / 550	Sigma / Merlin	Open FE-SEM

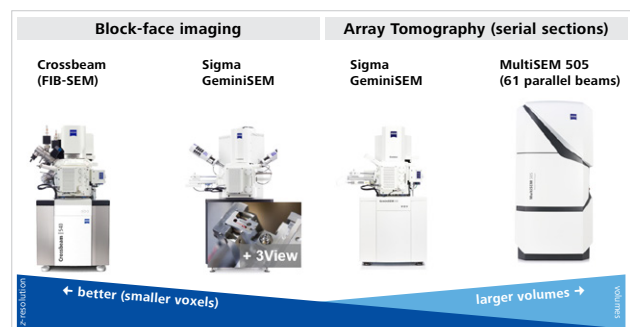


**Figure 4** Comparison of the different imaging techniques in 3D.

## Large Area Imaging

ZEISS offers a set of solutions for reliable and fast large area imaging. ZEISS Atlas 5 software allows large area imaging up to 32k × 32k pixels with high resolution and at high imaging speeds (down to 25 ns dwell time per pixel). Stitching of individual images then yields extremely large fields of view. Once image acquisition has taken place, ZEISS Atlas 5 enables the user to zoom seamlessly through the big image data—from nanometers to centimeters—always at the most appropriate resolution.

If ultimate acquisition speed is required, the unique ZEISS MultiSEM—the world's fastest scanning electron microscope—becomes the technology of choice. Using multiple electron beams and associated detection channels in one electron optical column, it is the first and so far only commercially available multi-beam SEM. By design, ZEISS MultiSEM increases the speed at which SEM data is acquired by almost two orders of magnitude compared to single-beam SEMs. This serves the rapidly developing need of imaging for large and even larger areas or volumes at nanometer resolution and serves the rapidly developing need for fast electron microscopes that can image large areas or volumes at nanometer resolution.

ZEISS MultiSEM also enables a different approach to large-area sample work, as whole areas are imaged automatically at high resolution, and the sample sites of interest can be searched and identified by inspecting the data set rather than by searching and repeatedly scanning the sample itself. Thus, the sample is only scanned once. In connection with the highly efficient detector setup and automated imaging workflows, electron beam damage is then minimized.

## Imaging Under Near-to-Native Conditions

Freezing of biological samples is an alternative to sample preparation by chemical fixation: Vitrification under liquid cryogenics keeps the ultrastructure of cells and tissues intact. The samples remain completely hydrated and there is no need for fixatives or resin embedding. ZEISS supports all necessary equipment for transferring the sample at cryo conditions into the electron microscope. This approach can also be combined with a cryo light microscope. The correlative cryo microscopy approach benefits from the stabilization of fluorophores under cryo conditions. Furthermore, there is no



**Figure 5** A typical correlative setup

need to worry about loss of fluorescence or structural changes that can be caused by heavy metals and chemical fixation normally used to fix and stain samples for electron microscopy.

## Correlative Imaging

The combination of various imaging modalities such as light and electron microscopy reveals new insights into biological interdependencies. Functional information obtained with a fluorescence microscope can be linked with structural information obtained with the SEM. Regions of interest of a sample can be easily retrieved across different microscopes. ZEISS software solutions support a wide variety of different possible combinations, such as correlation of ultrastructural information with analytical techniques such as Raman and EDX spectroscopy.

## Conclusion

ZEISS offers a large variety of solutions for electron microscopy in life sciences. ZEISS instruments enable traditional imaging of the topography of botanical and zoological samples under different environmental conditions. They also enable easy 2D and 3D imaging of a huge variety of biological samples—resin-embedded or vitrified—with the highest resolution and precision. Imaging large samples, including the possibility of combining the individual datasets from multiple imaging and analysis modalities, was pioneered by ZEISS. Today, a number of software workflows connects light-, electron-, and X-ray microscopes from ZEISS, supplying scientists with a wealth of interconnected data leading to new challenges in data handling, storing, and analysis. We strive to deliver continuous innovation and efficient workflows and work together with our customers to develop new solutions.



# Q & A

## A life of change in the brain

*Jeff Lichtman (J.L.), neurobiologist and the Jeremy R. Knowles Professor of Molecular and Cellular Biology at Harvard University, made time to talk with science reporter and writer Mike May (M.M.) about the changing connections in developing mammalian brains, what they mean, and how to explore them through cutting-edge electron microscopy tools.*

**M.M.: Let's start with the concept of synaptic competition. How would you describe it and why is it important?**

**J.L.:** Surprisingly, maybe, the nervous system of young animals—especially animals like us, mammals—is wired differently than the way it is wired in the adult. By wired, I mean which nerve cells are connected by synapses to which other nerve cells.

Although we humans think of ourselves as learning throughout our lives, the pace of learning is much greater when we're young. We learn how to interpret visual information. We learn how to manipulate our limbs to walk or to drive a car. We keep adjusting our behavioral repertoire as our environment changes. What makes this learning approach powerful is that we don't need a genetic change for each new behavior. We can do it based on learning.

What is going on during this learning period is a central and largely unanswered question about how the brain develops. One of the things we've noticed in a number of parts of the nervous system is that the wiring diagram in baby animals is surprisingly more complicated than in adults. It's as if the brain is, early on, kind of wired for any contingency, and then some subset of the wires and their synaptic connections

are maintained, while many of the other connections are pruned away. Where we've studied this pruning, it looks like a competition between nerve cells that temporarily share the same target cell. The target cell perhaps rewards one of the inputs, allowing it to get stronger, while at the same time, other inputs get weaker and disappear.

**M.M.: What are the top challenges of studying synaptic competition?**

**J.L.:** The competition is often between nerve cells that are nearly identical. So, most of the strategies microscopists use to label cells either label all the competitors or none of them, but it's very hard to find labels that allow you to see each individual cell as a separate entity.

We developed a technique called Brainbow that makes each nerve cell a different color, which certainly helps. However, competition often occurs at levels of resolution where the optical microscopy that Brainbow uses doesn't show fine enough details. So, we have begun to use electron microscopy, which has far better resolution, and where—even without staining, just by virtue of the high resolution—we can trace and map out the wires associated with different nerve cells.

**M.M.: How have you applied electron microscopy to synaptic competition?**

**J.L.:** The key to what we're doing—and it was technically very challenging until relatively recently—is generating 3D images of very highly resolved structures by taking an image of a single slice of a volume, then taking an image of the subsequent slice of the same volume, and continuing to do that until we have pictures of every single thin slice of a thick volume. The slices are in the range of 30 nanometers, which is about one-thousandth as thick as a human hair. So, it takes many thousands of sections to go through most volumes.

Imagine a brain tissue sample as a bowl of spaghetti. In a very thin slice through that, all you see are the little sections of each of the pieces of spaghetti. In the next slab, it's very easy to figure out which piece of spaghetti is attached to the piece from the previous one. By tracing the cut processes from one section to another, you can generate the directions, the branching, the synapses of all the spaghetti—all the wires in the nervous system. This method of generating many consecutive sections is called serial electron microscopy.

We have automated the process by cutting the sections with a microtome, floating them

in a small water bath, and then picking them up with a conveyor belt that picks up one section after another on a long piece of plastic tape. Then, we cut the tape into segments, paste them onto a very flat silicon wafer, and image them automatically in an electron microscope.

**M.M.: How have you used fast, large-volume ultrastructural imaging?**

**J.L.:** The challenge in microscopy has always been a trade-off between either getting high resolution or large areas—in our case, large volumes. That is, either you want to see the fine details or you want to see a lot. That’s the way it was until recently.

Now, the extraordinarily fast speedup in the way we acquire these images—one way is the multibeam approach that ZEISS has designed with our serial electron microscopy needs in mind—allows us to get very high resolution over areas that are much larger than we could before. With many, many sections, we image reasonably large volumes, like a cubic millimeter, which is still a very small part of the brain.

With 30-nanometer slices, it takes over 33,000 to get a millimeter of depth. Imaging each of those slices at 4-nanometer resolution and 1 millimeter by 1 millimeter requires 250,000 times 250,000—62.5 billion—pixels. For all 33,000 or so slices, you end up with two petabytes of data.

Another step uses a multicore cluster of computers to digitally register each section into an aligned stack. Then, data from humans tracing out the pathways are used as training sets for convolutional neural nets to do the tracing automatically. Once trained, computer algorithms do a pretty good job tracing, and generate a first-pass wiring diagram of the tissue.

**M.M.: Can you tell me more about the benefits of the multibeam technology?**

**J.L.:** A scanning electron microscope has an electron beam that scans back and forth across the whole area. If you had two beams, each working at the same time on nearby areas of the sample, you’d go twice as fast, in principal. The multibeam machine we have was the first one that ZEISS made available, and has 61 beams, which accelerate the acquisition of image data by more than 10-fold. Newer ones have 91 beams.

The increase in throughput, however, is not only related to the number of beams. At some point, the rate-limiting step is the speed of moving the stage from one location to another on the wafer.

**M.M.: As you have applied the latest electron microscopy technology to synaptic competition, what is one of your most interesting findings?**

**J.L.:** To be clear, we didn’t go into serial electron microscopy trying to find evidence for a particular hypothesis about synaptic competition. The imaging techniques we use, however, have provided evidence of a kind of organization that may have arisen because of synaptic competition. For my lab, these serial electron microscopy tools map out wiring diagrams in a very bottom-up way. We try to accurately describe what’s in the data, and then hope a hypothesis will emerge.

As I just mentioned, when we look at brain samples with these high-resolution techniques, we see things that are interesting from the perspective of how nerve cells might be competing. For example, in the adult cerebral cortex, we found that a single neuron often establishes many different synapses on the same target cell despite many other potential targets in its vicinity.

Perhaps during development, neurons initially connect with more target cells, and as some of these connections are pruned away, the remaining axons add synapses to give this pattern we see in the adult.

This is a research question we are now going after, but that hypothesis emerged by seeing the adult pattern, which was a regularity in the tissue that we hadn’t expected beforehand.

“ When we look at brain samples with these high-resolution techniques, we see things that are interesting from the perspective of how nerve cells might be competing.”

**M.M.: How is this research impacting neuroscience in general?**

**J.L.:** I see our work—data leading toward hypotheses—as part of an informatics trend in biology. Instead of starting with some big idea to test, one might try to mine big data to get a description of what a tissue shows. This descriptive approach is sort of the way the Hubble Telescope works: You map out the entire universe by looking at every object in the night sky. Then, you see what is there and work very hard to come up with a hypothesis that might explain what the data is trying to tell you.

---

*Mike May is a publishing consultant for science and technology.*

# Navigation of Bee Brains to Human Hips— Microscopy and the Modern Magellans

Author: Melissa L. Knothe Tate, Ph.D.  
University of New South Wales

Date: September 2017

**Technological breakthroughs in imaging have enabled seamless multiscale mapping of cells and their networks, paving the way for remarkable discoveries and an unprecedented understanding of cellular network plasticity in organs as diverse as bone and brain. Insights from these studies shed light on the common paradigms underpinning emergent structure–function properties across organisms and over millenia. Similarly, emergent functions such as learning, and dysfunctions such as addiction, are shared between organisms as diverse as animals and insects. These and other studies provide a blueprint for microscopy-aided invention, as well as design of materials, devices, and therapeutics to improve physical and mental health.**

## Introduction

Nearly five centuries ago, Ferdinand Magellan and Juan del Cano's first circumnavigation of the globe debuted the Age of Discovery.<sup>‡</sup> More than ever before, the intersecting roles of technology and explorers, the first tech users, paved the way for earth-changing findings, "set[ting] the foundation for the level of globalization we see today," from geopolitical to economic and technological contexts. [1]

<sup>‡</sup> *Magellan's voyage was one of many achievements during the Age of Discovery, a period from the 15th through the 18th century, when extensive exploration changed the shape of the world—literally for cartographers and more existentially in terms of political and economic relationships. Discoveries like Magellan's also set the foundation for the level of globalization we see today. The evolution of sailing technology, including the caravel ship design and improved rudders for steering, helped sailors maintain a steady course. The astrolabe and the compass enabled more precise navigation on open waters, expanding where and when ships could travel. A series of scientific breakthroughs allowed Spain, Portugal, England, the Netherlands and other European nations to overcome the geographic constraints of continental Europe. No longer beholden to a treacherous land route for trade with the East, Continental naval powers came to define geopolitics for centuries. [After 1]*

Magellan and del Cano's daring feat thrice leveraged the power of the human mind, i.e., not only (i) to invent the technologies that made the circumnavigation possible, but also (ii) to apply the technologies during the circumnavigation, and, (iii) in the process, to discover and to invent in unprecedented ways. Hence, beyond securing safe and stable trade routes, their explorative circumnavigation resulted in

long-lasting discoveries, i.e., proving that the Earth is round, establishing the international date line as a consequence of the unexpected finding that a day was "lost" in the globe's circumnavigation (despite keeping of meticulous ship logs), as well as the connection of far-flung peoples and the identification of new species.

Today, some 500 years after the start of Magellan's voyage of discovery, microscopy has transformed scientists into "modern Magellans" (Fig. 1, 2), where the intersection of technology and the mind will likely pave the way for a new Age of Discovery of the world within the human body. Like the Earth, our bodies are complex ecosystems with circa 15–70 trillion cellular and a similar order of magnitude bacterial (microbiome) inhabitants. [2, 3] Understanding population dynamics among diverse cell types as well as the microbiome of the body necessitates technological tools to carry out epidemiological studies within individuals.

Recent technological tool developments in the imaging sector will pivot scientific perspectives and ensuing explorations, from pinhole foci to intersecting planes to full volumes of study, from nano- to meso-length scales and with high temporal fidelity. Over the past three decades, research teams focused predominantly on single molecules, cells, tissues, organs, and organ systems. Yet, increasingly, new discoveries

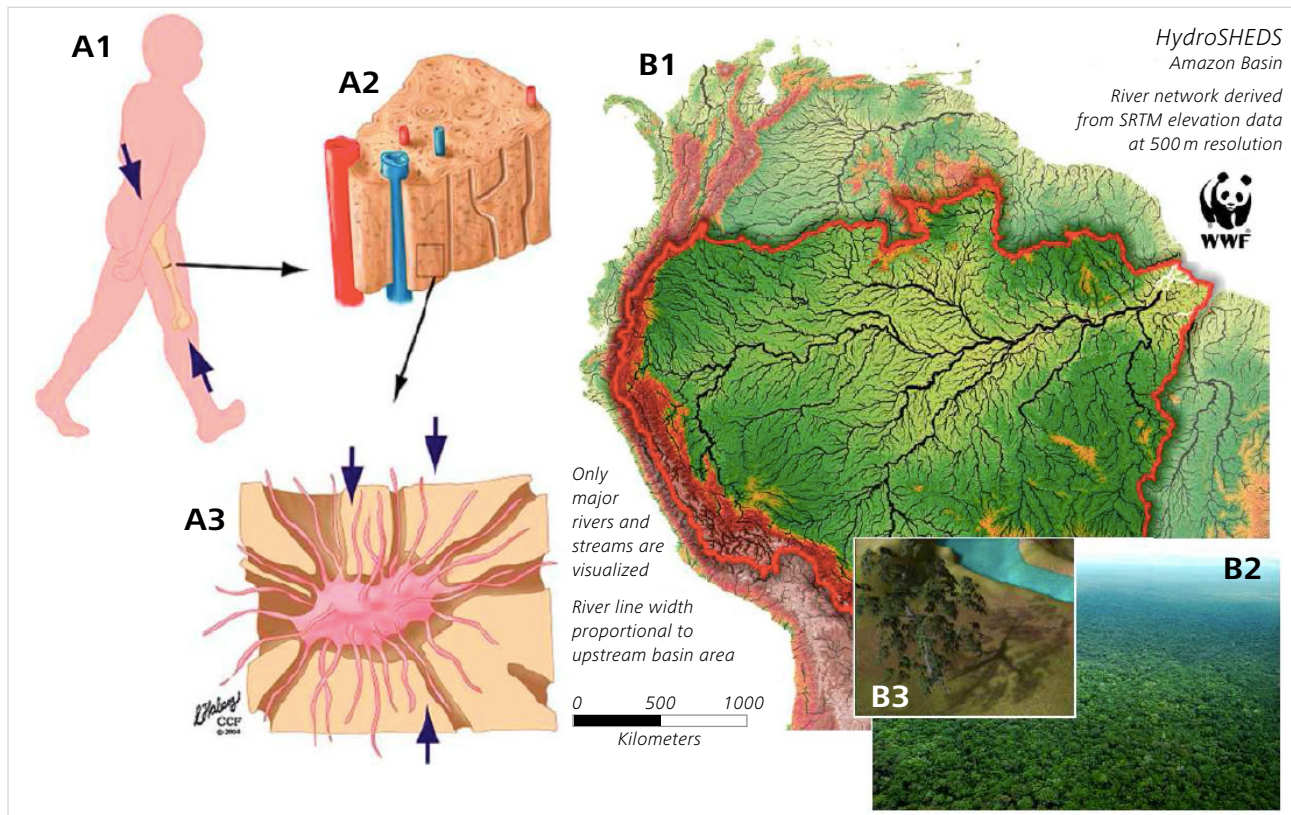


**Figure 1** Complex biosystems share remarkable similarities even if at first appearing to be quite disparate. Understanding the connectivity of individual cells in context of tissue and organ health necessitates a means to discern the forest from the trees and vice versa, or in short, a method to image seamlessly along the length and time scales. For example, the waterways of the ecosystem bone and its inhabitant osteocytes (A1–A3) and those of the Amazon rainforest ecosystem and its inhabitant trees (B1–B3) exhibit similar structures and length scale relationships. The pericellular networks around osteocytes, which are anchored within mineralized bone tissue via cellular processes, show fractal structure that is remarkably similar to that of trees, anchored by roots, and fed via the watersheds of the rainforest. Also the ratio of length scales of individual inhabitant cells/trees to the ecosystem, e.g., osteocyte: femur and tree: Amazon rain forest, is similar, i.e.,  $1:1 \times 10^5$ . Used with permission after [5].

occur at interfaces between length scales, tissue types, organ systems, and even disciplines, necessitating new approaches and new tools to observe, measure, and elucidate mechanisms (Fig. 2). As recently as 2009, this sparked a major debate at the meeting of the National Science Foundation's Civil, Mechanical, and Manufacturing Innovation Division Grantees, centered around whether true multiscale modeling and prediction of complex biosystems behavior would ever be possible, given the then insurmountable barrier to observing and quantifying changes in behavior between and across length and time scales. In less than one decade since that time,

*[s]eamless multiscale imaging technologies are enabling R&D teams to [link] events at different time and length scales in unprecedented ways. In addition to [illuminating] the nanoscopic through mesoscopic worlds of cells and the tissues and organs they inhabit, cutting-edge multiscale imaging technologies are also enabling the development and validation of seamless multiscale vir-*

*tual models that will enable efficient predictive studies..., profoundly increas[ing] the [rate] of scientific discovery. Together, paired imaging and virtual modeling methods will create a portal to new technologies and innovative approaches. [These will in turn enable] engineer[ing] and transl[ation of] emergent behavior, where emergence refers to properties or patterns arising from the putting together of simpler elements which themselves do not exhibit the properties or pattern.*  
[After 4]

Indeed, cutting-edge microscopy is setting the stage for the epidemiological study of cell and microbiome populations within individuals as well as amongst populations of individuals, from bee brains to human hips.

Together with geospatial mapping, navigation, and exploration approaches, new microscopy-based technological tools, such as light sheet microscopy and multibeam scanning electron microscopy (mSEM), are leading the way. Geospatial navigation and exploration approaches, similar to those

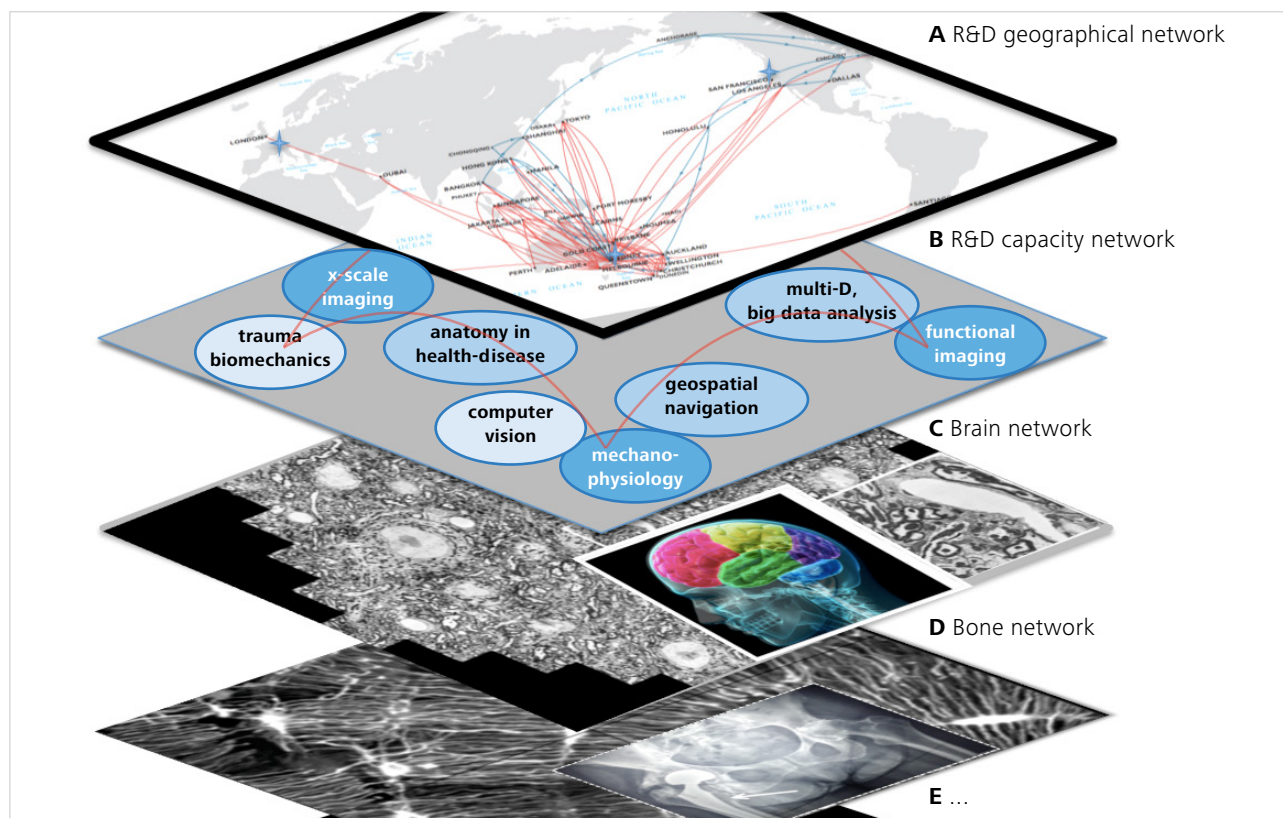


**Figure 2** Beyond the traditional four dimensions (spatiotemporal,  $xyz$ t), leveraging of technology, teams, and multidisciplinary expertise across cell/tissue/organ types as well as imaging modalities, is expected to speed the pace of discovery and innovation. A. With current digital communications capacity, global R&D networks leverage expertise irrespective of geographic obstacles, demonstrated in the context of the Qantas flight network, which links Australia to the rest of the world. B. Thereby novel, interdisciplinary expertise networks can be formed to create innovative solutions to science's most intractable unknown questions and research problems. C. In combination with leading-edge technology (i.e., cross-scale imaging modalities, computational including hardware and software, virtual modelling of complex biosystems), cross-length and -time scale imaging methods will be applied to disparate organ and tissue systems and their inhabitant cellular networks, e.g., brain (C) and bone (D), etc. (E). This is expected to lead to new discoveries, invention of disruptive technologies, and associated new economic market opportunities. (C,D,E) after [6,7].

applied to the Earth, are yielding an unprecedented understanding of our bodies as biosystems that adapt throughout life, and in health and disease. For instance, the cellular populations of the human femur include osteocytes, which are nonmotile cells encased in mineral cavities (Fig. 1A3), as well as motile bone cells that resorb (osteoclast) and build (osteoblast) bone, and cells of the circulatory and immune systems. Understanding the (patho)physiology of a single osteocyte in the complex biosystem of the femur is akin to understanding that of a single tree in the Amazon Basin (Fig. 1). Both depend on flow through the biosystems' waterways for basic survival, from transport of nutrients and waste disposal to extracellular signaling pathways. At the same time, the health of the tissues making up the femur and of the Amazon rainforest of South America depend on the health of those respective biosystems' inhabitants;

whereas the sickness and/or death of a single inhabitant represents part of the normal steady state of the biosystem, emergent pathologies are often not recognized until health implications manifest in an obvious manner and are difficult if not impossible to reverse. [5]

This manuscript describes the unfolding role of microscopy in scaled-up leveraging of the human mind's power. Concomitant advances in computer hardware and software that enable the management, analysis, storage, and transfer of resulting massive datasets as well as their automated analysis using deep-learning algorithms (also referred to as machine learning and/or artificial intelligence) catalyze this microscopy-enabled scale-up of the mind. Here we first address microscopy-enabled navigation of bee brains to human hips, showing how emergent properties can be deciphered when microscopy

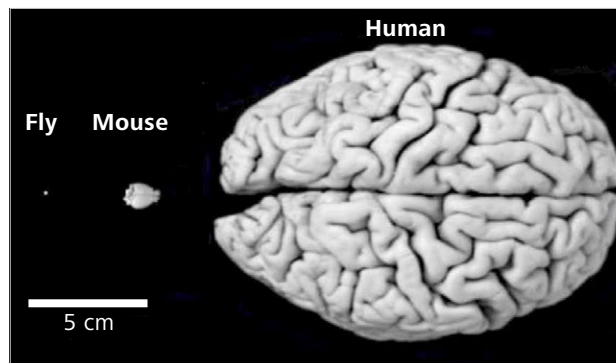
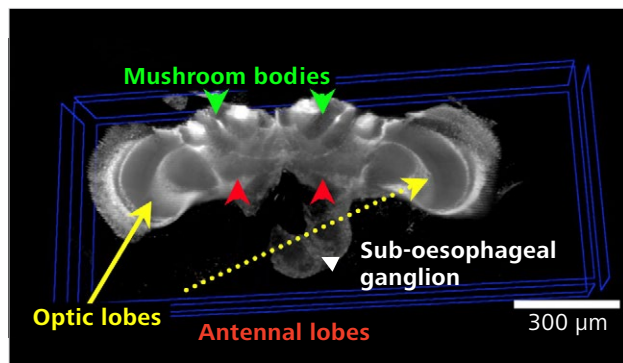


**Figure 3** Concept of scale and seamless imaging of structure and function across length scales of the brain. A. Light sheet fluorescence microscopy image of the mushroom body, a part of the bee brain. Mid-coronal section showing anatomical details of relevance for learning and addiction studies. Used with permission after [10]. B. Relative size comparison for brains of the fruit fly, mouse, and human. Used with permission after [11].

tech is combined with computational technologies. Then we describe how deciphering nature's paradigms to engineer emergence are setting a path for Microscopy-Aided Design And Manufacture (MADAMe). Finally, we place these in the context of the Age of Discovery initiated by Magellan, pointing toward a new, inward Age of Discovery that promises to solve Descartes' mind-body conundrum by revealing the mechanisms of multiscale mechanophysiology and other currently intractable research questions with profound implications for human health. [8]

### Navigation of bee brains to human hips

Cells are the body's "expert systems builders, maintainers and organismal traffic controllers." They create the physical infrastructure and systems of our bodies, which underpin higher-order behaviors such as ambulation, coordination between the brain and body, and cognition itself. Indeed it is the intrinsic connectivity of cells that "provides a measure of infrastructural integrity that likely influences the efficiency of the cellular communication as well as adaptation across tissues and organs." [9] Whereas confocal microscopy gives detailed information of cellular connectivity and its degeneration at a limited microscopic tissue scale, understanding the effect of emergent behavior on network connectivity at the organ scale requires higher-fidelity means to observe and study that network in detail, from nanoscopic- to mesoscopic-length scales. [4,6]

The totality of these physical cellular connections and their resulting networks in 3D has been referred to by the neuroscience community as the "connectome," and the process of

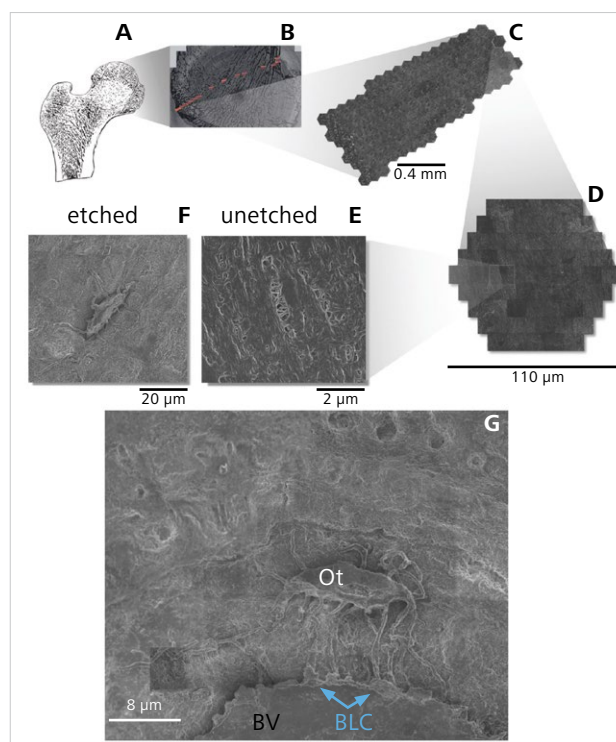


**Figure 4** Using geonavigational approaches and Google Maps API, maps have been created to explore cell populations in the human hip, across length scales from nano to meso. A–D. The 4.8 cm diameter femoral neck of a single patient (undergoing hip replacement—these tissues were discarded as a normal part of surgery) was imaged using a ZEISS MultiSEM 505, resulting in over 55,000 SEM images that were stitched together using Fiji and TrakEM2 libraries. These were then exported as 2,000,000 prerendered tiles (256 Å resolution) for interactive exploration using Google Maps API. E. In unetched specimens (resolution approximately 4 nm per pixel), osteocytes are somewhat hidden. F. Etching protocols reveal osteocytes (Ot in G); the living, nonmotile inhabitants of bone tissue are tightly coupled to the Bone Lining Cells (BLC, G) along the inner surface of all Blood Vessels (BV, G); G. Google Maps API is used to render the pyramidal data storage to achieve a seamlessly "zoomable" image of the bone's connectome. Used with permission after [4]. Map and navigation can be accessed via [12].

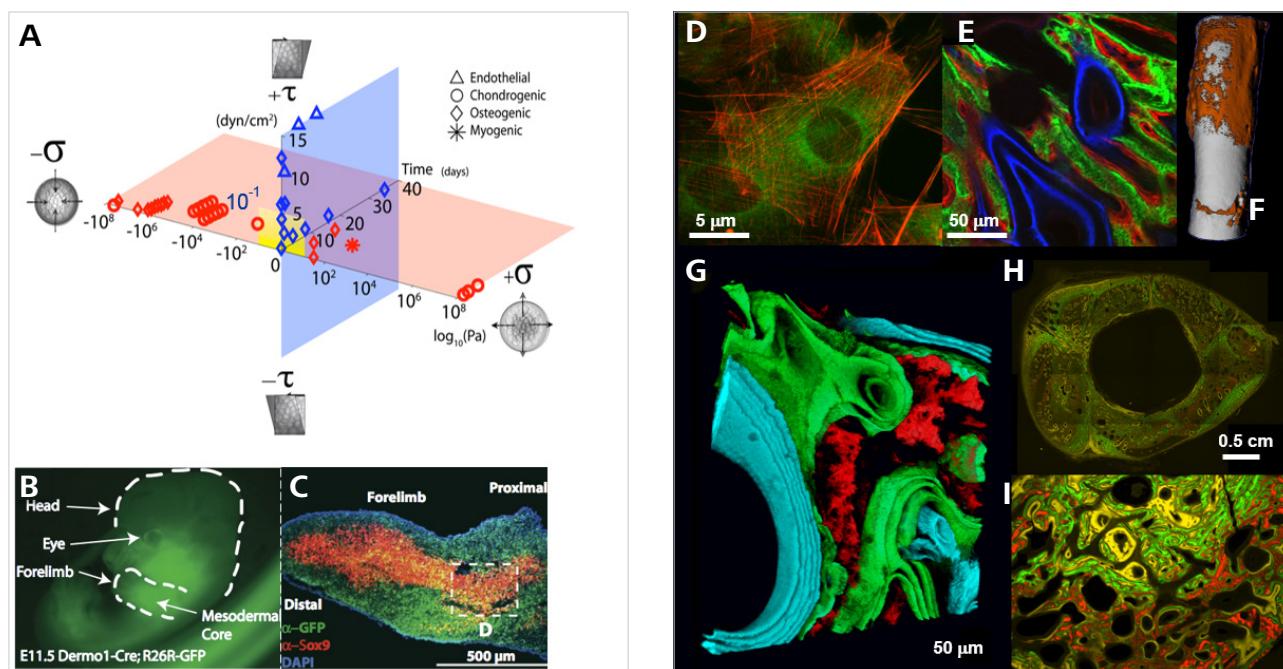


**Figure 5** Tissue genesis by cells shows emergence of form and function. This occurs across many orders of magnitude, of both length and time scales: from cell- to tissue- and organ-length scales, where development recapitulates the evolution of vertebrates (millenia) and postnatal healing recapitulates prenatal development. **A**. In utero and in postnatal life, uncommitted stem cells respond to dilatational (volume changing) and deviatoric (shape changing) stresses as well as biochemical cues, which result in up and down regulation of gene transcription. Over time, these may result in lineage commitment (data point shape indicates cell fate from a compilation of stem cell studies in which cells were subjected to specific mechanical loading regimes). **B**. At 11.5 days' gestation in the mouse, skeletogenesis begins and the (C) developing limb buds show patterns of musculoskeletal development. **D**. At the length scale of a single stem cell, even very tiny mechanical cues, 1,000 times smaller than those experienced by a chondrocyte in the adult knee during walking, induce a rearrangement of the cytoskeleton (red, actin cytoskeleton) and secretion of collagen (green autofluorescence around nucleus), a structural protein that is transcribed in the nucleus. **E**. Over time (green: 1–2 weeks, red: 3–4 weeks, blue: 8–12 weeks), these collagenous matrix proteins are secreted into the extracellular matrix (ECM), forming a 3D weave of ECM (G) that, together with the cells, makes up the tissue (H, I, F). Used with permission after [7, 16].

rendering, analyzing, and understanding the connectome as “connectomics.” Sebastian Seung, a pioneer on the subject, refers to this explicit neural circuit diagram of the brain as that which “makes us who we are.” [13] Taking a less cell-centric perspective, tissues per se reflect an organism’s experiences in the physical world throughout life, as cells transduce and memorialize the physical and chemical stimuli they experience throughout the lifespan of an organism in the transcription of proteins, which are the stuff from which tissues are made (see below 3. Understanding Nature’s Paradigms...). [14] In short, “[c]reated by the cell itself, the extracellular matrix comprising the structural components of tissue reflects the long-term memory of the cellular experience,” which makes up at higher-length scales the tissue and organ experience. [9]

Two general approaches, including choice of model and choice of imaging modality, enable a connectomics ap-

proach to mapping cellular connectivity across organs as diverse as brain and bone (Fig. 2–4). In the case of the brain, researchers have relied on animal and, more recently, insect models as a first step toward understanding structure–(dys)function relationships underpinning the human brain and cognition. The bee brain presents a surprisingly relevant model for an array of functional (behavioral) outcomes related to structural changes in the brain, encompassing a variety of emergent behaviors related to brain structure (Fig. 3). [15] These include study of the effects of pesticides and drug exposure in the brain, brain plasticity, cognition, and addiction. Neonicotinoids, one of the most prevalently used class of insecticides, target nicotinic acetylcholine receptors of the central nervous system. These insecticides have been associated with alarming declines in honey bee populations. Recent studies implicate neonicotinoids in subjecting honey bees to addictive behaviors analogous to human addiction to nicotine. [10]

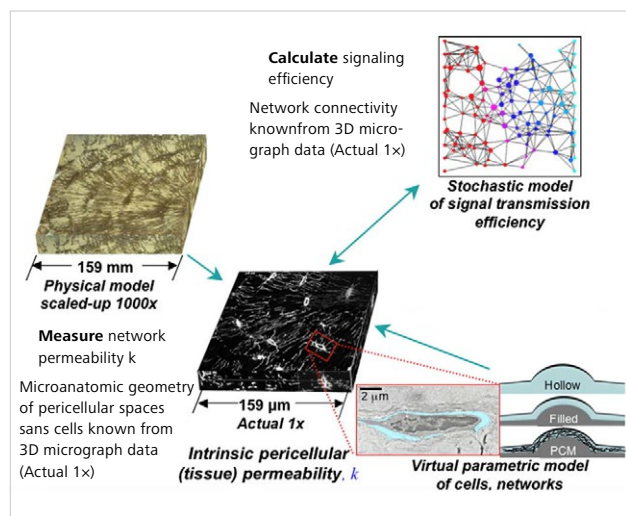


**Figure 6** Microscopy-based measurement of intrinsic tissue permeability, a measure of extracellular information transfer efficiency, in pericellular networks. While previous methods enabled measurement of tissue permeability based on confocal microscopy acquired image volumes, the method applies equally to new volume renderings of tissue connectomes. A. Actual (1 $\times$ ) pericellular network volumes are acquired using confocal microscopy. B. Scaled-up (1,000 $\times$ ) physical models are rapid prototyped using 3D printing methods, rendering the inverse volume of the pericellular network as voids in the model. Permeability is measured by measuring flow characteristics of a 1,000-fold more viscous fluid than pericellular fluid through the volume of the model under a known pressure gradient. C. The effect of cells (filled) and pericellular matrix (PCM) within the pericellular fluid space is studied in parallel, virtual parametric models of cells and their networks. D. Stochastic network models determine the effect of cellular connectivity of signal transmission efficiency. Used with permission after [21].

Yet, even in the very small yet remarkably effective brain of the honey bee (which has 950,000 neurons compared to the human brain with 100 billion neurons), a major barrier to understanding emergent behavior that underpins learning and memory is the paucity of methods to image cellular connectivity across length and time scales. Light sheet fluorescence microscopy (LSFM) provides a means by which entire, cleared bee brains and their resident cells can be visualized in situ (Fig. 3). [10, 17] Connectivity of cells in the different structures of the adult honey bee brain in its baseline state can be compared with that following exposure to neonicotinoids, controlled learning environments, as well as the interactions between the two, to provide a basis for observing and quantifying structure–function relationships underpinning emergent behaviors, including learning and addiction (Fig. 3).

Mapping and rendering the connectome of larger brains, e.g., moused-sized (75 million neurons), in the nanoscopic

detail required to map connections between neurons, requires even higher resolution and capturing of greater volumes of interest, thus mandating new imaging modalities (Fig. 3, 4). [18] Multibeam scanning electron microscopy (mSEM), a technology developed originally for rapid throughput scanning of 10 cm semiconductor wafers for quality control at the nanometer-length scale, offers an ideal tool to image seamlessly across these length scales (Fig. 4). In combination with sectioning and volume-rendering methods, it has been used to reconstruct macroscopic volumes of murine brain tissue. While whole-brain volume renderings have not yet been achieved, methodologies are underway to achieve this feat within the next year or two. [6, 19]

Scaling up a further order of magnitude, the first Google Maps API approach to mapping the human hip was recently achieved in tissue discarded routinely during the normal course of hip replacement. Rendering of the nanoscopic resolution images at the mesoscopic scale, and using Google Maps API, enables the scientific community and public alike to interact with and explore the human hip tissue maps in a way similar to their everyday interactions with Google Maps navigation (Fig. 4). [4, 6, 7, 12, 20] Such maps are expected to open up the possibility of intra- and interindividual as well as population-based epidemiological studies of diseases related to degeneration of cellular networks with age, e.g., osteoporosis and osteoarthritis. These diseases exhibit similar hallmarks to other degenerative diseases, and diagnostic tools are in development based on outcomes of these studies. Taken as a whole, connectomics will in the future be applied to every organ of the body, leading to unprecedented understanding of the role of cell networks in organ and organism (patho)physiology throughout life, and to the development of diagnostics that predict emergent cell-scale pathology and enable detection and treatment well before permanent damage at tissue- and organ-length scales.

### Understanding Nature's Paradigms to Engineer Emergence

Emergent properties arise from the combination of smaller elements that themselves alone do not observe emergent properties. Natural materials and systems, e.g., from weather to disease, exhibit these properties, as do human-made systems such as financial markets. The prediction of emergent events necessitates an understanding of nature's paradigms

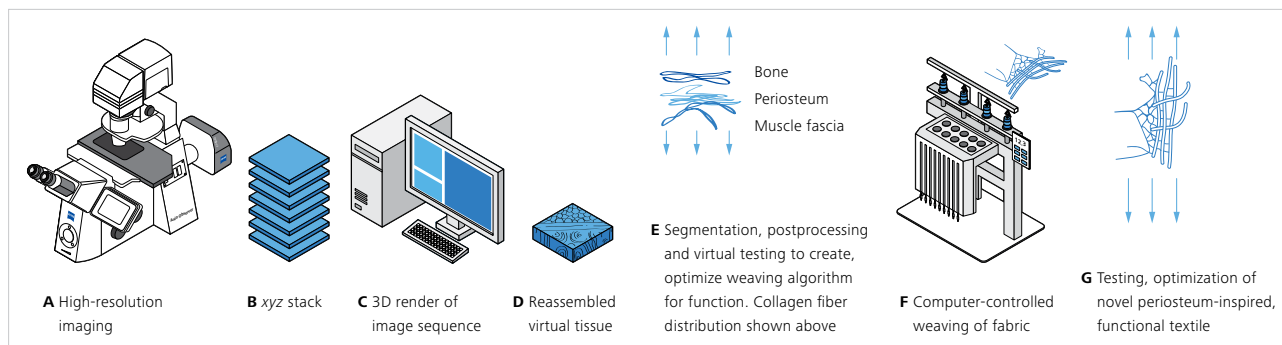


**Figure 7** Microscopy-enabled, scaled-up computer-aided design and manufacture of multifunctional textiles emulating the body's own. A–D. Second harmonic generation and two-photon excitation microscopy of tissues, e.g., periosteum, a soft and elastic tissue sheath bounding all nonarticular surfaces of bone, is used to map the precise patterns of elastin and collagen in native tissue. E. These are rendered using computer-aided design software, where the patterns can be optimized for desired design specifications. F. Optimized designs provide inputs for computer-controlled weaving of textiles that emulate the tissue studied under the microscope. G. Mechanical and other functional tests are performed to test whether designs achieve targeted structure–function relationships. Used with permission after [14].

to engineer emergence. Organismal development, both during evolution of vertebrates as well as through in utero development, which recapitulates this evolution, provides a perfect example, e.g., whereby biosystems' complexity and smart properties emerge over time from the seminal, two-cell fertilization event (Fig. 5). A bottom-up approach to the problem follows and facilitates elucidation of the path of emergence, for

*"[t]he cell itself, from its undifferentiated to its terminally differentiated state, is brainless yet retains functional memory in its structure, which becomes entrained or conditioned as structural connections are reinforced through repeated activity, ultimately stabilizing or entraining functional capabilities [like cellular conditioning]....[Similarly, c]reated by the cell itself, the extracellular matrix comprising the structural components of tissue reflects the long-term memory of the cellular experience....The length and time scales of cellular processes play an integral role encompassing cellular memory, enabling the cell to adapt to best survive follow-on experiences whose probability depends on previous experiences."*

[Adapted from 9]

In this way, each cell's experience scales up to the tissue, organ, and organismal scale, in organisms as diverse as humans and giant Sequoia trees, the world's largest living things by volume (and the oldest of which is 3,500 years old).

### Microscopy-Assisted, Computer-Aided Scaled-Up Invention and Design

The capacity to understand and predict emergence in natural systems paves the way to innovate new methods and materials to emulate nature's paradigms, e.g., those exhibiting smart or stimuli-responsive properties. Many of

the studies described in this manuscript provide a blueprint for microscopy-aided invention and design of materials, devices, and therapeutics.

*Cells are the living component of tissues, which are self-annealing biological materials. The self-annealing property of tissues represents the end result of cell activity over a given period of observation....Tissue remodeling depends on patent cellular machinery, as well as cellular navigation and coordination....Delineated by the structural network of cells, which in themselves allow for direct ...intracellular signaling, the contiguous pericellular fluid provides a powerful extracellular means to modulate cellular activity. Elucidation of the pericellular fluid environment could provide important insight into mechanisms underlying cellular navigation and coordination during tissue remodeling. [It] is interdependent on the [cellular network as well as the poro-elastic weave of tissue's extracellular matrix].*

[After 21]

Hence, taking a less cell-centric view of nature's self annealing materials, i.e., tissues, microscopy, and computational modeling lend themselves to understand, measure, and emulate the permeability of pericellular networks as well as the natural weave of tissues' extracellular matrix structural proteins, including elastin and collagen. [14, 21]

Permeability provides a measure of the interplay between the solid and fluid phases of a biological material. In any given tissue, permeability through the nano- and microscale pericellular fluid network provides a quantitative measure for the tissue's capacity to transport information across tissues and organs, e.g., from brain to cartilage to meniscus, lymphatic tissue, and bone. Using 3D printed, physical models scaled up from volumetric microscopy-based renderings of pericellular networks, and parametric scaling or similitude

analysis, it is possible to measure permeability in pericellular networks as a quantitative measure of signal transmission efficiency. Stochastic network modeling can then be used to estimate changes in signal transmission efficiency as a function of changes in network connectivity (Fig. 6). While initial studies were limited to volumes of interest  $160 \times 160 \times 40$  microns in size, LSFM and mSEM will enable true organ-scale measures of signal transmission efficiency, as well as the tying of local and global network connectivity effects on the same.

The stimuli responsive and adaptive properties of animal and plant tissues “emerge macroscopically from the anisotropic multicellular assembly and directional secretion of nanoscopic extracellular matrix proteins,” resulting in a cell-spun and woven, adaptive textiles-cum-tissues. Current methods to control cell behaviors are developing, e.g., to guide assembly of higher-order architectures that emerge during development, but have not yet reached the stage to guide true cellular spinning and weaving. [22] Nonetheless, modern microscopy has enabled a different, scaled-up approach to engineer emergence. The architecture of tissues such as periosteum, the tissue bounding all nonarticular bony surfaces in the body, can be mapped using second-harmonic generation and two-photon excitation microscopy. This results in precise 3D patterns of elastin and collagen fibers, the structural proteins making up the tissue. These natural tissue weaves are then rendered using computer-aided design software. These provide the basis for tissue-inspired, multidimensional fabrics that are woven using a computer-controlled jacquard loom (Fig. 7). [14, 16]

Ironically, the Jacquard loom (invented in 1804) was the first computer, and long punch cards were used as a physical binary code to allow for dropping (through holes) and holding up (no holes) of the weaving hooks. In this way, the series of holes in the punch cards (usually long loops) encoded the pattern of the textile. [23] Using recursive logic, it is now possible to weave textiles that emulate the body’s own tissues. This concept has resulted in a disruptive technology that can be implemented for design of advanced materials that exhibit smart, emergent properties and that will lend themselves for myriad applications from medical to transport and safety industries. [14, 16]

The investigation of permeability and fluid flow through scaled biological tissues holds many implications for understanding tissue (patho)physiology and drug delivery through tissues. Similarly, animal and plant textiles provide a plethora of natural patterns that can serve as motifs for multifunctional textiles. Multidimensional weaving and weaving-based composite materials may supplant 3D printing for mechanically functional materials, since textiles exhibit superior mechanical performance in tension and bending.

## Conclusion

Taken together, microscopy has transformed scientists into “modern Magellans,” providing the technological basis for unprecedented exploration of the natural world within the human body. Next-generation, microscopy-aided invention and design of materials, devices, and therapeutics promise to improve physical and mental health as well to enable the engineering of next-generation materials and devices that emulate the body’s own.

Magellan’s voyage was one of many achievements during the Age of Discovery, when extensive exploration changed the shape of the world and thereby thrice leveraged the power of the human mind. Exploration and elucidation are the first steps toward the engineering of nature’s emergent properties, which underpin higher-order behaviors such as mechanoadaptation of tissues as diverse as bone and brain, cognition, and creativity. In turn, higher-order behaviors beget further emergent behaviors, e.g., creation of tools to creation of computing machines, from weaving looms to quantum computers, to development of deep learning algorithms or artificial intelligence, to the development of robots that themselves exert emergent behaviors. Microscopy-enabled R&D teams, the “new Magellans,” have entered a modern Age of Discovery, which will both leverage manifold and scale-up infinitely the human mind’s power, with profound potential to improve well-being throughout life.

**References:**

- [1] R. Keller (2015) Magellan's voyage and the era of global trade. Stratfor World View. <https://worldview.stratfor.com/article/magellans-voyage-and-era-global-trade>.
- [2] E. Bianconi, A. Piovesan, F. Facchin, A. Beraudi, R. Casadei, F. Frabetti, L. Vitale, M.C. Pelleri, S. Tassani, F. Piva, S. Perez-Amodio, P. Strippoli (2013) An estimation of the number of cells in the human body. *Annals Human Biology* 40: 463–471.
- [3] R. Sender, S. Fuchs, R. Milo (2016) Are we really vastly outnumbered? Revisiting the ration of bacterial to host cells in humans. *Cell* 164: 337-40.
- [4] M.L. Knothe Tate, D. Zeidler, A.F. Pereira, D. Hageman, T. Garbowski, S. Mishra, L. Gardner, U.R. Knothe (2016) Organ-to-cell-scale health assessment using geographical information system approaches with multibeam scanning electron microscopy. *Advanced Healthcare Materials* 5: 1581–1587.
- [5] M.L. Knothe Tate, T. Falls, S. Mishra, R. Atit (2010) Engineering an ecosystem: taking cures from nature's paradigm to build tissue in the lab and the body. *Fields Institute for Mathematics in Biology monograph series on New Perspectives in Mathematical Biology* 57: 113–134.
- [6] A.-L. Eberle, S. Mikula, R. Schalek, J. Lichtman, M.L. Knothe Tate, D. Zeidler (2015) High-resolution, high-throughput imaging with a multiple beam scanning electron microscope. *Journal of Microscopy* 259: 114-20.
- [7] M.L. Knothe Tate, M. Detamore, J.R. Capadona, A. Wooley, U. Knothe (2016) Engineering and commercialization of human-device interfaces, from bone to brain. *Biomaterials* 95: 35–46.
- [8] M.L. Knothe Tate, T. Fath. (2016) The only constant is change: next generation materials and medical device design for physical and mental health. *Advanced Healthcare Materials*, 5: 1840–1843.
- [9] M.L. Knothe Tate, P.W. Gunning, V. Sansalone (2016) Emergence of form from function: role of stem cell mechanoadaptation in sealing of cell fate. *BioArchitecture* 6: 85–103.
- [10] A. Oni, S. Fok, U. Knothe, R. Whan, M.K. Greco, M.L. Knothe Tate (2017) Light sheet microscopy of bee brains to illuminate "What makes the brain buzz?", in review.
- [11] N.J. Strausfeld, F. Hirth (2013) Deep homology of arthropod central complex and vertebrate basal ganglia. *Science* 340: 157-61.
- [12] [mechbio.org](http://mechbio.org)
- [13] S. Seung (2012) *Connectome. How the brain's wiring makes us who we are.* Houghton Mifflin Harcourt.
- [14] J.L. Ng, L.E. Knothe, R.M. Whan, U. Knothe, M.L. Tate (2017) Scale-up of nature's tissue weaving algorithms to engineer advanced functional materials. *Scientific Reports*, 7, 40396.
- [15] R. Menzel (2012) The honeybee as a model for understanding the basis of cognition. *Nature Reviews Neuroscience* 13: 758–768.
- [16] M.L. Knothe Tate (2017) *Biotextility - The Cellular Catwalk*, ISBN 978-0-646-97861-1, Sydney.
- [17] J. Huisken, et al. (2004) Optical sectioning deep inside live embryos by selective plane illumination microscopy. *Science* 305: 1007–1009.
- [18] *Mouse Brain Atlas*. [http://www.mbl.org/atlas165/atlas165\\_start.html](http://www.mbl.org/atlas165/atlas165_start.html)
- [19] S. Mikula, W. Denk (2015) High-resolution whole brain staining for electron microscopic circuit reconstruction. *Nature Methods* 12: 541 6.
- [20] A. Pereira, D. Hageman, U. Knothe, D. Zeidler, M.L. Knothe Tate (2016) Creating high-resolution multiscale maps of human tissue using multibeam SEM. *PLoS Computational Biology* 12: e1005217.
- [21] E.J. Anderson, S.M. Kreuzer, O. Small, M.L. Knothe Tate (2008) Pairing computational and scaled physical models to determine permeability as a measure of cellular communication in micro- and nano-scale pericellular spaces. *Microfluidics and Nanofluidics* 4:193–204.
- [22] S.F. Evans, D. Docheva, A. Bernecker, C. Colnot, R. Richter, M.L. Knothe Tate (2013) Solid-supported lipid bilayers as a novel platform to engineer emergence of stem cell fate and tissue architecture using periosteum derived progenitor cells. *Biomaterials* 34: 1878–1887.
- [23] J. Essinger (2004) *Jaquard's Web. How a hand loom led to the birth of the information age.* Oxford University Press, Oxford.

# Discovering 3D Nano Worlds.

ZEISS Scanning Electron Microscopes

// INNOVATION  
MADE BY ZEISS

**GeminiSEM 500**

## Enter a whole new world of automated ultrastructure investigation

Discover the unique ZEISS portfolio of scanning electron microscopes (SEM) for life sciences. Choose your ZEISS SEM for TEM-like 3D imaging and correlate your results with a whole portfolio of complementing techniques. You profit from automated image acquisition of large areas and volumes at high speed with excellent resolution and contrast. Make your research faster and more flexible and get higher throughput.

[www.zeiss.com/life-sciences](http://www.zeiss.com/life-sciences)



# The Moment Your Data Change Scientific Minds.

This is the moment we work for.

// INNOVATION  
MADE BY ZEISS

Your Correlative Microscopy Solutions for Life Sciences from ZEISS



[www.zeiss.com/life-sciences](http://www.zeiss.com/life-sciences)

